

A Formation Model for Type II Porphyritic Olivine Chondrules in Nebular Shock Waves

Alexei V. Fedkin, Fred J. Ciesla, Lawrence Grossman* and Steven B. Simon
Department of the Geophysical Sciences
The University of Chicago
5734 South Ellis Avenue
Chicago, IL 60637

Submitted to *Geochimica et Cosmochimica Acta*
September 19, 2008

*Also Enrico Fermi Institute, The University of Chicago.

ABSTRACT

When a shock wave passes through a nebular region, temperatures, post-shock P^{tot} , heating rate and cooling rate are all calculated to increase with increasing shock velocity, and with increasing dust enrichment or initial P^{tot} of the region. Increasing water enrichment leads to higher temperatures and post-shock P^{tot} , but lower cooling rates. Increasing chondrule size decreases heating and cooling rates. A kinetic model is developed to investigate the mineralogical, chemical and isotopic transformations that would occur in a clump of chondrule precursor dust surrounded by nebular gas in a region traversed by a nebular shock wave. The model includes effects of non-equilibrium melting, fractional crystallization, oxidation-reduction, metal segregation, evaporation, isotopic exchange between droplet and gas, and recondensation. When a region of $P^{tot}=1.5 \times 10^{-6}$ bar and that is enriched in water by a factor of 550 and in dust of reduced chondritic composition by a factor of 600, both relative to a system of solar composition, is subjected to a 6 km/sec shock wave, the resulting droplet evolves into an object with many of the observed properties of Type II PO chondrules, including the presence of low- X_{Fa} relict grains, the mean X_{Fa} , the shape of the olivine composition histogram, the FeO content of the mesostasis, and only small isotopic mass-fractionations of Mg, Si, K and Fe. Peak temperatures near the liquidus will cause fractional crystallization of olivine to begin prior to extensive isotopic exchange between droplet and evaporated vapor, resulting in olivine with core-to-rim zoning in $\delta^{56}Fe$ and a droplet whose bulk $\delta^{56}Fe$ lies outside the range observed for chondrules, unless conditions of higher dust enrichment coupled with lower shock velocity and/or initial P^{tot} prevail.

INTRODUCTION

Chondrules are silicate-rich, glassy spherules that existed as independent liquid droplets in the solar nebula before they crystallized while undergoing cooling at 10-1000K/hr (Hewins *et al.*, 2005). The textures of barred chondrules have been reproduced in laboratory experiments by heating solid precursors to temperatures where all preexisting nuclei were destroyed, and textures of porphyritic chondrules to temperatures where some nuclei survived, generally in the range 1823-2173K (Hewins and Connolly,

1996). Types I and II chondrules differ from one another in having olivine and pyroxene with mean $\text{FeO}/(\text{FeO}+\text{MgO})$ atomic ratios <0.1 and ≥ 0.1 , respectively. The FeO contents of both types of chondrules pose important constraints on their origin, as they imply chemical communication with a gas whose $\log f_{\text{O}_2}$ was $\sim \text{IW}-1.5$, *i.e.*, 1.5 log units below the f_{O_2} of the iron-wüstite buffer, about 5 log units more oxidizing than a system of solar composition (Grossman *et al.*, 2008). In an attempt to understand why chondrules are so oxidized, models have been proposed in which excess water was added to chondrule-forming regions of the solar nebula by evaporation of ice from planetesimals that migrated inward from cold regions (*e.g.*, Ciesla and Cuzzi, 2006). Except for alkalis in Type IIs, both chondrule types are depleted relative to Si in elements more volatile than Si compared to CI chondrites (Jones and Scott, 1989; Jones, 1990; 1994; 1996). Such volatile element depletions are expected to result from evaporation when chondrule precursors are heated to near-liquidus temperatures in hydrogen-rich cosmic gases. Because this process would also produce heavy isotope enrichments in the fractions of the evaporated elements that remain in chondrule residues, however, another major problem in understanding the origin of chondrules is the absence from them of large isotopic mass-fractionations of moderately volatile elements. In an attempt to solve this problem, models have been proposed in which chondrule production occurred under conditions where Rayleigh fractionation of isotopes was suppressed, such as in regions enriched in condensable elements relative to the gas by factors of at least several hundred relative to solar abundances (*e.g.*, Cuzzi and Alexander, 2006).

Desch and Connolly (2002) explored the thermal history of chondrule precursors heated by nebular shock waves. When they included the effects of gas drag and radiation from other chondrules on chondrule heating rates, the effect of chondrule enrichment on heating and cooling rates, and the effect of the post-shock cooling rate of the surrounding gas on cooling rates of chondrules, they were able to compute chondrule thermal histories in reasonable agreement with those deduced from laboratory experiments. The systems investigated by Desch and Connolly (2002) are solar in composition except for the dust enrichments, but the chemical and isotopic compositions of chondrules probably require both dust and water enrichments. Because collisions with water molecules are more energetic than those with lower-mass molecules, both heating rates and peak

temperatures of chondrules will be higher when shock waves pass through water-enriched systems if all other variables are held constant. Also, because of the higher mass density of water-enriched gas, post-shock cooling rates will be lower than in systems with solar water abundance.

In the present work, the thermal history of chondrule precursor material is investigated as a function of initial shock velocity and initial total pressure, P^{tot} , in systems having both dust and water enrichments capable of reproducing the chemical and isotopic properties of Type II chondrules. The resulting thermal histories are then used as input to a kinetic model for the evolution of mineralogical, chemical and isotopic properties of chondrule precursor material in order to compare the computed properties of the final products with those of actual Type II porphyritic olivine (PO) chondrules. A preliminary version of this work appeared in Fedkin *et al.* (2008).

MINERALOGICAL AND CHEMICAL PROPERTIES OF TYPE II PO CHONDRULES

Jones (1990) performed a petrographic and electron microprobe study of a suite of Type II PO chondrules in the Semarkona LL3.0 chondrite. She found them to be composed of olivine, ~27 volume % mesostasis, minor spinel, <1 wt % troilite and even less metallic nickel-iron. In nine chondrules free of pyroxene laths, she found the mesostasis to contain 6.5-9.7 wt% FeO, yielding a mean of 8.1 ± 1.1 wt %. A defocussed beam technique was used to obtain bulk chemical analyses of the chondrules, from which the mean atomic ratios of total Fe/Si, Na/Si and K/Si were found to be 0.34 ± 0.09 , 1.2 ± 0.2 and 1.3 ± 0.5 , respectively, relative to CI chondrites. Thus, although Fe is depleted in the chondrules by an average of 66% relative to CI abundances, there is no evidence for alkali depletion in the average Type II PO chondrule in Semarkona.

Olivine composition histograms of ten Type II PO chondrules were obtained from three sections of Semarkona by wavelength-dispersive techniques in Chicago. After non-stoichiometric compositions were rejected, 213-415 analyses were retained for each histogram. Six of these histograms, representing the full range of compositions and patterns, are shown in Fig. 1. The mean fayalite mole fraction, X_{Fa} , ranges from 0.12 to 0.24, and the mean of the means is 0.169, in good agreement with the value of 0.157

found by Jones (1990). For most chondrules in Fig. 1, the modes are shifted to lower X_{Fa} than the medians, with the result that the frequency rises very steeply from the lowest X_{Fa} to the mode and falls much more gradually from the mode to higher X_{Fa} . In some chondrules, *e.g.* #696 and #7, rare compositions are found at lower X_{Fa} than the continuous parts of the histograms. Much more common are long, low, discontinuous, high- X_{Fa} tails extending to as high an X_{Fa} as 0.45.

The abundances of FeO in the mesostases of six of the above chondrules were determined by energy-dispersive analysis. In the SEM, a beam was rastered over areas $\sim 10\text{-}40\text{ }\mu\text{m}$ across having representative proportions of glass and quench crystals. From three to six areas were analyzed in each chondrule. Average FeO contents of the chondrule mesostases were found to range from 5.1 to 9.5 wt%, with an overall average of 7.4 ± 1.7 wt%. These values are quite similar to those obtained by Jones (1990).

ISOTOPIC COMPOSITIONS OF CHONDRULES

Magnesium isotopic compositions of chondrules in the Allende CV3 chondrite were measured by Galy *et al.* (2000) and Young *et al.* (2002) against the SRM980_O standard and by Bizzarro *et al.* (2004) against the DSM3 standard. Because the DSM3 standard has a very similar Mg isotopic composition to the Orgueil and Allende carbonaceous chondrites (Galy *et al.*, 2003), measurements made with DSM3 are considered to be relative to average solar system matter. Because Galy *et al.* (2003) found that SRM980_O has a mean $\delta^{25}\text{Mg}$ of -1.78 ‰ when measured against DSM3, the Galy *et al.* (2000) and Young *et al.* (2002) data were corrected according to $(\delta^{25}\text{Mg})_{DSM3} = (\delta^{25}\text{Mg})_{SRM980_O} - 1.78$. While Galy *et al.* (2000) and Bizzarro *et al.* (2004) analysed whole chondrules, Young *et al.* (2002) performed multiple analyses of individual spots within chondrules by laser ablation. A simple average was made of all spots within each chondrule measured by Young *et al.* (2002), and all data from the three studies are plotted on Fig. 2, from which it can be seen that $\delta^{25}\text{Mg}$ varies from -0.6 to $+1.0\text{ ‰}$ in individual chondrules, with a slight bias toward positive values. No significant difference in $\delta^{25}\text{Mg}$ can be discerned between PO and barred olivine (BO) chondrules. Which are Type I and which are Type II is unknown.

The only Si isotopic data for individual chondrules are those reported from Allende by Clayton *et al.* (1983). These were measured relative to NBS-28 but have been renormalized relative to mean solar system matter (ss) according to $(\delta^{29}\text{Si})_{ss} = (\delta^{29}\text{Si})_{\text{NBS-28}} + 0.275$, as in Grossman *et al.* (2000). Chondrules whose bulk FeO content is ≤ 8 wt % were reclassified as Type I and those whose FeO > 8 wt% as Type II, and the data are plotted in Fig. 3. All of the chondrules have $\delta^{29}\text{Si}$ within ± 0.4 ‰ of average solar system matter and are approximately evenly distributed about $\delta^{29}\text{Si}=0$. The Si isotopic compositions of Type I chondrules are indistinguishable from those of Type IIs. None of the measured chondrules are known to be porphyritic.

Shown in Fig. 4 are K isotopic compositions measured for an Allende chondrule by Humayun and Clayton (1995) and in individual chondrules from the Bishunpur L/LL3.1 chondrite (Alexander *et al.*, 2000) and Semarkona (Alexander and Grossman, 2005). In the latter two studies, chondrules were found to be internally heterogeneous in K isotopic composition, so a mean for each chondrule was obtained by weighting the different analyses from each by the inverse square of their 1σ uncertainties. Humayun and Clayton (1995) found that the K isotopic composition of average chondrites was indistinguishable from their chemical standard and that the average K isotopic composition of terrestrial materials was nearly so. Because Alexander *et al.* (2000) and Alexander and Grossman (2005) used a terrestrial basalt glass standard, all data in Fig. 4 are assumed to be relative to mean solar system matter. The chondrules range in $\delta^{41}\text{K}$ from $+12$ ‰ to -6 ‰, with more positive than negative values and a mean of $+1.5$ ‰. Almost all Type II chondrules have positive $\delta^{41}\text{K}$, while Type Is are more evenly distributed about normal K. This is particularly true of the porphyritic chondrules.

Literature data for the Fe isotopic compositions of individual chondrules from carbonaceous and ordinary chondrites are plotted in Fig. 5. The data of Mullane *et al.* (2005) and Zhu *et al.* (2001) were reported relative to the IRMM-014 standard and those of Kehm *et al.* (2003) relative to the Kil1919 standard. Because IRMM-014 has an Fe isotopic composition very close to that of mean solar system matter (Dauphas and Rouxel, 2005), the Kehm *et al.* (2003) data were re-normalized to IRMM according to $(\delta^{56}\text{Fe})_{\text{IRMM}} = (\delta^{56}\text{Fe})_{\text{Kil1919}} + 0.078$ (Dauphas and Rouxel, 2005). All of the chondrules

have $\delta^{56}\text{Fe}$ within ± 0.8 ‰ of that of mean solar system matter, and are close to normally distributed about $\delta^{56}\text{Fe}=0$. Little difference in $\delta^{56}\text{Fe}$ can be discerned between Types I and II chondrules, nor between porphyritic and barred chondrules.

THERMAL EVOLUTION IN WATER-RICH SHOCK WAVES

General Considerations

Solar nebular shock waves are among the leading candidates for the heat source needed for production of meteoritic chondrules (Ciesla, 2005). This is because various models have demonstrated that the thermal evolution of condensed matter in such shock waves is consistent with the rapid heating, peak temperatures and rapid cooling inferred from chondrule properties for chondrule formation (Hood and Horanyi, 1991; 1993; Iida *et al.*, 2001; Desch and Connolly, 2002; Ciesla and Hood, 2002; Ciesla *et al.*, 2003). Furthermore, the conditions to which chondrules are exposed during processing in nebular shock waves allow such properties as chondrule size and the frequency of compound chondrules to be explained (Desch *et al.*, 2005).

Descriptions of the processing of chondrules in shock waves may be found in Desch *et al.* (2005) and the references therein. Here are reviewed only those aspects needed to understand the dependence of the thermal evolution on those nebular parameters important for this work. In an undisturbed nebula, chondrule precursors and nebular gas are in both thermal and kinetic equilibrium. That is, they are at the same temperature and have no velocity with respect to one another other than that which arises due to the pressure gradient that exists in the gas (Weidenschilling, 1977; Cuzzi and Weidenschilling, 2006). A shock wave that passes through the nebula disturbs this equilibrium state because the gas, upon passing through the shock front, changes from a low-density, low-temperature state in which it is moving with high velocity (in the reference frame of the shock front) to a high-density, high-temperature state in which it is moving with low velocity. The solid precursors, however, are unaffected by passing through the shock front, thus retaining their high velocity. Because the precursors are immersed in the shocked gas, energy and momentum are exchanged between them until a

new equilibrium state is achieved. This results in the solids being heated due to frequent, energetic collisions with the gas, which cause the relative gas-solid velocity to decrease.

Radiation is important in the processing of condensed matter in shock waves. Even before encountering the shock wave, chondrule precursors are heated by radiation that escapes from behind the shock front and propagates upstream. The precursors in turn heat the gas with which they are in contact. Radiation from the hottest solids, those immediately behind the shock front, also propagates downstream to the precursors that already achieved a new equilibrium with the gas, keeping them warm and slowing the rate at which they cool radiatively.

All thermal histories used in this work were calculated using the model described in Ciesla *et al.* (2003), which allows the nebular water abundance to be varied. Unless otherwise stated, solids were assumed to be present as 1 mm-diameter silicate spheres with densities of 3.3 g/cm^3 . The solar solid/gas mass ratio was taken to be 0.005 and the average solar H_2O/H_2 molecular ratio was taken to be 5×10^{-4} (Fedkin and Grossman, 2006). The water concentration is increased by simple addition of the desired amount of stoichiometric H_2O . When the water abundance is increased, both the density of the gas and its specific heat capacity increase. This model does not account for cooling of the gas due to line emission from water molecules, an effect that should be investigated in future studies (see discussion in Desch *et al.*, 2005). The likely impact of line emission by water molecules would be to increase the cooling rate of the gas immediately behind the shock front, where the gas is optically thin to certain lines emitted by the water molecules (Morris *et al.*, 2007). Given the high abundances of water and chondrule precursors considered here, however, the optically thin region would likely be much smaller than in solar-composition systems considered previously.

Chondrule Number Density

In the present work, all dust is assumed to be processed into chondrules, and a greater initial amount of dust is assumed to lead to a greater chondrule number density. Consequently, the terms “dust” and “chondrule precursors” are used interchangeably, as are “dust enrichment” and “chondrule enrichment”. During passage of a shock wave, the abundance of chondrule precursors affects the thermal evolution of the system in two

ways. First, a higher concentration of solids increases the optical depth of the nebular region where the shock propagates, meaning that photons emitted from solids will not travel as far before being absorbed by other solids. The radiation from behind the shock is also more intense due to the greater number of emitting chondrules, and the heating upstream of the shock is much more rapid as the radiation is concentrated into a smaller region of space. Thus, higher heating rates and higher pre-shock temperatures are reached with higher chondrule number densities.

As chondrules drift away from the hot chondrules immediately behind the shock, the intensity of the radiation to which they are exposed diminishes, and they cool. The rate at which chondrules drift away from the shock front does not vary significantly with the choice of model parameters. The higher the density of solids, the greater is the rate of decrease of the radiation intensity experienced by a drifting chondrule, causing the latter to be warmed by radiation from the hottest chondrules for a shorter period of time. As a result, the cooling rate of the chondrules increases with higher chondrule abundance.

The second way that chondrule abundance impacts the thermal evolution of the system is in the exchange of energy and momentum in the post-shock gas. As the chondrules move through the gas immediately behind the shock front, some of their kinetic energy is converted into the thermal energy of the gas. The resulting higher gas temperatures result in more energetic and frequent collisions between the gas molecules and the chondrules, causing the latter to achieve even higher temperatures. This feedback means that chondrules reach higher peak temperatures as the concentration of chondrules increases. The increase of pre-shock and peak temperatures and the increase in both heating and cooling rates with increasing dust enrichment can be seen in Figs. 6a and 6b. The higher post-shock temperatures resulting from increasing dust enrichment also lead to higher post-shock total pressures, as seen in Figs. 7a and 7b.

Shock Velocity

Greater shock velocities result in higher post-shock gas temperatures and densities, leading to more frequent and more energetic collisions between the solids and gas immediately behind the shock front and, consequently, to higher temperatures of chondrule precursors (Fig. 6c). The increased density behind the shock front also leads to

solids becoming more spatially concentrated once they establish a new equilibrium with the gas. As a result, with all other things being equal, greater shock velocities result in the post-shock volume being more optically thick, yielding more rapid cooling rates for the same reasons described above (Fig. 6c). The higher post-shock temperatures and densities resulting from increasing shock velocity also lead to higher post-shock total pressures, as seen in Fig. 7c.

Chondrule Size

Both heating and cooling rates of chondrules depend on their surface areas. Energy is gained by collisions with gas molecules and by absorption from the ambient radiation field, while energy is lost by radiation from the chondrule surface. Given that the heat gain and loss rates have the same dependence on chondrule surface area, the peak temperatures that chondrules reach are approximately independent of their size (Ciesla, 2006). The sizes of chondrules do affect the propagation of radiation through the shocked region. At constant dust enrichment, decreasing chondrule size by a factor of two results in a greater abundance of chondrules but merely increases the optical depth by a factor of two. Radiation is thus trapped in a smaller volume upstream of the shock front, leading to more rapid chondrule heating rates. Likewise, as chondrules cool by drifting away from the shock front, the optical depth between them and the shock front also increases more rapidly, resulting in faster cooling rates for smaller chondrules. Fig. 6d shows that decreasing chondrule size by a factor of two results in an increase in heating and cooling rates by about the same factor. Fig. 7d shows that chondrule size has a minimal effect on evolution of P^{tot} .

Initial Gas Pressure

As the gas crosses a shock front, its temperature, density and velocity change in accord with the Rankine-Hugoniot equations, with faster shocks resulting in higher temperatures and densities, and lower post-shock velocities. The changes in these properties are determined by the ratio of the shock velocity to the speed of sound in the gas (the Mach number) and the ratio of the specific heat of the gas at constant pressure to

that at constant volume. In an ideal gas, a good approximation for solar nebular gas, the latter ratio is independent of gas density. As a result, the gas density increases and the shock velocity decreases by the same factor across the shock front. All other things being equal, a greater initial pressure leads to a higher post-shock density, which leads to more frequent gas-dust collisions and a higher peak temperature. This is a very large effect that can be seen in Fig. 6e. Because of this, the shock velocity required to reach a specific peak temperature is a strong function of initial gas pressure. For example, in Fig. 6c, it is seen that a 3.5 km/s shock achieves a peak temperature of $\sim 1900\text{K}$ at an initial P^{tot} of 1.5×10^{-5} bar, while in Fig. 6a, even a 6km/s shock fails to reach this temperature at 1.5×10^{-6} bar. The higher post-shock density resulting from higher initial gas pressure also results in a greater concentration of solids behind the shock front, which leads to more rapid cooling, as noted above and illustrated in Fig. 6e. The higher post-shock temperatures and densities resulting from increasing initial gas pressure also lead to higher post-shock total pressures, as seen in Fig. 7e.

Water Concentration

In a gas of solar composition, the H_2O/H_2 molecular ratio varies with temperature and averages $\sim 5 \times 10^{-4}$ (Fedkin and Grossman, 2006). At constant pressure and temperature, increasing the water concentration by simple addition of water molecules reduces the number of moles/l of other species, most of which are H_2 and He. Because of the relatively high molecular weight of water, this increases the gas mass density. As a result, when chondrule precursors move through the gas immediately behind the shock front, the collisions they experience are more energetic, causing higher peak temperatures to be reached, as illustrated in Fig. 6f. Furthermore, the increase in water concentration results in the gas having higher heat content, requiring the system to radiate away more energy to cool. Thus, the cooling rates of solids processed in a shock wave decrease when the water concentration increases, when all other factors are held constant. The higher post-shock temperatures resulting from increasing water enrichment also lead to higher post-shock total pressures, as seen in Fig. 7f.

CHEMICAL MODELING TECHNIQUE

General Considerations

The mineralogical, chemical and isotopic changes of a chondrule during heating, melting and cooling are specific examples of a more general problem. When a clump of solids undergoes heating while immersed in a gas with which it is out of equilibrium, what phase changes occur, what changes in chemical and isotopic composition occur and how rapidly do these processes take place in relation to the rate of change of temperature and pressure? This section describes the technique employed herein to compute the answers to these questions. Changes in chemical and isotopic composition result from evaporation and condensation processes. As a result, the computation involves several steps. First, the molecular composition of the gas phase with which the condensed assemblage would be in equilibrium must be calculated. This is commonly referred to as a vapor pressure calculation. Next, the actual partial pressures of the same species in the ambient gas must be calculated. Finally, the rate at which matter is transferred between the condensed and gas phases in order to equalize the vapor and ambient pressures is computed. This is accomplished via the Hertz-Knudsen equation, employing rate information, known as evaporation coefficients, derived from laboratory experiments on the kinetics of evaporation of chondritic material.

Thermodynamic State of the Condensed Assemblage

The total system is assumed to consist of the following 17 elements: H, He, C, N, O, Na, Mg, Al, Si, P, S, K, Ca, Ti, Cr, Fe and Ni. Of these, the condensed assemblage is assumed to contain only O, Na, Mg, Al, Si, K, Ca, Ti, Cr, Fe and Ni. The computational engine for this calculation is the MELTS thermodynamic model of Ghiorso and Sack (1995). The bulk chemical composition, temperature and pressure of a condensed system uniquely determine its equilibrium phase assemblage. If the system contains iron, either the oxygen fugacity, f_{O_2} , must also be specified to determine the oxygen content of the assemblage, or the oxygen content of the assemblage can be used to determine its equilibrium oxygen fugacity. Because the oxygen content of the condensed assemblage is always known in the present calculations, the MELTS model is used to determine the

equilibrium assemblage by iterating on the oxygen fugacity until an assemblage is found whose oxygen content matches that of the actual assemblage. This yields the equilibrium weight and volume proportions of solid and liquid silicate, metal and oxide phases, their individual compositions and the activities of all components in the liquid phase(s). The equilibrium oxygen fugacity at which the assemblage is computed is also the equilibrium vapor pressure of $O_{2(g)}$ for the assemblage.

Calculation of Equilibrium Vapor Pressures

To calculate the equilibrium vapor pressures of all other molecules, the speciation of the gas phase that would be in equilibrium with the condensed assemblage, hereinafter referred to as the droplet, must be computed. For each element in the condensed assemblage, the vapor pressure of the monatomic species is uniquely determined from such relations as

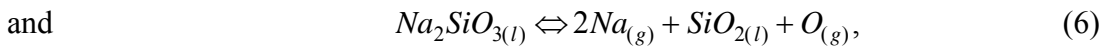
$$P_O = \sqrt{K_1 f_{O_2}}, \quad (1)$$

$$P_{Si} = K_2 a_{SiO_2} / f_{O_2} \quad (2)$$

and

$$P_{Na} = \sqrt{\frac{K_3 a_{Na_2SiO_3}}{a_{SiO_2} P_O}}, \quad (3)$$

where K_1 , K_2 and K_3 are the equilibrium constants for the reactions,



respectively, and a_{SiO_2} and $a_{Na_2SiO_3}$ are the activities of SiO_2 and Na_2SiO_3 , respectively, in the liquid phase.

The gas-phase speciation of the system can be described by a set of 17 mass-balance equations, one for each element i . In each such equation, the sum of the partial pressures of all species of element i , multiplied by their respective stoichiometric

coefficients, is defined as P_i^{tot} . In all calculations, P_H^{tot} is an input parameter. For all other elements entirely in the gas phase, *i.e.*, He, C, N, P and S,

$$P_i^{tot} = A(i)P_H^{tot} / A(H), \quad (7)$$

where $A(i)$ and $A(H)$ are the relative atomic abundances of elements i and H, respectively. For each of the other elements, those whose vapor pressures were determined in the previous paragraph, P_i^{tot} is a dependent variable. Examples of mass-balance equations for elements entirely in the gas phase are those for hydrogen,

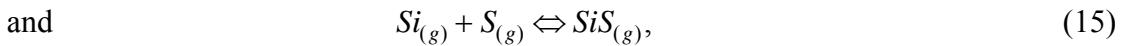
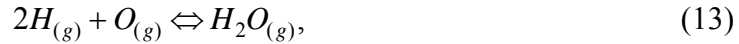
$$2P_{H_2} + 2P_{H_2O} + P_H + \dots = P_H^{tot}, \quad (8)$$

and sulfur,
$$P_{H_2S} + P_{SiS} + \dots = P_S^{tot}, \quad (9)$$

that become
$$K_4 P_H^2 + K_5 P_H^2 P_O + P_H = P_H^{tot} \quad (10)$$

and
$$K_6 P_H^2 P_S + K_7 P_{Si} P_S = P_S^{tot}, \quad (11)$$

respectively, where K_4 , K_5 , K_6 and K_7 are the equilibrium constants for the reactions,



respectively. Because P_O and P_{Si} are uniquely determined by the condensed phase assemblage, Equations (10) and (11) show that the mass-balance equation for each element i entirely in the gas phase introduces only one additional variable, the partial pressure of its monatomic species, P_i . After substitution of the value determined for P_i for each of the elements that do enter the condensed phase assemblage, a Newton-Raphson method is used to solve the resulting system of 6 simultaneous non-linear mass-balance equations for P_i for each of the elements that do not enter the condensed phase. When all P_i are known, the partial pressures of all species in the vapor that would be in

equilibrium with the droplet can be calculated simply using the equilibrium constants for their formation from their monatomic gaseous constituents. The 156 gaseous species carried in the present calculations are listed in Table 1. All thermodynamic data are from Chase (1998), except for several corrections as discussed by Fedkin and Grossman (2006).

Calculation of Partial Pressures in the Ambient Gas

Using the actual relative atomic abundances of the same 17 elements as in the previous computation to calculate all P_i^{tot} , the partial pressures of the same 156 molecular species are calculated by solving a system of 17 mass-balance equations *via* the Newton-Raphson method. Because none of the partial pressures are constrained to be in equilibrium with the droplet in this calculation, the resulting molecular speciation is that which would exist in the absence of the droplet.

Calculation of Liquid-Gas Equilibration Rates

The driving force for evaporation and condensation of a species i is the difference between its equilibrium vapor pressure, P_i^v , and its ambient partial pressure, P_i^a , and is expressed by the Hertz-Knudsen equation,

$$J_i = \frac{\gamma_i (P_i^v - P_i^a)}{\sqrt{2\pi M_i R T}}, \quad (16)$$

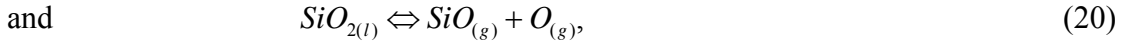
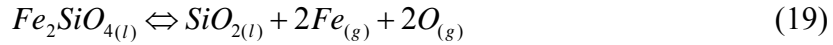
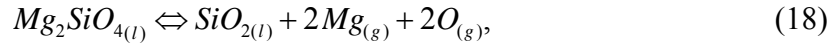
where J_i , M_i and γ_i are the flux in moles $\text{cm}^{-2} \text{sec}^{-1}$, molecular weight and evaporation coefficient of i , respectively, R is the gas constant and T is the absolute temperature. When $P_i^v > P_i^a$, the flux of i is positive, causing i to evaporate in an attempt to reduce P_i^v and increase P_i^a . When $P_i^v < P_i^a$, the flux is negative, and i condenses, causing P_i^a to fall and P_i^v to increase. When $P_i^v = P_i^a$, the system is at equilibrium, the flux is zero and there is no net evaporation or condensation of species i . The rate of mass transfer, J_i , between condensed and vapor phases is thus seen to be directly dependent upon two parameters, P_i^v and P_i^a , which are computed from thermodynamics only, and a third, γ_i , which must be determined experimentally and within which lies the kinetic information.

To calculate the total evaporation rate, J_j^t , of any element j , the evaporation rate of each species of that element, as given by Equation (16), must be multiplied by a stoichiometric coefficient, ν_i , and then summed together with the evaporation rates of all other species of that element, as in

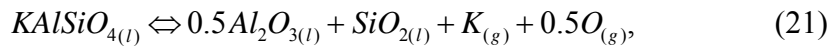
$$J_j^t = \sum_i \frac{\nu_i \gamma_i (P_i^v - P_i^a)}{\sqrt{2\pi M_i RT}}. \quad (17)$$

In this work, the total fluxes of Al, Ca, Ti and Cr are assumed to be zero.

Hashimoto (1983) performed vacuum evaporation experiments on molten chondrule analogs at several temperatures. Fedkin *et al.* (2006) interpreted the predominant evaporation reactions to be



and derived evaporation coefficients for these gaseous species from silicate liquid, and their temperature dependences, from these experiments. These coefficients are adopted in this study. $Ni_{(g)}$ is assumed to evaporate from silicate liquid in a completely analogous way to $Fe_{(g)}$, and with an identical evaporation coefficient. Yu *et al.* (2003) performed evaporation experiments on molten chondrule analogs in low-pressure air at 1723K, and measured the rates of Na and K loss with time. From these data, Fedkin *et al.* (2006) interpreted the evaporation reactions to be Equation (6) and



and derived evaporation coefficients for these gaseous species from silicate liquid, which are adopted here. Their temperature variations are unknown, and the evaporation coefficients of the alkalis were assumed to be invariant with temperature in the present work. Insufficient data are available from the above experiments to determine a distinct value of γ_i for each evaporating species of the same element. Thus, strictly speaking, the

derived value is determined largely by γ_i for the dominant evaporating species. In modeling chondrule analogs in this work, however, the same evaporation reactions were found to predominate as in the above experiments, justifying use of the experimentally determined value that was used in every term of Equation (17) for a given element.

Tachibana (pers. comm.) performed evaporation experiments on solid and liquid metallic Fe, and found that

$$\ln \gamma_{Fe(s,l)} = 1.43 - 2580/T, \quad (22)$$

which we adopt here. In this work, the evaporation coefficient of $Ni_{(g)}$ from solid and liquid metallic Ni is assumed to be identical to that of $Fe_{(g)}$ from metallic Fe. Crystalline silicate and oxide phases were assumed not to evaporate.

In some treatments, the numerator of Equation (16) is written as $\gamma_e P_i^v - \gamma_c P_i^a$, where γ_e and γ_c are evaporation and condensation coefficients, respectively, under the assumption that they may be different from one another. Because there is virtually no information on the values of condensation coefficients for reactions relevant to chondrule compositions, γ_c is always assumed to be identical to γ_e in this work.

Redox Equilibration

In the above treatment, evaporation is assumed to be stoichiometric; *i.e.*, when a cation evaporates from the silicate liquid, it is assumed to be accompanied by an amount of oxygen in stoichiometric proportion to it in its liquid oxide component, regardless of the identity of the dominant evaporating gas species of that cation. Hence, there is a stoichiometric flux of oxygen, J_O^{stoich} , defined as

$$J_O^{stoich} = 0.5J_{Na}^t + J_{Mg}^t + J_{Fe}^{ts} + 2J_{Si}^t + \dots, \quad (23)$$

where J_{Fe}^{ts} refers only to the flux of iron from the silicate liquid. There is also a total flux of iron from solid and liquid metallic iron alloys, J_{Fe}^m . Because of the different evaporation coefficients of Fe from silicate and metal, and the changing surface areas these phases have during heating and evaporation, the FeO/Fe^0 ratio and thus, the equilibrium f_{O_2} , change during evaporation. When the equilibrium f_{O_2} of the droplet is

different from the f_{O_2} of the ambient gas, there is a driving force for transfer across the droplet-gas interface of additional oxygen, unaccompanied by cations of elements in the droplet. This results in an additional redox flux of oxygen, J_O^{red} , such that

$$J_O^t = J_O^{stoich} + J_O^{red}, \quad (24)$$

where J_O^{red} is defined as

$$J_O^{red} = \frac{\gamma_O}{\sqrt{2\pi RT}} \left[\frac{(P_{H_2O}^v - P_{H_2O}^a)}{\sqrt{M_{H_2O}}} + \frac{(P_O^v - P_O^a)}{\sqrt{M_O}} + \frac{(P_{CO}^v - P_{CO}^a)}{\sqrt{M_{CO}}} + \frac{2(f_{O_2} - f_{O_2}^a)}{\sqrt{M_{O_2}}} + \dots \right], \quad (25)$$

in which there is a term for each oxygen-bearing gaseous species that does not also contain a condensable cation. In Equation (25), the equilibrium f_{O_2} of the droplet and $f_{O_2}^a$ are substituted for $P_{O_2}^v$ and $P_{O_2}^a$, respectively. In all cases investigated in this study, the $(P_{H_2O}^v - P_{H_2O}^a)$ term is more than an order of magnitude larger than all other terms in Equation (25), and this term is correlated with $(f_{O_2} - f_{O_2}^a)$. Thus, when the equilibrium f_{O_2} of the droplet is greater than the ambient f_{O_2} , oxygen evaporation occurs. When the ambient f_{O_2} is greater than the equilibrium f_{O_2} of the droplet, condensation of oxygen occurs. In this way, reduction of $FeO_{(l)}$ is modeled as oxygen evaporation, and oxidation of metallic iron as oxygen condensation.

In order to model the rate of redox change, the value of γ_O must be known. Ideally, this would be based on measurements of the oxidation rate of Fe in NiFe beads of known surface area in contact with a ferromagnesian silicate melt of known surface area, when both are exposed to a low-pressure mixture of H_2O and H_2 at a known temperature and f_{O_2} . Although such information is unavailable, an experiment by Everman and Cooper (2003) suggests that metal-silicate redox reactions occur on short time-scales. They observed formation of a significant amount of metallic iron in only 30 minutes at 1628K when they exposed an oxidized iron-bearing silicate melt to a $CO-CO_2$ gas mixture whose $\log f_{O_2}$ of $\sim IW-2.7$ was more than one log unit below the equilibrium f_{O_2} of the melt. Furthermore, chondrules themselves provide useful clues that the oxidation

state of iron changed during their formation. Low-fayalite cores in olivine phenocrysts in Type II chondrules (Jones, 1990) and dusty olivine grains in Type I chondrules (Jones, 1994) are interpreted as relict grains of solid precursors in which the oxidation state of iron differs from the bulk of the material in their host chondrules. Their presence suggests that at least partial oxidation of metallic iron and reduction of FeO occurred on the time-scale of chondrule formation. The values of γ_{Mg} , γ_{Si} and γ_{Fe} are all close to 0.3 at 2000K, and assigning the same value to γ_O at this temperature and giving it the same $\ln \gamma$ vs $1/T$ dependence as that for Si ensures that the oxidation state of iron changes on the time-scales of chondrule melting explored in this work.

Evaporation-induced isotopic fractionations

Isotopic fractionation factors employed in this study were measured in vacuum evaporation experiments of liquid chondrite analogs for Fe at 1700°C (Dauphas *et al.*, 2004), Si at 1800°C (Wang *et al.*, 2001) and Mg at 1800°C and 2000°C (Wang *et al.*, 2001), and in vacuum evaporation experiments of CAI analogs for Mg at 1600, 1700 and 1900°C (Richter *et al.*, 2007). The isotopic fractionation factor measured in these experiments for one pair of isotopes was used to calculate those of the other pairs of isotopes of the same element by writing the Rayleigh equation in δ notation and expressing simple proportional relationships between the δ values of the different pairs. Separate evaporation coefficients for each isotopologue were then derived by writing Equation (16) to express the flux of each isotopologue of the dominant evaporating species of each of Mg, Si and Fe, and then equating the total flux of that species to the sum of the fluxes of all isotopologues of that species. Of these elements, Mg is the only one known to have a temperature-dependent isotopic fractionation factor. Thus, in this work, it is the only one whose dominant evaporating species have temperature-dependent evaporation coefficients. In the model, the isotopic compositions of droplet and coexisting gas were calculated by using the separate evaporation coefficients derived herein to write Equation (16) for the flux of each isotopologue of the dominant evaporating species.

Isotopic fractionation factors equal to the square root of the inverse mass ratios have been observed for evaporation of K from molten stony cosmic spherules (Taylor *et*

al., 2005) and determined experimentally for evaporation of iron from metallic solid iron (Tachibana *et al.*, 2007). Such mass-dependent isotopic fractionations are implemented in the model calculations by using the evaporation coefficient for the dominant evaporating species of an element for each isotopologue of that species when writing Equation (16) for the flux of each. It is assumed here that the isotopic composition of a droplet of liquid metallic iron evolves according to the fractionation factor found for solid metallic iron. It is also assumed, however, that solid metallic iron is isotopically unfractionated during evaporation due to the inability of diffusion to homogenize isotopically fractionated iron on grain surfaces with isotopically normal iron in grain interiors prior to total evaporative loss of surface material.

Composition of the chondrule precursor

The chondrule precursor is assumed to contain enough mass to yield a spherical droplet of initial radius ~ 0.05 cm when equilibrated at the initial temperature of 1400K. It is also assumed to contain chondritic proportions of Na, Mg, Al, Si, K, Ca, Ti, Cr, Fe and Ni, implying total condensation of each of these elements into the precursor, leaving none in the complementary ambient gas. The latter contains 100% of each of the H, He, C, N, P and S in the system initially, implying either that they did not condense into the dust or that they were totally volatilized prior to the precursor reaching its initial temperature. The initial partitioning of oxygen is determined by the f_{O_2} at which the precursor is assumed to have equilibrated at the starting temperature. Ideally, that $\log f_{O_2}$ should be set at less than $\sim IW-6.0$, or 6.0 log units below the iron-wüstite (IW) buffer, to simulate the conditions of formation of low-temperature, solar nebular condensates (Fedkin and Grossman, 2006) but this yields so little FeO in the assemblage that MELTS cannot function. When an initial $\log f_{O_2}$ of IW-2.6 is assumed instead, the precursor begins with 28.1 wt % Fe^o and 2.3 wt% FeO, and sufficient FeO remains in the silicate liquid through subsequent chemical evolution that MELTS is able to function continuously in the cases investigated in this work. The initial bulk chemical and mineralogical compositions of the droplet, as well as the chemical compositions of the different phases present in this assumed chondrule precursor, are shown in Table 2. Only 6% of the Fe is present as FeO. The amount of oxygen in the coexisting gas is calculated

by subtracting the amount of oxygen in dust of the composition in Table 2 from the system bulk composition. Jones (1990) described fayalite-rich cores in the olivine crystals of some Type II chondrules, suggesting that the precursors of those objects formed from more oxidized material than the bulk chondrules. This phenomenon was not considered in this work.

Composition of the total system

As seen in Figs. 2-5, isotopic mass-fractionations of relatively volatile elements in chondrules are very small to non-existent. Enriching the bulk composition of the system in dust relative to gas is an effective way of suppressing isotopic fractionation that might otherwise occur during heating and evaporation of chondrule precursors. This is because the fraction of a volatile element that need be evaporated in order to reach the equilibrium vapor pressure in the ambient gas becomes smaller with increasing dust enrichment. In the present work, the system was assumed to be enriched in dust by various factors between 300 and 600 relative to the gas compared to solar composition. The dust is assumed to be a low-temperature condensate that was processed into the chondrule precursor shown in Table 2. Thus, the dust composition is that in Table 2, augmented by the chondritic proportion of S that is assumed to have been degassed when the chondrule precursor was formed by heating the dust to 1400K, the starting point of the present calculations.

The purpose of the present work is to model formation of Type II chondrules. The olivine in these chondrules has an average X_{Fa} of 0.16 (Jones, 1990). At liquidus temperatures, the gas with which such chondrule compositions are in equilibrium must have $\log f_{O_2} \sim IW-1.5$, or about 5 log units more oxidizing than a system of solar composition. Grossman *et al.* (2008) reviewed two ways of creating cosmic gases more oxidizing than solar composition: by dust enrichment; and by water enrichment. When gas that is otherwise solar in composition is enriched in dust by factors of 300x and 600x, the extremes selected here for the purpose of suppressing isotopic fractionation, $\log f_{O_2}$ of the ambient gas reaches only $\sim IW-2.7$ and $\sim IW-2.6$, respectively, at chondrule liquidus temperatures. Therefore, in addition to these dust enrichments, the system was assumed to be enriched in water by a factor of 550. The amount added to the system was

calculated by multiplying by 549 the fractional abundances of hydrogen and oxygen that are present as water in solar gas at 10^{-3} bar and a temperature of 1800K, where there are no stable condensates. Relative atomic abundances in systems employed in this work are presented in Table 3. Data sources for solar composition are those given by Fedkin and Grossman (2006). For this water enrichment, 24% of the total additional oxygen in the system comes from the added dust and 76% from the added water at a dust enrichment of 300; 47% of the added oxygen is from the added dust at a dust enrichment of 600. The initial distribution of oxygen varies with the amount by which the system is enriched in water and dust; *e.g.*, for 600x dust and 550x water enrichment relative to solar composition, 37% of the oxygen is present initially in the droplet and 63% in the vapor for the chondrule precursor in Table 2.

Computational strategy

Because the equilibrium mineralogical composition of the chondrule precursor is calculated from MELTS at a specific temperature and f_{O_2} , the activities of all components and the volumes of all condensed phases are known. Because the bulk composition of the system is assumed and the distribution of all elements between the droplet and gas is known, the ambient gas composition is also known. The composition of the vapor that would be in equilibrium with the droplet; *i.e.*, the equilibrium vapor pressure of each species, is calculated from the activities of the components and from the composition and assumed P^{tot} of the surrounding gas in the manner described above. The actual molecular speciation of the ambient gas is also calculated as above from its elemental composition, temperature and P^{tot} . At the initial temperature and P^{tot} , the flux of each molecular species out of or into the droplet is calculated from Equation (16), and the total flux of each element from Equations (17) and (25). In order to calculate the rate of evaporation or condensation of each species or element, its flux must be multiplied by an appropriate surface area. The radius of the droplet and its total surface area are calculated from the sum of the volumes of all constituent phases. Table 2 shows that the starting assemblage contains 30 wt% NiFe alloy, which translates to 14 vol%. An initial radius of 3 μm is assumed for each grain of metallic NiFe, and the number of such grains is calculated from the initial total volume of metal and held constant until metal is

mechanically separated from the droplet at a late stage. It is assumed that five per cent of the metal grains reside on the surface of the droplet at all times, and that each consumes πr^2 of surface area. Metal thus occupies $\sim 30\%$ of the total surface area initially and is over-represented compared to its volume percent. The relative surface areas of non-metallic phases are assumed to be equal to their relative volumes. Silicate liquid is the only non-metallic phase assumed to evaporate. The fluxes of Fe and Ni associated with metallic NiFe are then multiplied by the surface area of metal, and the fluxes of all elements associated with silicate liquid by the surface area of that phase. In all cases in this study, the equilibrium f_{O_2} of the droplet is initially less than the ambient f_{O_2} , so the oxygen redox flux is multiplied by the surface area of metal in order to oxidize metallic Ni and Fe into $NiSi_{0.5}O_{2(l)}$ and $Fe_2SiO_{4(l)}$, respectively.

As seen in Fig. 6, the shock wave thermal histories investigated in this work are characterized by a long, pre-shock period with a near-linear, relatively low heating rate, followed by a very short period at the time of shock passage when the temperature spikes sharply upward and then sharply downward, reaching a base temperature, followed finally by a long period of near-linear, relatively slow cooling. During the long, pre-shock period, P^{tot} (Fig. 7) and, consequently, P_H^{tot} , rise logarithmically with time, spike sharply upward at the time of shock passage, then slightly downward, and are nearly constant during the post-shock period.

The chemical evolution of the droplet is calculated while the temperature and P_H^{tot} of the system change according to the input thermal history. No attempt was made in this work to account for differences in temperature between gas and droplet that are particularly large only during the very short duration of the temperature spike. Although the full thermal history calculation begins at a much lower temperature and P_H^{tot} , the chemical evolution calculation begins only when the temperature reaches 1400K, producing the instantaneous mineral assemblage given in Table 2. The starting P_H^{tot} for the chemical evolution calculation is that prescribed by the thermal history for the time corresponding to that temperature. A time step size corresponding to a temperature change of 0.3-3K is selected. Its size may vary from a fraction of a second to several minutes within a given model run, depending on the instantaneous rate of change of

temperature. The initial rates of evaporation and condensation calculated above for silicate liquid and metallic phases are multiplied by the initial time step size in order to calculate the absolute amount of each element crossing the droplet-vapor interface. The amount of each element evaporated from the droplet is subtracted from the initial amount present and added to the ambient gas, and the amount condensed, including oxygen, is subtracted from the ambient gas and added to the droplet. The fraction of each element's total system abundance is known in the vapor and in the droplet prior to the evaporation step, and the known fraction by which these amounts change during the evaporation step is used to adjust P_i^{tot} in the ambient gas using Equation (7). At the next time step, where temperature and P_H^{tot} are different from those in the previous step, the compositions of both the droplet and the ambient gas are also incrementally different due to evaporation and condensation during the previous time step. The equilibrium f_{O_2} of the droplet is found by iteration until an equilibrium assemblage is produced whose oxygen content matches the known oxygen content of the droplet to within 10^{-12} . This usually requires about 50 iterations. The equilibrium f_{O_2} so determined, together with the activities of this equilibrium assemblage and the new ambient gas composition, are used to compute a new set of vapor pressures for this time step. The speciation of the ambient gas is also calculated from its new elemental composition, and new fluxes are obtained. The sizes of the metal grains are allowed to change but not their number, and the relative surface areas of the phases are calculated for the new time step. The amounts of each element evaporated or condensed during this time step are calculated and, from these, the compositions of the droplet and ambient gas which will be used in the next time step.

Non-equilibrium melting

Hewins *et al.* (2005) reviewed the origins of chondrule textures. Barred chondrules form when the precursor is heated above its liquidus and all pre-existing solids are destroyed. Upon subsequent cooling, the absence of nuclei leads to supercooling, the phenomenon whereby crystallization does not begin until after the temperature falls below the equilibrium crystallization temperature. When melting of precursor solids is incomplete, their vestiges do not permit supercooling, and porphyritic chondrules result. Many porphyritic chondrules contain relict olivine grains, suggesting

that they experienced heating rates too high for complete equilibration of pre-existing solids with the liquid. In addition, the shock wave thermal histories investigated in the present work include periods of very rapid heating. For these reasons, a very simple approximation of non-equilibrium melting was incorporated into the present model. In this simulation, 50% of the non-metallic crystalline assemblage calculated to be present in the starting material at 1400K was assumed to be isolated chemically and isotopically from the equilibrating part of the system, consisting of the liquid plus the remaining solids. During the subsequent thermal history, it was assumed that the amount of isolated solids decreases, and the amount introduced into the equilibrating part of the system increases, linearly with the value of

$$\int_{t_o}^{t_f} T dt \quad (26)$$

where t_o is the time at which $T=1400\text{K}$ and t_f is the time when the temperature reaches the post-shock base of the temperature spike. If, however, clinopyroxene, orthopyroxene or feldspar dissolves totally in the equilibrating part of the system, the sequestered amount of that phase is assumed to fall linearly with temperature to zero over the next 20K. Whenever the equilibrium assemblage is partially molten at the peak temperature, the amount of sequestered olivine and spinel at t_f is assumed to be 2% of the original amount. In this way, the amount of sequestered solids decreases with increasing temperature and with increasing time spent above 1400K, and progressive equilibration of the sequestered solids continues during part of the cooling period. A small percentage of the final product consists of relict grains of olivine and spinel, and crystallization begins at the equilibrium crystallization temperature.

Because silicate liquid and metal are always assumed to be entirely in the equilibrating part of the system and these are the only phases allowed to evaporate, it is the equilibrating system that undergoes evaporative changes in its chemical and isotopic compositions during heating, while the sequestered fraction retains its original chemical and its normal isotopic composition. Because progressive equilibration of the droplet with increasing temperature and time is assumed to occur by gradual transfer of material from the sequestered fraction into the equilibrating fraction, the chemical and isotopic

compositions of the bulk droplet do not change as fast as they would if the entire droplet were assumed to be in liquid-crystal equilibrium from the beginning of the calculation. After its bulk chemical and isotopic compositions change at each time step, the equilibrating system is assumed to reach liquid-crystal equilibrium, and the isotopic composition of each element is equalized in every phase within it. Thus, even though the Fe isotopic compositions of the metal and silicate liquid phases evolve with different isotopic fractionation factors, the Fe isotopic compositions of all phases in the equilibrating system are equalized after each time step. This assumes that equilibrium and kinetic, metal-silicate and silicate-silicate Fe isotope fractionations are zero at chondrule melting temperatures, although evidence for small fractionations exists (Roskosz *et al.*, 2006; Theis *et al.*, 2008).

Fractional crystallization

Because the goal of this work is to model olivine chondrules, formation of all non-metallic phases other than olivine was suppressed during cooling, allowing a metastable liquid to persist to ~950-1050K, below which the MELTS model fails for technical reasons. Zoned olivine phenocrysts are direct evidence that Type II chondrules underwent fractional crystallization. In order to model this phenomenon, a very simple routine was adopted based on the assumption that, as the amount of solid olivine increases, individual crystals grow larger and the fraction of the olivine that is isolated from chemical communication with the liquid increases very rapidly with falling temperature, eventually reaching 100%. Specifically, during the cooling part of the thermal history, olivine crystallization is assumed to be an equilibrium process until the base of the temperature spike, T_o , is reached. Below this temperature, however, a percentage of the existing olivine is assumed to be isolated from further chemical and isotopic equilibrium with the liquid, and added to the sequestered assemblage, if any. This percentage is assumed to vary inversely with e^{T-T_o} , starting at zero at T_o , reaching 99% at T_o-90K , and leveling off at 100%, defined herein as 100% fractional crystallization, for the duration of the model run. Thus, during cooling, the equilibrating part of the system continues to undergo chemical and isotopic evolution due to transfer of material across the droplet-gas interface but it is not the only part of the system whose

composition changes. This is because the olivine and metal in the equilibrating part of the system equilibrate their chemical compositions and equalize their isotopic compositions with those of the liquid at each temperature step, and then a portion of the olivine from the equilibrating system is added to the sequestered fraction, changing the bulk chemical and isotopic compositions of the latter cumulatively. As a consequence, the isotopic composition of the sequestered fraction is always less evolved than the instantaneous isotopic composition of the equilibrating part of the system. Because Type II chondrules contain very little olivine with $X_{Fa} > 0.33$, further crystallization of this phase is suppressed after it reaches this composition.

Metal fractionation

On average, the total Fe/Si atomic ratio of Type II chondrules is only ~ 0.33 of that of CI chondrites (Jones, 1990; 1996). While substantial amounts of iron are lost from the droplet by evaporation during the heating stages of the thermal histories investigated in the present work, both metallic and oxidized iron begin to recondense into the droplet soon after the cooling stage begins. In order to produce the observed depletion in the Fe/Si ratio in the final product, it is assumed that 70% of all the metal grains are expelled from the droplet when the temperature falls to 1640K. The expulsion process is assumed to be related to that envisioned by J.N. Grossman and Wasson (1985) and Uesugi and Sekiya (2006) whereby globules of relatively dense liquid metal are lost from the immiscible silicate liquid while the droplet is spinning, although recent calculations (Uesugi *et al.*, 2008) suggest that rotation of the droplet may not be necessary for globule ejection. Below this temperature, it is still assumed that 5% of the remaining metal grains in the droplet are present on its surface, and that their total surface area controls the recondensation rates of metallic iron and nickel into the droplet. In addition, large fractions of the metallic iron and nickel recondense onto the independent metal grains at a rate controlled by their total surface areas. For the thermal histories investigated in this work, removal of the metal at 1640K ensures that the final droplet contains ~ 0.33 of the total iron in the system. In this work, the independent metal grains are referred to as “external metal”.

RESULTS AND INTERPRETATION

Formation Model for Type II Porphyritic Olivine (PO) Chondrules: Standard Case

As seen in Fig. 6f, a region of the solar nebula with initial P^{tot} of 1.5×10^{-6} bar and that is enriched in water and in 0.05 cm-radius dust clumps by factors of 550 and 600, respectively, relative to a system of solar composition reaches a pre-shock temperature of 1580K, a peak temperature of 1832K and a post-shock temperature at the base of the temperature spike of 1620K when traversed by a 6 km/sec shock wave. The corresponding pre-shock and final values of P^{tot} in Fig. 7f are 8.2×10^{-6} and 4.0×10^{-4} bar, respectively. The time of shock arrival is 234 minutes after the droplet reaches 1400K. These conditions, together with the assumptions discussed in previous sections, constitute what is referred to herein as the “standard case”. Discussed immediately below are the properties expected of the final product when the chondrule precursor is subjected to the standard case model. The effect on these properties of different conditions or assumptions is discussed later.

Because more than 50% of the silicate fraction melts upon heating and the peak temperature is less than 1960K, the liquidus temperature for the bulk chemical composition that the silicate fraction possesses by the time it reaches peak temperature, this thermal history is conducive to formation of porphyritic chondrules.

In Fig. 8, the fraction of each element evaporated is plotted as a function of time for this thermal history. Significant fractions of Na and K begin to evaporate before any other element, both of them are completely lost from the droplet before the time of shock arrival and they recondense very gradually over the next 12 hours, reaching virtually total condensation by the time the droplet cools to ~ 1000 K. In contrast, the percentages of Fe and Ni evaporated rise more gently with time and continue to rise for a period of time even after the shock arrives, reaching maxima of 27 and 9%, respectively. They recondense relatively quickly, becoming fully condensed when the droplet reaches ~ 1490 K. Perceptible percentages of the Si and Mg begin to evaporate only after the peak temperature is attained but reach maxima of only 0.34 and 0.10%, respectively, before recondensation begins. The reason why such small fractions of these elements evaporate is a combination of the relatively short time at peak temperature; the vapor pressures

being relatively low, due to the low peak temperature; and the ambient pressures of $\text{SiO}_{(\text{g})}$ and $\text{Mg}_{(\text{g})}$ becoming relatively high with very little evaporation, due to the high dust enrichment and high post-shock ambient P^{tot} .

For this thermal history, the variation of the equilibrium f_{O_2} of the droplet and the f_{O_2} of the ambient gas are plotted in Fig. 9 as a function of time while the droplet and gas approach redox equilibrium. The droplet is assumed to have equilibrated at a log f_{O_2} of IW-2.6 at 1400K. Given the elemental composition of the ambient gas, its log f_{O_2} at this temperature is IW-1.3. As temperature rises, the surface area of silicate liquid and the evaporation coefficient of FeO from it both increase, but so do the oxidation coefficient of metallic iron and the evaporation coefficient of $\text{Fe}_{(\text{g})}$ from it. As a result, the FeO concentration rises and, with it, the equilibrium f_{O_2} of the droplet. The uptake of oxygen by the droplet causes the f_{O_2} of the ambient gas to decrease in this temperature interval. During the sharp upward temperature spike from 1580 to 1832K at 234 minutes, melting of a large amount of orthopyroxene and olivine leads to a large change in silicate liquid composition but there is insufficient time for the oxygen content of the droplet to change significantly. This causes the equilibrium f_{O_2} to fall relative to IW just before the droplet reaches its peak temperature. When the peak temperature is reached, the difference in f_{O_2} between ambient gas and droplet, which is the driving force for oxidation, is very large, rapid oxidation occurs and the droplet f_{O_2} approaches that of the ambient gas. After they become equal at 331 minutes, the droplet and ambient gas remain in redox equilibrium for the remainder of the cooling history.

The resulting change in the bulk chemical composition of the droplet is plotted as a function of time in Fig. 10. Prior to shock passage, the relatively rapid decline in Na_2O and K_2O contents is caused by their evaporation, and the more gradual decrease in the content of metallic Fe is caused by a combination of evaporation and oxidation. The gradual increase in FeO content is due to the fact that the oxidation rate of metallic Fe is greater than the evaporation rate of FeO. Within the 2 minutes immediately after shock arrival, two things happen: seventy percent of the metallic NiFe grains are assumed to be mechanically separated from the droplet, causing the metallic Fe content to fall from 19 to 7 wt%; and recondensation of metallic NiFe and FeO begin. For the next 30 minutes,

there is a rapid drop in the metallic Fe content despite recondensation of significant amounts of metallic Fe. This, together with a rapid rise in the FeO content, is due to the high oxidation rate in the temperature interval 1640 to 1540K. The loss of metallic Fe by evaporation and mechanical removal causes a complementary increase in the concentrations of SiO₂, MgO, Al₂O₃ and CaO, oxides that are either calculated to evaporate negligibly or assumed not to evaporate. After 400 minutes, the Na₂O and K₂O contents gradually increase due to their slow recondensation into the silicate liquid. With slowly falling temperature, rising f_{O_2} and changing liquid composition, very gradual reduction of FeO to metallic Fe occurs until 840 minutes, followed by gradual oxidation.

The changing mineral proportions in the model droplet are illustrated in Fig. 11. The mineralogical composition given in Table 2 for the model droplet at 1400K, the starting temperature for chemical modeling, is divided into the assumed initial fractions of equilibrating and chemically sequestered (labeled “relict”) material in Fig. 11a. By the time the temperature has reached 1580K, the pre-shock base of the temperature spike (Fig. 11b), the fraction of relict material has fallen sharply, the feldspar and clinopyroxene have disappeared, the proportion of silicate liquid has risen from 8 to 16 wt%, and the proportion of NiFe alloy has fallen from 30 to 22 wt% due to its evaporation and oxidation. The amount of olivine has fallen slightly and, despite the temperature increase, the amount of orthopyroxene has increased from 21 to 30 wt% due to the increased availability of SiO₂ from feldspar dissolution. By the time the peak temperature is reached (Fig. 11c), all of the orthopyroxene and some of the olivine have dissolved in the silicate liquid, which now constitutes 51% of the droplet and 65% of the silicate fraction. The NiFe has melted completely but its amount has not fallen greatly because the time for the temperature to rise from 1580 to 1832K is too short to allow significant evaporation or oxidation. By the time the post-shock base of the temperature spike has been reached (Fig. 11d), large amounts of olivine have crystallized from the liquid, mechanical removal and recondensation of the metal have taken place and the metal has solidified. By the time the temperature has fallen to 1590K (Fig. 11e), more olivine has crystallized from the silicate liquid, 70% of the total olivine (labeled “fractionated”) has been chemically sequestered from the liquid, and some of the alloy has disappeared due to continued oxidation of the Fe. By the time the lowest temperature

of the chemical modeling has been reached (973K, Fig. 11f), more olivine has crystallized, all of it has been chemically isolated from the silicate liquid, and there has been a net loss of metallic NiFe. If quenching occurred at this temperature, the object would contain 68 wt% olivine, 26% glass, 4% metal and 2% spinel. This is very similar to the mineral proportions found in many Type II PO chondrules.

The change in silicate liquid composition accompanying the above mineralogical changes is shown as a function of time in Fig. 12. At 1400K, the initial liquid contains 67 wt% SiO₂, 12% Al₂O₃, 9% Na₂O, 5% CaO and 1% K₂O but only 4% MgO and <1% FeO. As clinopyroxene and feldspar dissolve into the liquid with increasing temperature, the CaO and Al₂O₃ contents of the liquid increase but the evaporation rates of the alkalis exceed the rates at which they are added to the liquid, and their concentrations fall. The SiO₂ content falls and the MgO content increases as the liquid gradually reacts with olivine to form orthopyroxene. The FeO content gradually increases as metallic NiFe is oxidized. The MgO content spikes upward and the SiO₂, CaO and Al₂O₃ fall sharply when orthopyroxene and olivine dissolve during the sudden rise in temperature at 234 minutes. These trends reverse themselves when large amounts of olivine begin to crystallize upon cooling. Shortly thereafter, the rate of increase of the FeO content increases as the oxidation rate of metal increases. Further evolution of the silicate liquid composition after 300 minutes is controlled by olivine subtraction and recondensation of alkalis. If quenching occurred at 973K, the glass would have the composition shown in Table 4, where it is compared with the average mesostasis composition in the nine Type II PO chondrules reported by Jones (1990) to be free of pyroxene laths. The agreement is very good. For each oxide except SiO₂, FeO, Cr₂O₃ and TiO₂, the concentration in the model liquid lies within the $\pm 1\sigma$ uncertainty of the mean concentration in the mesostasis of the average Type II PO chondrule.

The histogram of olivine compositions calculated to be preserved in the droplet at the final temperature of chemical modeling is shown in Fig. 13. The composition of the relict grains of the starting material is shown. Because the liquid is olivine-saturated at 1832K, the peak temperature, and there are many olivine nuclei present, crystallization of new olivine begins at 1832K. It is assumed that these grains have sizes small enough that they equilibrate with the liquid during cooling to the base of the temperature spike,

1620K, where preservation of their compositions due to crystal growth begins with the onset of fractional crystallization. The percentage of the olivine that is chemically sequestered from the liquid is assumed to increase with falling temperature, reaching 99% by 1530K. The compositions of the first olivine to be preserved by fractional crystallization and of the olivine in equilibrium with the liquid when fractional crystallization reaches 99% are indicated on the histogram. The mean X_{Fa} is 0.150, and the mode is at 0.133. The peak width at one-fifth maximum is ~ 0.05 . The histogram is very similar to that of Chondrule 5 in Semarkona, shown in Fig.1. In the continuous part of the calculated histogram, there is a steep rise from the lowest X_{Fa} to the mode and a much more shallow decline from the mode to higher X_{Fa} . This is characteristic not only of the histogram for Chondrule 5 but also of those for several other chondrules in Fig. 1, *e.g.* 8, 18, 6 and 696. The calculated histogram also has the long, low, high- X_{Fa} tail characteristic of chondrules 8, 18, 6 and 696.

The variations of $\delta^{25}\text{Mg}$ and $\delta^{29}\text{Si}$ with time are shown in Figs. 14 and 15, respectively. All of the Mg and Si are in the droplet at the beginning of the calculation. As seen in Fig. 8, although a slightly greater proportion of the Si evaporates than Mg, very little of each of these elements ever evaporates. Preferential evaporation of light isotopes causes $\delta^{25}\text{Mg}$ and $\delta^{29}\text{Si}$ of the gas to begin at $\sim -10.0\%$ and -8.6% , respectively, and $\delta^{25}\text{Mg}$ and $\delta^{29}\text{Si}$ of the equilibrating fraction of the droplet to become just barely positive. Evaporation of Mg and Si becomes more significant only after the peak temperature is reached, and $\delta^{25}\text{Mg}$ and $\delta^{29}\text{Si}$ of the equilibrating fraction and the bulk droplet become larger than those of the sequestered fraction that, at first, consists only of relict grains of the starting material that retain their normal isotopic compositions. Isotopic exchange between the ambient gas and the liquid causes the rates of increase of the $\delta^{25}\text{Mg}$ and $\delta^{29}\text{Si}$ of the equilibrating fraction to fall, and $\delta^{25}\text{Mg}$ and $\delta^{29}\text{Si}$ of the ambient gas to increase. Fractional crystallization of olivine from the heavy isotope-enriched liquid follows, causing the cumulative $\delta^{25}\text{Mg}$ and $\delta^{29}\text{Si}$ of the sequestered crystals to rise. Shortly thereafter, preferential recondensation of light isotopes causes $\delta^{25}\text{Mg}$ and $\delta^{29}\text{Si}$ of the equilibrating fraction to fall and those of the ambient gas to continue to rise. Continued fractional crystallization causes the cumulative $\delta^{25}\text{Mg}$ and $\delta^{29}\text{Si}$ of the sequestered fraction to fall. Because recondensation of Si is less complete

than that of Mg (Fig. 8), $\delta^{29}\text{Si}$ of the equilibrating fraction does not become as small as $\delta^{25}\text{Mg}$. As a consequence, the difference in $\delta^{29}\text{Si}$ between the sequestered fraction and the equilibrating fraction is much smaller than the difference in $\delta^{25}\text{Mg}$ during fractional crystallization, and $\delta^{29}\text{Si}$ of the sequestered fraction falls less than its $\delta^{25}\text{Mg}$. At the end of the model run, $\delta^{25}\text{Mg}$ and $\delta^{29}\text{Si}$ of the bulk droplet are $\sim -10^{-5}\text{‰}$ and 10^{-4}‰ , respectively. These values are well within the ranges observed for $\delta^{25}\text{Mg}$ in PO chondrules in Fig. 2 and for $\delta^{29}\text{Si}$ in the chondrules in Fig. 3. The 0.5 ppm of the total Mg that is still in the gas has $\delta^{25}\text{Mg}$ of 53‰, and the 0.2% of the total Si remaining in the gas has $\delta^{29}\text{Si}$ of -0.24‰.

The variation of $\delta^{41}\text{K}$ with time is shown in Fig. 16. Feldspar is the only K-bearing crystalline phase in the initial mineral assemblage and is also the low-melting component. Initially, K evaporates quickly from the liquid, producing a vapor with initial $\delta^{41}\text{K}$ of -25‰ and causing $\delta^{41}\text{K}$ to increase rapidly in the equilibrating system while sequestered feldspar retains normal K isotopic composition. The vapor becomes less negative as $\delta^{41}\text{K}$ of the equilibrating system rises to 73‰. At this point, the last feldspar remaining in the equilibrating fraction melts, and feldspar in the sequestered fraction is assumed to be added selectively to the equilibrating system over the next 20K, where it melts instantaneously. This causes normal K to be added to the liquid so quickly in this temperature interval that $\delta^{41}\text{K}$ of the equilibrating fraction falls even as K is evaporating from it. When K is exhausted from the sequestered fraction at 150 minutes, the equilibrating fraction becomes the bulk droplet on this diagram. Because of K evaporation in the absence of further dilution by normal K, $\delta^{41}\text{K}$ of the bulk droplet rises to 60‰ before isotopic exchange with the ambient gas causes $\delta^{41}\text{K}$ to fall. Preferential recondensation of light isotopes begins shortly after shock passage, causing $\delta^{41}\text{K}$ of the droplet to become negative before reversing itself and gradually approaching zero while the gas becomes more positive as K condensation nears completion. At the end of the model run, 0.03% of the K remains in the gas, whose $\delta^{41}\text{K}$ reaches 125‰, and $\delta^{41}\text{K}$ of the droplet is -0.04‰, well within the range of values for the chondrules in Fig. 4.

The variation of $\delta^{56}\text{Fe}$ with time is shown in Fig. 17. Initially, iron evaporates rapidly from solid NiFe without isotopic fractionation and relatively slowly from silicate

liquid, producing a very small positive $\delta^{56}\text{Fe}$ in the equilibrating system and the bulk droplet and a small negative $\delta^{56}\text{Fe}$ in the ambient gas. The rate of Fe evaporation from metal increases relative to that from silicate with increasing temperature, causing $\delta^{56}\text{Fe}$ of the ambient gas to increase but, after ~ 77 minutes, the relative evaporation rate falls due to the increased surface area of silicate liquid, causing a greater rate of increase of $\delta^{56}\text{Fe}$ in the equilibrating system and the bulk droplet and a decrease of $\delta^{56}\text{Fe}$ in the ambient gas. The rapid temperature increase accompanying shock passage leads to a higher evaporation rate of Fe from silicate liquid and to the melting of metallic NiFe, from whose liquid evaporation of iron causes isotopic fractionation. As a result, $\delta^{56}\text{Fe}$ of the equilibrating system and bulk droplet increase more rapidly, reaching a maximum of 0.95‰, and that of the ambient gas decreases more rapidly, reaching a minimum of -2.57‰, shortly after shock passage. Isotopic exchange between the droplet and ambient gas causes $\delta^{56}\text{Fe}$ of the equilibrating system to fall and that of the ambient gas to rise. Shortly afterward, physical separation of 70% of the liquid metallic NiFe is assumed to occur, forming independent, external globules. At the same time, recondensation of FeO into the silicate liquid and of metallic Fe onto both the metal nuclei inside the droplet and the external metal causes $\delta^{56}\text{Fe}$ of the equilibrating system, the bulk droplet and the external metal to fall and that of the ambient gas to rise. This is followed by fractional crystallization of olivine that incorporates the Fe isotopic composition of the equilibrating system at this stage, causing $\delta^{56}\text{Fe}$ of the cumulative sequestered fraction to increase sharply and then fall gradually in tandem with that of the equilibrating system. At the end of the model run, <1 ppm of the total Fe is in the gas, 66.7% in the external metal and 21.2% in the sequestered fraction of the droplet. $\delta^{56}\text{Fe}$ of the gas is 0.47‰, of the external metal is -0.14‰, of the sequestered fraction 0.41‰, of the equilibrated fraction 0.07‰ and of the bulk droplet 0.29‰. The latter value is well within the range of values observed for the chondrules in Fig. 5.

The textures of porphyritic chondrules indicate that they crystallized without supercooling because of the presence of nuclei of preexisting solids. This means that precipitation of olivine began during cooling as soon as the liquid reached olivine saturation. For the thermal history investigated above, the liquid is saturated with olivine

at the peak temperature, and the maximum heavy isotope enrichments of the liquid occur shortly after cooling begins. Olivine that forms by fractional crystallization upon further cooling of such a droplet should preserve a continuous record of the isotopic composition of the liquid from which it crystallized, including part of the positive isotopic excursion of the liquid. Of the elements considered here, the alkalis suffer the greatest evaporative losses (Fig. 8). As a result, K exhibits the largest heavy isotope enrichment in the model droplet (Fig. 16), but only vanishingly small amounts of this element are incorporated into the crystallizing olivine. Mg and Si enter the olivine but their maximum heavy isotope enrichments are tiny (Figs. 14 and 15). Under the conditions of the model run, Fe is the most volatile of the elements that enter olivine and exhibits the largest heavy isotope enrichment. Fractional crystallization of olivine is calculated to begin when the droplet cools to 1620K and to continue to below 1530K. During this time period, $\delta^{56}\text{Fe}$ of the equilibrating fraction of the droplet is seen to fall from +0.8‰ to 0.1‰ (Fig. 17). Olivine that fractionally crystallizes from this system should record this progressive change in $\delta^{56}\text{Fe}$ with decreasing temperature of crystallization in the form of core-to-rim isotopic zoning, for example. The relative amount of olivine at each $\delta^{56}\text{Fe}$ preserved at the end of the model run is shown by the histogram in Fig. 18. Most of the olivine in the droplet has $\delta^{56}\text{Fe}$ between 0.50 and 0.75‰, while 5% has values that are more positive. The bulk olivine in the droplet has $\delta^{56}\text{Fe}$ of 0.47‰ and the bulk $\delta^{56}\text{Fe}$ of the droplet is 0.29‰. Thus, even though recondensation of iron ultimately may reduce $\delta^{56}\text{Fe}$ of the bulk droplet to a very small value, that portion of the olivine that crystallized from the liquid shortly after the degree of evaporation from the latter reached its maximum, and was prevented from further equilibration with it, still preserves a record of this event in its $\delta^{56}\text{Fe}$. While the range of $\delta^{56}\text{Fe}$ expected to be preserved should vary with thermal history, degree of dust enrichment, P^{tot} , degree of fractional crystallization of olivine, and other factors, the absence from porphyritic chondrules in the least equilibrated chondrites of olivine with significantly higher $\delta^{56}\text{Fe}$ than the bulk chondrules would be strong evidence that such objects did not experience Fe evaporation during their formation.

Sensitivity of Results to Model Assumptions

A model has thus been developed that reproduces many of the observed properties of Type II PO chondrules; namely, the bulk chemical composition, mineralogical composition, shape of the olivine composition histogram, chemical composition of the mesostasis and the bulk isotopic compositions of Mg, Si, K and Fe. In generating this result, however, many assumptions were made. What follows is a summary of a study of the sensitivity of the results to some of the major assumptions. This was done by re-running the model many times, in most cases by changing only one of the assumptions relative to those employed in the standard case described in detail above. Some of the assumptions are related to the physical and chemical properties of the droplet that have little effect on the thermal history, such as the droplet's initial redox state, the initial internal spatial distribution of metal relative to silicate, the degree of fractional crystallization of olivine and the oxidation rate of metallic iron as expressed *via* the value of γ_o . Other assumptions, such as the initial P^{tot} , shock velocity, chondrule radius and the degrees of dust and water enrichment, directly affect the thermal history. In order to isolate the chemical effects of changes in the degree of either the dust or water enrichment from those that would be caused by the resulting changes in thermal history, however, the runs conducted at different dust and water enrichments employed the same thermal history as the standard case. The justification for doing so is that the thermal history is not solely dependent on the dust and water enrichments. Rather, many different combinations of shock velocity, initial P^{tot} and degree of either dust or water enrichment can yield very similar thermal histories.

Degree of Dust Enrichment

If the thermal history is held constant and the degree of dust enrichment is reduced by a factor of two compared to the standard case, to a factor of 300 relative to a system of solar composition, the fraction of the iron that evaporates prior to its recondensation increases to 34% but the degree of evaporation of Mg and Si increase only very slightly. The mean X_{Fa} is 0.150, and the shape of the histogram (Fig. 19a) is little different from that of the standard case (Fig. 13) or of Chondrules 5 and 6 in Fig. 1. Relative to the standard case, $\delta^{56}\text{Fe}$ increases in the olivine and in the bulk droplet, but to

only 0.65‰ and 0.37‰, respectively. The latter value is well within the range of values observed for the chondrules in Fig. 5.

Assuming that quenching of the silicate liquid into glass causes immediate termination of K recondensation, it is assumed that liquid persists to a temperature at least as low as that required for complete recondensation of K, because there is no evidence for K depletion in Type II chondrules. The fraction of K in the gas is plotted against the FeO content of the liquid in the final steps of the model run in Fig. 20, and compared with similar curves for many other runs. As K recondenses into silicate liquid, the FeO content of the latter varies due to fractional crystallization of olivine and oxidation-reduction reactions. It is assumed that these chemical interactions also cease upon quenching of the silicate liquid, and that the FeO content of the resulting glass would be that reached by the liquid at the quench temperature. The range of FeO contents in mesostases of Type II PO chondrules is also shown in Fig. 20. Although the FeO content of the liquid can continue to evolve even after K recondensation is complete, model conditions are considered inappropriate for forming Type II PO chondrules if the FeO content of a model liquid lies well outside this range when K recondensation is at or near completion. In the present case of a dust enrichment of 300, the final liquid contains 5.9 wt% FeO, within the range of FeO contents in the mesostases of Type II PO chondrules.

Degree of Fractional Crystallization of Olivine

When the temperature interval over which the degree of fractional crystallization of olivine rises from zero to 99% is reduced to 40K from 90K, so that all olivine that precipitates below 1580K is immediately isolated chemically from the liquid, a sharper rise to and drop from the mode of the histogram is produced (Fig. 19b), resulting in a mean X_{Fa} of 0.139, well within the range for Type II PO chondrules. The sharp rise of the histogram makes it resemble most closely that of Chondrule 8 in Fig. 1. The final liquid contains 6.0 wt% FeO (Fig. 20), in the middle of the range of FeO contents of the mesostases of Type II PO chondrules. If instead the temperature interval is lengthened to 140K, so that fractional crystallization reaches 99% by 1480K, then the mean X_{Fa} becomes 0.160, the shape of the histogram (Fig. 19c) is little different from that of the

standard case (Fig. 13) or of Chondrules 5 and 6 in Fig. 1, and the final liquid contains 5.1 wt% FeO, just within the range observed for the mesostases of Type II PO chondrules. In neither case are the degrees of evaporation of Fe, Mg, Si or alkalis, or $\delta^{56}\text{Fe}$ of either the bulk olivine or the bulk droplet significantly different from the standard case.

Oxidation Coefficient

Shown in Figs. 19d and 19e are the effects on the olivine composition histogram of lowering γ_o , the oxidation coefficient, relative to the standard case by a factor of 3 at all temperatures, *i.e.* to 0.1 at 2000K, and increasing it by a factor of 2 at all temperatures, *i.e.* to 0.6 at 2000K, respectively. In the low- γ_o case, the oxidation rate of metal is slower and there is less FeO in the silicate liquid when olivine begins to fractionally crystallize than in the high- γ_o case. Because of this, the difference between the f_{o_2} of the ambient gas and the equilibrium f_{o_2} of the droplet is greater in the low- γ_o case but a lower value of γ_o must be used in Equation (25) to obtain J_o^{red} , the redox flux of oxygen. When fractional crystallization begins, J_o^{red} is a factor of 2.7 larger in the high- γ_o case but, because of a greater amount of prior oxidation in this case, must be multiplied by a 15% smaller surface area of metal to obtain the oxidation rate. The net effect is that the oxidation rate is 2.4 times greater in the high- γ_o case at the start of fractional crystallization. Fractional crystallization begins at the same temperature in both cases and produces the olivine in the main body of each histogram. Because of the higher oxidation rate in the high- γ_o case, the X_{Fa} of the olivine increases more quickly relative to the crystallization rate, resulting in an olivine composition histogram (Fig. 19e) in which smaller proportions of the olivine form within most composition bins at the lowest X_{Fa} than for the low- γ_o case (Fig. 19d). Because the f_{o_2} difference becomes smaller as time passes, the oxidation rate slows, and the proportion of the olivine within each bin increases with increasing X_{Fa} but reaches the mode after fewer bins in the low- γ_o case. The mean X_{Fa} is 0.115 and 0.170 in the low- and high- γ_o cases, respectively, values that bracket that of the standard case and are within the range of Type II PO chondrules. The shapes of all three histograms are similar to one another, with that for the standard case

being closer to the high- γ_o case. Of the chondrules in Fig. 1, they most closely resemble # 5 and 6. The final FeO contents of the liquids are 6.0 and 5.5 wt% in the low- and high- γ_o cases, respectively, also within the range observed in the mesostases of Type II PO chondrules (Fig. 20). Because the equilibrium f_{O_2} of the droplet is generally lower in the low- γ_o case than in the standard case, the vapor pressures of lithophile elements are higher but, due to the higher metal abundance, the time-averaged surface area of silicate liquid is lower, resulting in only slightly more evaporation of lithophiles than in the standard case. The opposite effects are seen in the high- γ_o case. In neither case is $\delta^{56}\text{Fe}$ of either the bulk olivine or the bulk droplet very different from the standard case.

Degree of Water Enrichment

If the thermal history is held constant and the degree of water enrichment is reduced to a factor of 350 relative to a system of solar composition, the initial $\log f_{O_2}$ of the ambient gas becomes IW-1.7. Because the equilibrium f_{O_2} of the initial droplet is the same as in the standard case, the difference in f_{O_2} between it and the ambient gas is smaller and the oxidation rate of the metal slower, causing the proportion of the olivine to rise rapidly toward the mode of the composition histogram with increasing X_{Fa} , as in the low- γ_o case above. The shape of the histogram is again like those of Chondrules 5 and 6 in Fig. 1 but the mean X_{Fa} falls to 0.109 (Fig. 19f), close to the arbitrary boundary between Types I and II chondrules. The final liquid contains only 2.1 wt% FeO (Fig. 20), well outside the range observed for the mesostases of Type II PO chondrules but very similar to the values found in those of Type I chondrules by Jones and Scott (1989). Although the equilibrium f_{O_2} of the droplet is generally lower than in the standard case, the degrees of evaporation of Mg and Si are only slightly larger. $\delta^{56}\text{Fe}$ of both the bulk olivine and the bulk droplet are very similar to the standard case.

Temperature of Mechanical Separation of Metal

When the temperature at which metal grains are physically separated from the droplet is increased from 1640 to 1690K, there is very little difference in the chemical and isotopic evolution of the droplet compared to the standard case (Fig. 20). In this

case, 70% of the metal grains must be removed in order for the bulk Fe/Si ratio of the droplet to end up at 0.33 relative to C1 chondrites. Iron evaporation continues for a short time after metal removal, and $\delta^{56}\text{Fe}$ of the external metal and of the bulk droplet evolve to -0.09‰ and 0.18‰ , respectively, by the end of the model run, both very similar to the standard case. When the temperature of removal is lowered to 1590K, however, the olivine composition histogram undergoes a major change. This is because, in this case, the very large amount of fractional crystallization of olivine that occurs between 1620 and 1590K does so in the presence of much greater amounts of metal than in the previous and standard cases. Consequently, the oxidation rate of metal is much greater in the earliest stages of fractional crystallization of olivine due to the much greater surface area of metal compared to the standard case. As in the high- γ_o case, when the oxidation rate is large compared to the crystallization rate, X_{Fa} increases before much olivine forms in each low- X_{Fa} bin but, as the droplet approaches redox equilibrium with the ambient gas and the oxidation rate slows, progressively more olivine forms within each bin and the fraction of the total olivine moles gradually increases, forming a gradual incline toward the mode of the histogram with increasing X_{Fa} . In this particular case, the mean X_{Fa} increases to 0.179 and the resulting histogram becomes more gaussian in shape (Fig. 19g) than the one for the standard case (Fig. 13). Not only does this histogram resemble those of Chondrules 696 and 7 in Fig. 1 but the FeO content of the liquid at 975K is 7.8 wt%, within the range observed for the mesostases of Type II chondrules (Fig. 20). Because metal separation occurs after much recondensation of iron in this case, $\delta^{56}\text{Fe}$ of the metal is slightly less than that of the bulk droplet at the time of separation. After further evolution, $\delta^{56}\text{Fe}$ of the external metal and of the bulk droplet reach -0.09‰ and 0.17‰ , respectively, at the end of the model run. In both cases, $\delta^{56}\text{Fe}$ of the bulk droplet is well within the range of values observed for the chondrules in Fig. 5.

Higher Temperature

An attempt was made to investigate evaporation effects at temperatures high enough that they approached the liquidus more closely but not so high that all the FeO was lost, which would otherwise have caused the MELTS algorithm to fail. To do so, a thermal history was computed at a higher shock velocity, 6.75 km/sec, than the standard

case, a higher water enrichment of 640 relative to solar composition, and a lower initial P^{tot} of 1.0×10^{-6} bar. All other standard case conditions were retained both in the thermal history calculation and in the chemical evolution calculation. The resulting heating and cooling rates are 0.57 and 0.59 K/min, respectively, both slightly lower than for the standard case, but the pre-shock and peak temperatures and the post-shock base of the temperature spike, 1610, 1915 and 1645K, respectively, are all higher than in the standard case. The post-shock P^{tot} is 3.6×10^{-4} bar. As a result, the extent of melting of the silicate fraction increases to 86% and the degrees of evaporation of Fe, Mg and Si increase to 57%, 0.46 and 1.4 %, respectively. Due to the higher pre-shock temperature, a point is reached in this thermal history where the rate of evaporation of FeO exceeds the oxidation rate of the metal, causing the FeO content of the silicate liquid to fall just before the time of shock arrival. Compared to the standard case, the equilibrium $\log f_{O_2}$ of the droplet is lower by 0.10 at the time of shock passage, a factor that, together with the higher value of γ_O due to the higher peak temperature, increases the driving force for metal oxidation. As a consequence, X_{Fa} is lower when fractional crystallization of olivine begins, but the oxidation rate is faster, causing the olivine to increase its X_{Fa} much more quickly as crystallization proceeds. Compared to the standard case, the resulting olivine composition histogram (Fig. 19h) is shifted to higher X_{Fa} , yielding a mean value of 0.167, again with a more gradual rise toward the mode, as rapid oxidation does not allow large amounts of relatively low- X_{Fa} olivine to form. While the shape of the olivine composition histogram for this high-temperature case is similar to that of Chondrule 696, it is quite different from most of those observed for Type II PO chondrules in Fig. 1. At 980K, the final FeO content of the liquid reaches 8.8 wt % (Fig. 20), within the range observed for the mesostases of this type of chondrule. While the degrees of evaporation of Mg and Si are still small, much more iron evaporates compared to the standard case. As a result, iron isotopic exchange between vapor and droplet occurs earlier relative to fractional crystallization of olivine, the earliest olivine to form has $\delta^{56}\text{Fe} > 3.5\text{‰}$, pronounced core-to-rim zoning of $\delta^{56}\text{Fe}$ is produced in the olivine, whose bulk $\delta^{56}\text{Fe} = 1.27\text{‰}$, and $\delta^{56}\text{Fe}$ of the bulk droplet is 0.89‰, just beyond the range of values for the chondrules shown in Fig. 5.

Amount of Surface Metal

When 2% of the metal grains are assumed to reside on the surface of the droplet at all times, metal occupies 12% of the surface area of the droplet initially and is slightly under-represented compared to its volume %. Because the surface area of metal is less than in the standard case, less oxidation of metal occurs during the pre-shock heating period. As a result, the equilibrium f_{O_2} of the droplet is smaller and the difference between the f_{O_2} of the ambient gas and that of the droplet is greater than in the standard case when fractional crystallization begins. Although γ_o is the same and the driving force for oxidation is bigger, the surface area of metal is a factor of 2.5 smaller, and the oxidation rate is very similar to that in the standard case. The resulting mean X_{Fa} of 0.122 is within the range for Type II PO chondrules, and the shape of the histogram is very similar to that of the standard case (Fig. 19i). The final liquid contains 6.4 wt% FeO, within the range observed for the mesostases of Type II PO chondrules. With less metal coating the surface, less Fe evaporates (~19%) than in the standard case, and slightly more of the Mg and Si evaporate due to the greater surface area of silicate liquid. $\delta^{56}\text{Fe}$ of the bulk olivine, external metal and bulk droplet are 0.31, -0.03 and 0.07‰, respectively, the latter value being within the range of those in Fig. 5. When 10% of the metal grains are assumed to be on the surface of the droplet at all times, metal is vastly over-represented on the surface, occupying 59% of the initial surface area, causing the oxidation rate to be much greater than in the standard case. Thus, at the start of fractional crystallization, the FeO content of the liquid and the equilibrium f_{O_2} of the droplet are larger. During fractional crystallization, the decrease in oxidation rate expected from the smaller difference between the f_{O_2} of the ambient gas and that of the droplet compared to the standard case is offset by the greater surface area of metal. As a result, the shape of the olivine composition histogram is very similar to the standard case but the mean X_{Fa} is 0.164 (Fig. 19j). Although this value lies within the range for Type II PO chondrules, the FeO content of the final liquid, 5.0 wt% at 980K, lies just within the range observed for their mesostases. The increased surface area of metal results in more evaporation of Fe (~42%) but less of Mg (0.07%) and Si (0.25%) than in the standard case. The resulting $\delta^{56}\text{Fe}$ of the bulk olivine, external metal and bulk droplet are 0.78, -0.32 and 0.64‰,

respectively, the latter value being well within the range observed in Fig. 5. A maximum core-to-rim difference of 1.25‰ would be expected in the olivine crystals.

Chondrule Size

The difference between this case and the standard case was not only that the initial chondrule radius was reduced to 0.25 from 0.5 mm but that the thermal history appropriate for this chondrule radius was also adopted. Although the pre-shock and peak temperatures as well as that of the post-shock base of the temperature spike are only slightly lower for this thermal history than in the standard case, the heating and cooling times are shorter (Figs. 6d and 7d). For this chondrule size, when 5% of the metal is assumed to reside on the surface of the droplet at all times, as in the standard case, the fraction of the surface area initially occupied by metal falls from 30 to 15%, and the fraction occupied by silicate liquid rises from 10 to 12%. Compared to the standard case, the smaller surface area of metal results in a lower initial oxidation rate, and the olivine composition histogram (Fig. 19k) has features similar to that for the case of diminished surface area of metal (Fig. 19i). Accordingly, the X_{Fa} for both the beginning of the continuous part of the histogram and the mean are lower, 0.075 and 0.129, than for the standard case but the shape of the histogram is very similar to that in the standard case. The final liquid contains 6.6 wt% FeO, within the range observed in the mesostases of Type II PO chondrules. With substantially less metal coating the surface, less Fe evaporates (~16%) than in the standard case. The combined effects of an ~50% shorter evaporation time and a greater surface area to volume ratio of silicate liquid lead to only slightly more Mg (0.10%) and Si (0.40%) evaporation than in the standard case. $\delta^{56}\text{Fe}$ of the bulk olivine, external metal and bulk droplet are 0.24, 0.01 and -0.01‰, respectively, the latter value being well within the range observed in Fig. 5.

Initial Redox State of the Droplet

When the starting material is assumed to form at $\log f_{O_2} = \text{IW}-1.45$ instead of $\text{IW}-2.6$, the value used in the standard case, the droplet begins with only 20.6 wt% metallic NiFe and 13.1 wt% FeO, instead of 30 and 2.31 wt%, respectively. For this example, the dust with which the system is enriched is assumed to have the same composition as in the

standard case. In this way, the oxygen content of the total system is the same, and the additional oxygen in the starting assemblage of the droplet at 1400K is assumed to have been removed from the ambient gas through processing of the chondrule precursor during heating to 1400K, resulting in an initial $\log f_{O_2}$ of IW-1.35 in the ambient gas. The X_{Fa} of olivine in the starting material is 0.22. Compared to the standard case, less Fe evaporates because there is less metal, and even less Mg and Si evaporate because the higher equilibrium f_{O_2} s during heating result in lower vapor pressures of $Mg_{(g)}$ and $SiO_{(g)}$. Because there is a relatively small difference between the f_{O_2} of the ambient gas and the equilibrium f_{O_2} of the droplet initially, the droplet and ambient gas are in redox equilibrium with one another before fractional crystallization begins. At this point, the silicate liquid has more FeO in it compared to the standard case, shifting the olivine composition histogram to higher X_{Fa} , as seen in Fig. 19l. Because there is virtually no change in f_{O_2} during fractional crystallization, there is no oxidation-induced rise in the proportion of olivine with increasing X_{Fa} toward the mode. The result is a histogram with a sharp peak close to the lowest X_{Fa} . Although the mean X_{Fa} is 0.199, which is still within the range found for Type II chondrules, the shape of the histogram is quite unlike that of the standard case (Fig. 13), but it does resemble that of Chondrule 8 in Fig. 1. No relict olivine is discernible, as its X_{Fa} is within the range of fractionally crystallized olivine and is thus hidden within the main body of the histogram. In this case, however, growth of fractionally crystallized olivine whose X_{Fa} changes progressively from 0.18 to 0.33 upon relict cores with X_{Fa} of 0.22 would produce grains having fayalite-rich cores similar to those seen by Jones (1990). The FeO content of the last liquid, 6.4 wt%, is also well within the range observed in the mesostases of Type II chondrules, as seen in Fig. 20. $\delta^{56}Fe$ of the bulk olivine, external metal and bulk droplet are 0.40, -0.32 and 0.33‰, respectively. The latter value is within the range of those observed for the chondrules in Fig. 5.

DISCUSSION

When a 6 km/sec shock wave traverses a region of the solar nebula at an initial P^{tot} of 1.5×10^{-6} bar that is enriched relative to a system of solar composition by a factor

of 550 in water and by a factor of 600 in 0.05 cm-radius clumps of dust of chondritic composition in which only 6% of the iron is oxidized, it has been demonstrated that the product will probably have the bulk mineralogical, chemical and isotopic compositions of many Type II PO chondrules. The products will also have textures, olivine composition histograms and glass compositions very similar to these objects. Furthermore, these similarities are produced when the dust clumps are a factor of two smaller or start out with a factor of 6 more of their iron in oxidized form, or when the metallic NiFe starts out slightly under-represented on the surface of the resulting droplet, or over-represented by a factor of 4. They are produced when ~two-thirds of the metallic NiFe is mechanically separated at any temperature within a 100K range, over a wide range of values of the oxidation coefficient of metallic Fe from 0.1 to 0.6, and over a wide range of degrees of fractional crystallization of olivine.

If other factors were to compensate for the resulting consequences on the shock wave thermal history, the above similarities would persist at a dust enrichment only one-half as large but not at a water enrichment as low as 350 relative to solar composition, where the FeO content predicted for the mesostasis would fall below the range observed in Type II PO chondrules.

Different shock wave thermal histories, however, can have profound impacts on the properties of the final product. In particular, for the thermal history calculated for a 6.75 km/sec shock wave propagating through a system of initial $P^{tot}=1.0 \times 10^{-6}$ bar, a water enrichment of 640 relative to solar composition but the same dust enrichment as in the standard case (the “higher temperature” case, above), the heating and cooling rates are slightly smaller but the higher pre-shock, peak and post-shock temperatures lead to greater degrees of melting and evaporation. In this case, the degree of melting of the silicate fraction increased from 65% at 1832K, the peak temperature in the standard case, to 86% at a peak temperature of 1915K. The significant amount of unmelted olivine remaining at the peak temperature would have still produced a model chondrule with porphyritic texture. As seen above, however, fractional crystallization of olivine would have begun at an earlier stage of iron isotopic exchange, leading to preservation of olivine with elevated $\delta^{56}\text{Fe}$ that would have resulted in olivine with pronounced core-to-rim zoning in $\delta^{56}\text{Fe}$ and in a bulk chondrule with $\delta^{56}\text{Fe}$ of 0.89‰. The only iron isotopic

compositions of chondrule olivine available are the ion microprobe data of Alexander and Wang (2001). The closest thing to a Type II PO chondrule that was measured in that work is sample CHUa, whose olivine has X_{Fa} of 0.09. Only one 20-25 μm spot near the center of a chemically unzoned olivine crystal was analyzed, and it gave a $\delta^{57}\text{Fe}$ (relative to ^{56}Fe) of -0.2‰ with a 2σ error of $\pm 1.2\%$. On this basis, it is simply not known if the olivine in some Type II PO chondrules is significantly zoned in $\delta^{56}\text{Fe}$ but the bulk $\delta^{56}\text{Fe}$ of the model chondrule is outside the range observed for Type II PO chondrules in Fig. 5. Even if all relict olivine equilibrated with the rest of the droplet, there would still be unmelted olivine in this composition unless peak temperatures exceeded 1950 to 1960K. Thus, considering persistence of relict olivine, formation of PO chondrules from this composition is possible even for thermal histories whose peak temperatures are slightly in excess of 1960K, where even larger $\delta^{56}\text{Fe}$ would be expected in bulk chondrules, accompanied by even more pronounced $\delta^{56}\text{Fe}$ zoning of olivine. Because of the small values of $\delta^{56}\text{Fe}$ observed in Type II chondrules, it is concluded that Type II PO chondrules can form in shock waves at near-liquidus temperatures only if evaporation of Fe is significantly retarded, because of high initial P^{tot} and/or high dust enrichments. For example, in the high-temperature thermal history used above (the one computed for a shock velocity of 6.75 km/sec), a dust enrichment of 700x would be required to keep $\delta^{56}\text{Fe}$ of the bulk droplet within the observed range at an initial P^{tot} of 1.0×10^{-6} bar. Recall, however, that both higher initial P^{tot} and higher dust enrichments themselves cause temperatures to increase during shock wave passage and that, in particular, the effect on the thermal history of increasing the dust enrichment from 600 to 700x is not included in this calculation. For those Type II PO chondrules that formed in shock waves at near-liquidus temperatures, it is evident that the elevated initial P^{tot} and/or dust enrichment needed to retard Fe evaporation must be accompanied by shock velocities below 6.75 km/sec.

In all of the model runs in the present study, the weighted mean $\delta^{56}\text{Fe}$ of the external metal and the relatively small amount of metal remaining inside the Type II PO chondrule ranges from a minimum of -0.43‰ (for the case of the high-temperature thermal history) to a maximum of -0.02‰ (for the small chondrules case), and averages -

0.14‰. Thus, although H3 chondrites certainly contain metal processed through additional types of chondrules, *e.g.* Type I, barred, *etc.*, the present model predicts that Type II PO chondrule formation would not contribute metal of highly anomalous $\delta^{56}\text{Fe}$ to the bulk metal inventory of such chondrites. In an iron isotopic study of bulk metal separated from each of a suite of chondrites, Theis *et al.* (2008) found a $\delta^{56}\text{Fe}$ of $0.01 \pm 0.01\text{‰}$ for the H3 Clovis, the only Type 3 chondrite measured.

One property of Type II PO chondrules unable to be predicted by the models discussed herein is the Na content of their olivine. Alexander *et al.* (2008) found that the Na_2O concentrations of the most FeO-poor olivine crystal cores in ten Type II PO chondrules in Semarkona range from 0.0035 wt% to 0.0133 wt%, determined olivine-melt distribution coefficients for Na_2O from the chondrules and argued that these data imply that the chondrule liquids contained $\sim 1\text{-}2\text{ wt\% Na}_2\text{O}$ when the olivine began to crystallize. In contrast, 19 ppm Na_2O are predicted to be in the silicate liquid when olivine starts fractionally crystallizing in the standard case in the present work, many orders of magnitude lower than inferred by Alexander *et al.* From vapor pressures of Na calculated for these concentrations at liquidus temperatures, Alexander *et al.* (2008) estimated that the ambient pressures of Na necessary to hold these concentrations in solution in the melt require nebular dust concentrations that range from 72 to 534 gm/m^3 at 10^{-7} bar. In the present work, the equilibrium vapor pressure of Na was determined from Equation (6) for each of the ten Type II PO chondrule compositions given by Alexander *et al.* at its liquidus temperature for each of two values of $\log f_{\text{O}_2}$: IW and IW-1.4, the equilibrium $\log f_{\text{O}_2}$ of the model droplet at the beginning of fractional crystallization of olivine in the standard case in the present work. The ratio of the vapor pressure of Na to the partial pressure of Na in a system of solar composition at $P^{\text{tot}} = 10^{-3}$ bar and the same temperature ranges from 9×10^4 to 4×10^5 at IW, and from 2×10^5 to 8×10^5 at IW-1.4. When the Na vapor pressure is compared to its partial pressure in solar gas at 10^{-7} bar, the ranges of the ratios become $1\text{-}6 \times 10^9$ and $3 \times 10^9\text{-}1 \times 10^{10}$, respectively. These are the enrichment factors of dust relative to gas compared to a system of solar composition that would be required to maintain the Na contents of the chondrule liquids at their inferred levels under the stated conditions. Alternatively, if it is assumed, as in Alexander *et al.*, that the chondrules equilibrated their Na contents at liquidus

temperatures after 10% of the Na had evaporated from them, the dust enrichments that would be necessary to do so range from 5×10^5 to 4×10^6 at IW and from 1×10^6 to 8×10^6 at IW-1.4 compared to a system of solar composition at $P^{tot} = 10^{-3}$ bar. At 10^{-7} bar, the dust enrichments become 7×10^9 - 6×10^{10} at IW and 2×10^{10} - 1×10^{11} at IW-1.4. These are from 10 to 10^6 times greater than the largest enrichments of chondrule precursor dust predicted in solar nebular models to date, even under the most extreme conditions (Cuzzi *et al.*, 2001). Furthermore, based on extrapolation of existing nebular shock wave models, it is likely that the temperatures reached during passage of even the lowest-velocity shock waves through regions having such dust enrichments would lead to total evaporation of chondrule precursors. If the inferences of Alexander *et al.* (2008) are correct, non-nebular settings for chondrule formation should be seriously explored.

CONCLUSIONS

When a shock wave passes through a nebular region, temperatures, post-shock P^{tot} , heating rate and cooling rate all increase with increasing shock velocity, and with increasing dust enrichment or initial P^{tot} of the region. Increasing water enrichment leads to higher temperatures and post-shock P^{tot} , but lower cooling rates. Increasing chondrule size decreases heating and cooling rates. Many observed properties of Type II PO chondrules are produced when precursor dust in a region at $P^{tot} = 1.5 \times 10^{-6}$ bar is subjected to a nebular shock wave traveling at 6 km/sec. The ranges of mean X_{Fa} and of the FeO contents of mesostases of Type II chondrules require the droplet to have gradually equilibrated with an ambient gas with a water enrichment of ~ 550 relative to a system of solar composition (equivalent to a $\log f_{O_2}$ of \sim IW-1.4 at 1600K) but the presence of low- X_{Fa} relict grains requires the precursor to have formed under more reducing conditions (equivalent to a $\log f_{O_2}$ of \sim IW-2.6 at 1400K). The shapes of the olivine composition histograms require the degree of fractional crystallization to have increased with decreasing temperature. If the precursor is assumed to have had the chondritic total Fe/Si ratio, then several percent of the total metal is required to have been on the surface of the droplet at all times, and \sim two-thirds of the total metal is required to have been mechanically separated from the droplet at a temperature ranging from well above the

post-shock base of the temperature spike to several tens of degrees below it in order to produce the observed Fe depletion of Type II chondrules. Dust enrichments as low as 300 compared to solar composition suppress evaporation sufficiently to prevent development of isotopic mass-fractionations beyond the ranges observed in chondrules. At dust enrichments greater than this, evaporation of Mg and Si is minimal, even at the maximum temperatures that allow retention of olivine nuclei in this bulk composition, and isotopic mass-fractionation of K is small due to total recondensation of this element, probably requiring persistence of metastable silicate liquid to 950-1000K. Several tens of percent of the Fe evaporate at these dust enrichments but isotopic exchange with the droplet and recondensation at high temperature leave bulk isotopic mass-fractionations that are within the range observed for chondrules. For shock wave conditions that produce peak temperatures near the liquidus, however, fractional crystallization of olivine begins before Fe isotopic exchange is complete, a process that would have resulted in olivine that is zoned in $\delta^{56}\text{Fe}$ and a bulk droplet whose $\delta^{56}\text{Fe}$ lies outside the range observed for chondrules. Such mass-fractionations could be reduced at dust enrichments slightly higher than 600 compared to a system of solar composition, but the higher peak temperatures that would result from the higher dust enrichments would have to be offset by lower shock velocity and/or initial P^{tot} in order to keep peak temperatures below the liquidus so that the olivine nuclei needed to produce the textures of PO chondrules would be preserved.

ACKNOWLEDGMENTS

We thank the Musee Nationale d'Histoire Naturelle and the National Museum of Natural History for thin sections of the Semarkona meteorite, and H. Connolly, N. Dauphas and R. Hewins for helpful discussions. This work was supported by NASA Grants NNX08AG27G (to FJC), NAG5-11588 (to LG) and NNG05GG00G (to LG). F. Ciesla's work was also supported by funds from the Carnegie Institution of Washington.

REFERENCES

Alexander, C.M.O'D. and Grossman, J.N. (2005) Alkali elemental and potassium isotopic compositions of Semarkona chondrules. *Meteoritics Planet. Sci.* **40**, 541-556.

Alexander, C.M.O'D. and Wang, J. (2001) Iron isotopes in chondrules: Implications for the role of evaporation during chondrule formation. *Meteoritics Planet. Sci.* **36**, 419-428.

Alexander, C.M.O'D., Grossman, J.N., Wang, J., Zanda, B., Bourot-Denise, M. and Hewins, R.H. (2000) The lack of potassium-isotopic fractionation in Bishunpur chondrules. *Meteoritics Planet. Sci.* **35**, 859-868.

Alexander, C.M.O'D., Grossman, J.N., Ebel, D.S. and Ciesla, F.J. (2008) The formation conditions of chondrules and chondrites. *Science* **320**, 1617-1619.

Bizzarro, M., Baker, J.A. and Haack, H. (2004) Mg isotope evidence for contemporaneous formation of chondrules and refractory inclusions. *Nature* **431**, 275-278.

Chase, M.W. Jr. (1998) NIST-JANAF Thermochemical Tables. Fourth Edition. *J. Phys. Chem Ref. Data, Monograph 9*. American Institute of Physics, Woodbury, New York.

Ciesla, F.J. (2005) Chondrule-forming processes-an overview. In *Chondrites and the Protoplanetary Disk* (eds. A.N. Krot, E.R.D. Scott and B. Reipurth), *ASP Conference Series 341*, pp. 811-820. Astronomical Society of the Pacific, San Francisco, CA.

Ciesla, F.J. (2006) Chondrule collisions in shock waves. *Meteoritics Planet. Sci.* **41**, 1347-1359.

Ciesla, F.J. and Cuzzi, J.N. (2006) The evolution of the water distribution in a viscous protoplanetary disc. *Icarus* **181**, 178-204.

Ciesla, F.J. and Hood, L.L. (2002) The nebular shock wave model for chondrule formation: Shock processing in a particle-gas suspension. *Icarus* **158**, 281-293.

Ciesla, F.J., Lauretta, D.S., Cohen, B.A. and Hood, L.L. (2003) A nebular origin for fine-grained phyllosilicates. *Science* **299**, 549-552.

Clayton, R.N., Onuma, N., Ikeda, Y., Mayeda, T.K., Hutcheon, I.D., Olsen, E.J. and Molini-Velsko, C. (1983) Oxygen isotopic compositions of chondrules in Allende and ordinary chondrites. In *Chondrules and their Origins* (ed. E.A. King), pp. 37-43. Lunar and Planetary Institute.

Cuzzi, J.N. and Alexander, C.M.O'D. (2006) Chondrule formation in particle-rich nebular regions at least hundreds of kilometres across. *Nature* **441**, 483-485.

Cuzzi, J.N. and Weidenschilling, S.J. (2006) Particle-gas dynamics and primary accretion. In *Meteorites and the Early Solar System II* (eds. D.S. Lauretta and H.Y. McSween), pp. 353-381. The University of Arizona Press, Tucson, AZ.

Cuzzi, J.N., Hogan, R.C., Paque, J.M. and Dobrovolskis, A.R. (2001) Size-selective concentration of chondrules and other small particles in protoplanetary nebula turbulence. *Astrophys. J.* **546**, 496-508.

Dauphas, N. and Rouxel, O. (2005) Mass spectrometry and natural variations of iron isotopes. *Mass Spectrom. Revs.* **25**, 515-550.

Dauphas, N., Janney, P.E., Mendybaev, R.A., Wadhwa, M., Richter, F.M., Davis, A.M., van Zuilen, M., Hines, R. and Foley, C.N. (2004) Chromatographic separation and multicollection-ICPMS analysis of iron. Investigating mass-dependent and -independent isotope effects. *Anal. Chem.* **76**, 5855-5863.

Desch, S.J. and Connolly, H.C. Jr. (2002) A model of the thermal processing of particles in solar nebula shocks: Application to the cooling rates of chondrules. *Meteoritics Planet. Sci.* **37**, 183-207.

Desch, S.J., Ciesla, F.J., Hood, L.L. and Nakamoto, T. (2005) Heating of chondritic materials in solar nebula shocks. In *Chondrites and the Protoplanetary Disk* (eds. A.N. Krot, E.R.D. Scott and B. Reipurth), *ASP Conference Series 341*, pp. 849-872. Astronomical Society of the Pacific, San Francisco, CA.

Everman, R.L.A. and Cooper, R.F. (2003) Internal reduction of an iron-doped magnesium aluminosilicate melt. *J. Am. Ceram. Soc.* **86**, 487-494.

Fedkin, A.V. and Grossman, L. (2006) The fayalite content of chondritic olivine: Obstacle to understanding the condensation of rocky material. In *Meteorites and the Early Solar System II* (eds. D.S. Lauretta and H.Y. McSween Jr.), pp. 279-294. Univ. AZ Press, Tucson, AZ.

Fedkin, A.V., Grossman, L. and Ghiorso, M.S. (2006) Vapor pressures and evaporation coefficients for melts of ferromagnesian chondrule-like compositions. *Geochim. Cosmochim. Acta* **70**, 206-223.

Fedkin, A.V., Ciesla, F.J. and Grossman, L. (2008) Shock wave models: Dependence of thermal history and Type II chondrule composition on water and dust enrichment. *Lunar Planet. Sci.* **XXXIX**, Abstract #1834 (CD-ROM).

Galy, A., Young, E.D., Ash, R.D. and O'Nions, R.K. (2000) The formation of chondrules at high gas pressures in the solar nebula. *Science* **290**, 1751-1753.

Galy, A., Yoffe, O., Janney, P.E., Williams, R.W., Cloquet, C., Alard, O., Halicz, L., Wadhwa, M., Hutcheon, I.D., Ramon, E. and Carignan, J. (2003) Magnesium isotope heterogeneity of the isotopic standard SRM980 and new reference materials for magnesium-isotope-ratio measurements. *J. Anal. At. Spectrom.* **18**, 1352-1356.

Ghiorso, M.S. and Sack, R.O. (1995) Chemical mass transfer in magmatic processes IV. A revised and internally consistent thermodynamic model for the interpolation and extrapolation of liquid-solid equilibria in magmatic systems at elevated temperatures and pressures. *Contrib. Mineral. Petrol.* **119**, 197-212.

Grossman, J.N. and Wasson, J.T. (1985) The origin and history of the metal and sulfide components of chondrules. *Geochim. Cosmochim. Acta* **49**, 925-939.

Grossman, L., Ebel, D.S., Simon, S.B., Davis, A.M., Richter, F.M. and Parsad, N.M. (2000) Major element chemical and isotopic compositions of refractory inclusions in C3 chondrites: The separate roles of condensation and evaporation. *Geochim. Cosmochim. Acta* **64**, 2879-2894.

Grossman, L., Beckett, J.R., Fedkin, A.V., Simon, S.B. and Ciesla, F.J. (2008) Redox conditions in the solar nebula: Observational, experimental and theoretical constraints. In *Oxygen in the Solar System* (eds. G.J. MacPherson, D.W. Mittlefehldt, J.H. Jones and S.B. Simon), *Revs. Mineral. Geochem* **68**, pp. 93-140. Mineralogical Society of America, Chantilly, VA.

Hashimoto, A. (1983) Evaporation metamorphism in the early solar nebula-evaporation experiments on the melt FeO-MgO-SiO₂-CaO-Al₂O₃ and chemical fractionations in primitive materials. *Geochem J.* **17**, 111-145.

Hewins, R.H. and Connolly, H.C. Jr. (1996) Peak temperatures of flash-melted chondrules. In *Chondrites and the Protoplanetary Disk* (eds. R.H. Hewins, R.H. Jones and E.R.D. Scott), pp. 197-204. Cambridge University Press, New York.

Hewins, R.H., Connolly, H.C. Jr., Lofgren, G.E. and Libourel, G. (2005) Experimental constraints on chondrule formation. In *Chondrites and the Protoplanetary Disk* (eds. A.N. Krot, E.R.D. Scott and B. Reipurth), *ASP Conference Series 341*, pp. 286-316. Astronomical Society of the Pacific, San Francisco, CA.

Hood, L.L. and Horanyi, M. (1991) Gas dynamic heating of chondrule precursor grains in the solar nebula. *Icarus* **93**, 259-269.

Hood, L.L. and Horanyi, M. (1993) The nebular shock wave model for chondrule formation – One-dimensional calculations. *Icarus* **106**, 179-189.

Humayun, M. and Clayton, R.N. (1995) Potassium isotope cosmochemistry: Genetic implications of volatile element fractionation. *Geochim. Cosmochim. Acta* **59**, 2131-2148.

Iida, A., Nakamoto, T., Susa, H. and Nakagawa, Y. (2001) A shock heating model for chondrule formation in a protoplanetary disk. *Icarus* **153**, 430-450.

- Jones, R.H. (1990) Petrology and mineralogy of Type II, FeO-rich chondrules in Semarkona (LL3.0): Origin by closed-system fractional crystallization, with evidence for supercooling. *Geochim. Cosmochim. Acta* **54**, 1785-1802.
- Jones, R.H. (1994) Petrology of FeO-poor, porphyritic pyroxene chondrules in the Semarkona chondrite. *Geochim. Cosmochim. Acta* **58**, 5325-5340.
- Jones, R.H. (1996) FeO-rich, porphyritic pyroxene chondrules in unequilibrated ordinary chondrites. *Geochim. Cosmochim. Acta* **60**, 3115-3138.
- Jones, R.H. and Scott, E.R.D. (1989) Petrology and thermal history of Type IA chondrules in the Semarkona (LL3.0) chondrite. In *Proc. 19th Lunar Planet. Sci. Conf.*, pp. 523-536. Lunar and Planetary Institute, Houston, TX.
- Kehm, K., Hauri, E.H., Alexander, C.M.O'D. and Carlson, R.W. (2003) High precision iron isotope measurements of meteoritic material by cold plasma ICP-MS. *Geochim. Cosmochim. Acta* **67**, 2879-2891.
- Morris, M.A., Desch, S.J. and Ciesla, F.J. (2007) The effect of line cooling in chondrule-forming shocks. *Meteoritics Planet. Sci.* **42** Supp., A111 (abstr.)
- Mullane, E., Russell, S.S. and Gounelle, M. (2005) Nebular and asteroidal modification of the iron isotope composition of chondritic components. *Earth Planet. Sci. Lett.* **239**, 203-218.
- Richter, F.M., Janney, P.E., Mendybaev, R.A., Davis, A.M., Wadhwa, M. (2007) Elemental and isotopic fractionation of Type B CAI-like liquids by evaporation. *Geochim. Cosmochim. Acta* **71**, 5544-5564.
- Roskosz, M., Luais, B., Watson, H.C., Toplis, M.J., Alexander, C.M.O'D. and Mysen, B. O. (2006) Experimental quantification of the fractionation of Fe isotopes during metal segregation from a silicate melt. *Earth Planet. Sci. Lett.* **248**, 851-867.
- Tachibana, S., Nagahara, H., Ozawa, K. and Yamada, M. (2007) Isotopic fractionation of iron during kinetic evaporation of metallic iron. *Meteoritics Planet. Sci.* **42** Supp., A146 (abstr.)
- Taylor, S., Alexander, C.M.O'D., Delaney, J., Ma, P., Herzog, G.F. and Engrand, C. (2005) Isotopic fractionation of iron, potassium, and oxygen in stony cosmic spherules: Implications for heating histories and sources. *Geochim. Cosmochim. Acta* **69**, 2647-2662.
- Theis, K.J., Burgess, R., Lyon, I.C. and Sears, D.W. (2008) The origin and history of ordinary chondrites: A study by iron isotope measurements of metal grains from ordinary chondrites. *Geochim. Cosmochim. Acta* **72**, 4440-4456.

Uesugi, M. and Sekiya, M. (2006) Separation of melted iron spheres in chondrules during the chondrule formation. *Lunar Planet. Sci.* **XXXVII**, Abstract #1505 (CD-ROM).

Uesugi, M., Sekiya, M. and Nakamura, T. (2008) Kinetic stability of a melted iron globule during chondrule formation. I. Non-rotating model. *Meteoritics Planet. Sci.* **43**, 717-730.

Wang, J., Davis, A.M., Clayton, R.N., Mayeda, T.K. and Hashimoto, A. (2001) Chemical and isotopic fractionation during the evaporation of the FeO-MgO-SiO₂-CaO-Al₂O₃-TiO₂ rare earth element melt system. *Geochim. Cosmochim. Acta* **65**, 479-494.

Weidenschilling, S.J. (1977) Aerodynamics of solid bodies in the solar nebula. *Monthly Not. Royal Astron. Soc.* **180**, 57-70.

Yu, Y., Hewins, R.H., Alexander, C.M.O.'D. and Wang, J. (2003) Experimental study of evaporation and isotopic mass fractionation of potassium in silicate melts. *Geochim. Cosmochim. Acta* **67**, 773-786.

Young, E.D., Ash, R.D., Galy, A. and Belshaw, N.S. (2002) Mg isotope heterogeneity in the Allende meteorite measured by UV laser ablation-MC-ICPMS and comparisons with O isotopes. *Geochim. Cosmochim. Acta* **66**, 683-698.

Zhu, X.K., Guo, Y., O'Nions, R.K., Young, E.D. and Ash, R.D. (2001) Isotopic homogeneity of iron in the early solar nebula. *Nature* **412**, 311-313.

FIGURE CAPTIONS

Figure 1. Olivine composition histograms for Type II PO chondrules in Semarkona. Bins are 0.5 mole% fayalite wide. For most chondrules, the mode tends to be at a lower fayalite content than the median. As a result, there is a steep increase in frequency from the lowest fayalite values to the peak and a much more gradual decline in frequency from the mode to higher fayalite values. Note the sporadic and rare occurrence of compositions to the low- X_{Fa} side of the continuous parts of the distributions, and the much more common occurrence of a long, discontinuous, low tail to high X_{Fa} . Analyses of olivine in chondrules with the highest mean X_{Fa} tend to be more normally distributed. One standard deviation uncertainties are shown for the mean values. n: number of analyses.

Figure 2. Magnesium isotopic compositions of individual chondrules from the Allende meteorite, as reported in the literature relative or renormalized to the DSM3 standard, which is indistinguishable from mean solar system matter. There are slightly

more chondrules with positive than negative $\delta^{25}\text{Mg}$, and the mean value is +0.15‰. No significant difference in $\delta^{25}\text{Mg}$ can be seen between porphyritic (PO) and barred (BO) olivine chondrules. Chondrules of other texture types are lumped together with those whose texture types are unknown. Which of the chondrules are Type I and which are Type II is unknown.

Figure 3. Silicon isotopic compositions of individual chondrules from the Allende meteorite. Data are those reported by Clayton *et al.* (1983) relative to SMOW but have been renormalized to mean solar system matter. All have $\delta^{29}\text{Si}$ within $\pm 0.4\%$ of mean solar system matter. Types I and II chondrules are indistinguishable. Unknown: neither the chemical nor the textural type are known.

Figure 4. Potassium isotopic compositions of chondrules from Allende (Humayun and Clayton, 1995), Bishunpur (Alexander *et al.*, 2000) and Semarkona (Alexander and Grossman, 2005). Plotted for Bishunpur and Semarkona is the mean for each chondrule, obtained by weighting the different ion microprobe spot analyses from each by the inverse square of their 1σ uncertainties. Type II chondrules, particularly the porphyritic ones, tend to have positive $\delta^{41}\text{K}$, while the Type Is are more evenly distributed about normal K. “Others” refers to other textural types.

Figure 5. Iron isotopic compositions of individual chondrules from carbonaceous (CC) and ordinary (OC) chondrites, as reported in the literature relative or renormalized to the IRMM-014 standard, which is indistinguishable from mean solar system matter. Almost all have $\delta^{56}\text{Fe}$ within $\pm 0.8\%$ of mean solar system matter. Little difference can be discerned between Type I and Type II chondrules, nor between porphyritic and barred ones. “Others” refers to other textural types.

Figure 6. Shock wave thermal histories computed at various combinations of shock velocity, initial P^{tot} , dust enrichment, water enrichment and chondrule radius, r . The effect of varying dust enrichment is shown for water enrichment of 640x, an initial P^{tot} of 1.5×10^{-6} bar and $r=0.5$ mm at a shock velocity of (a) 6 km/s and (b) 7 km/s; (c) of varying shock velocity for dust enrichment of 300x, water enrichment of 640x and $r=0.5$ mm at an initial P^{tot} of 1.5×10^{-5} bar; (d) of varying chondrule radius for dust enrichment of 600x, water enrichment of 550x, an initial P^{tot} of 1.5×10^{-6} bar and shock velocity of 6

km/s; of varying initial P^{tot} (e) at 300x dust enrichment, 640x water enrichment, $r=0.5$ mm and a shock velocity of 3 km/s; and of varying water enrichment (f) at 600x dust enrichment, an initial P^{tot} of 1.5×10^{-6} bar, $r=0.5$ mm and a shock velocity of 6 km/s. In all panels, time-zero is defined as the time when the temperature is 1400K. Linear portions of the thermal histories are labeled with their heating or cooling rates in K/min. In (c), the following inflection points characteristic of all thermal histories discussed herein are defined on the curve for 3.5 km/sec: X-the pre-shock temperature; Y-the peak temperature; and Z-the post-shock base of the temperature spike. Portions of each thermal history over which the silicate fraction of the corresponding protochondrule is <50 wt%, >50 wt% and 100% molten are solid, dashed and dotted, respectively. Thermal histories coded with dash-dot patterns are those that could not be modeled chemically because the protochondrules lost all their FeO. In this case, the dash-dot pattern begins after total FeO loss unless this occurred before 50% of the silicate melted.

Figure 7. Evolution of the ambient total pressure, P^{tot} , for the shock wave thermal histories shown in Fig. 6. In all panels, time-zero is defined as the time when the temperature is 1400K, as in Fig. 6. All other things being equal, the post-shock P^{tot} increases with increasing dust enrichment (a b), increasing shock velocity (c.), increasing initial P^{tot} (e) and increasing water enrichment (f).

Figure 8. Percent of each of Na, K, Fe, Ni, Si and Mg calculated to evaporate from a reduced 0.5 mm-radius chondrule precursor, plotted as a function of time when a 6 km/sec shock wave traverses a region of the solar nebula initially at $P^{tot} = 1.5 \times 10^{-6}$ bar and enriched in water and dust by factors of 550 and 600, respectively, relative to a system of solar composition. These conditions, together with the assumptions made in the text, collectively define the “standard case” in this work. Droplet temperatures corresponding to various times are indicated at the top of the graph. The peak temperature is reached when the shock arrives, 234 minutes after the droplet reaches 1400K.

Figure 9. Redox equilibration of the droplet and gas for the standard case. The log of the equilibrium f_{O_2} of the droplet (solid curve) and of the ambient gas (dashed curve) are each plotted as a function of time relative to the logarithm of the f_{O_2} of the

iron-wüstite (IW) buffer. Droplet temperatures corresponding to various times are indicated at the top of the graph.

Figure 10 (a) and (b). Bulk chemical composition of the model droplet for the standard case, plotted as a function of time. The major effects seen are due to oxidation, evaporation and mechanical separation of metallic Fe; and evaporation and recondensation of alkalis. Droplet temperatures corresponding to various times are indicated at the top of the graph.

Figure 11. Snapshots of the mineral proportions in the model droplet in the standard case at (a) 1400K, the starting temperature of chemical modeling; (b) 1580K, the pre-shock base of the temperature spike; (c) 1832K, the peak temperature; (d) 1625K, the post-shock base of the temperature spike, where crystal fractionation is assumed to begin and below which all remaining relict grains are assumed to be preserved; (e) 1590K, where fractional crystallization of olivine reaches 70%; and (f) 973K, the final temperature of chemical modeling. Proportions of each of the initial silicate and oxide phases assumed to be preserved are indicated in black. Proportions of the olivine and spinel that are chemically sequestered from the liquid during cooling are indicated by shading as “fractionated”.

Figure 12 (a) and (b). Bulk chemical composition of silicate liquid in the model droplet in the standard case, plotted as a function of time. During the first 200 minutes, the liquid evolution is governed by melting of feldspar and clinopyroxene, a faster rate of evaporation of the alkalis than the rate at which they are added by melting, and formation of clinopyroxene by reaction of olivine with the liquid. At the time of shock arrival, orthopyroxene and olivine dissolve and, at later times, olivine subtraction and recondensation of alkalis control the liquid composition. Droplet temperatures corresponding to various times are indicated at the top of the graph.

Figure 13. Olivine composition histogram produced in the model droplet in the standard case. The histogram is composed of olivine compositions preserved by fractional crystallization plus a relatively small number of grains of the starting material that remained inert throughout the thermal history. The histogram has many features in common with those of Fig. 1, particularly chondrule 5. Bins are 0.005 wide.

Figure 14. The change in $\delta^{25}\text{Mg}$ for the droplet in the standard case, plotted as a function of time. The inset shows the simultaneous evolution of $\delta^{25}\text{Mg}$ of the coexisting gas. Droplet temperatures corresponding to various times are indicated at the top of the graph. The Mg isotopic composition of the final product is essentially normal. Abbreviations: sequ. fr.-sequestered fraction; equ. fr.-equilibrated fraction; bulk-bulk droplet.

Figure 15. The change in $\delta^{29}\text{Si}$ of the droplet in the standard case, plotted as a function of time. The inset shows the simultaneous evolution of $\delta^{29}\text{Si}$ of the coexisting gas. Droplet temperatures corresponding to various times are indicated at the top of the graph. The Si isotopic composition of the final product is essentially normal. Abbreviations as in Fig. 14.

Figure 16. The change in $\delta^{41}\text{K}$ for the droplet in the standard case, plotted as a function of time. Droplet temperatures corresponding to various times are indicated at the top of the graph. After all relict feldspar dissolves in the liquid at 150 minutes, there is no K in the sequestered fraction. Had it been possible to continue the model run to lower temperature, the K isotopic composition of the product would have been normal. Abbreviations as in Fig. 14.

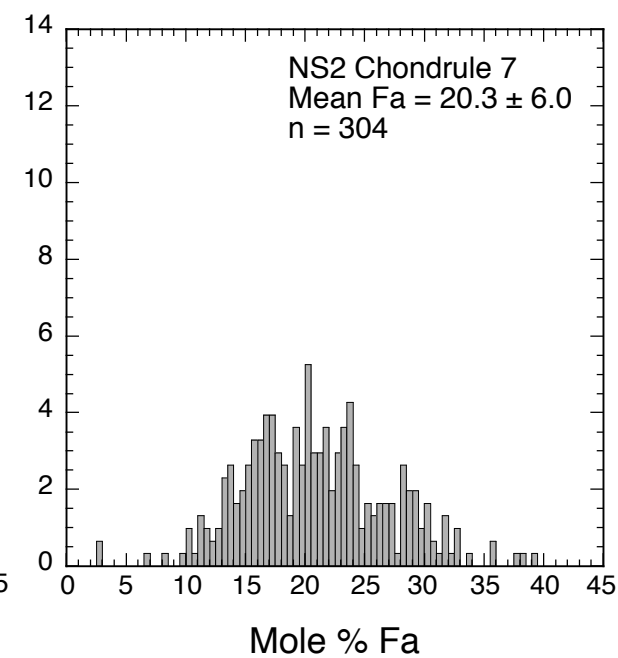
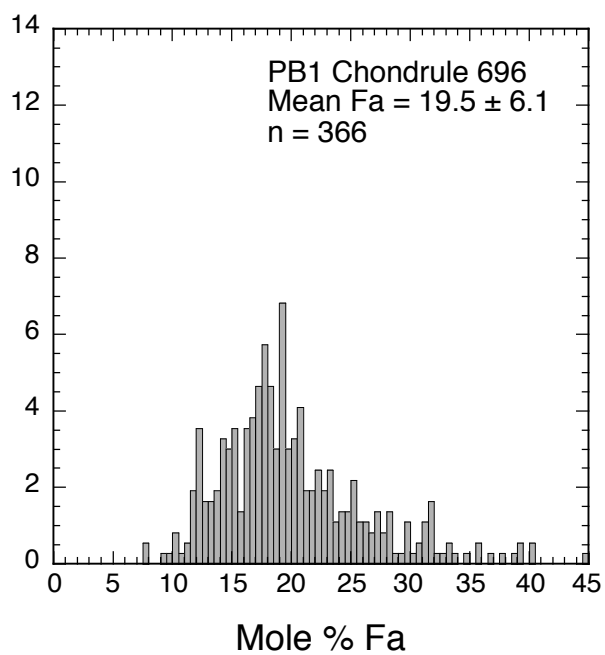
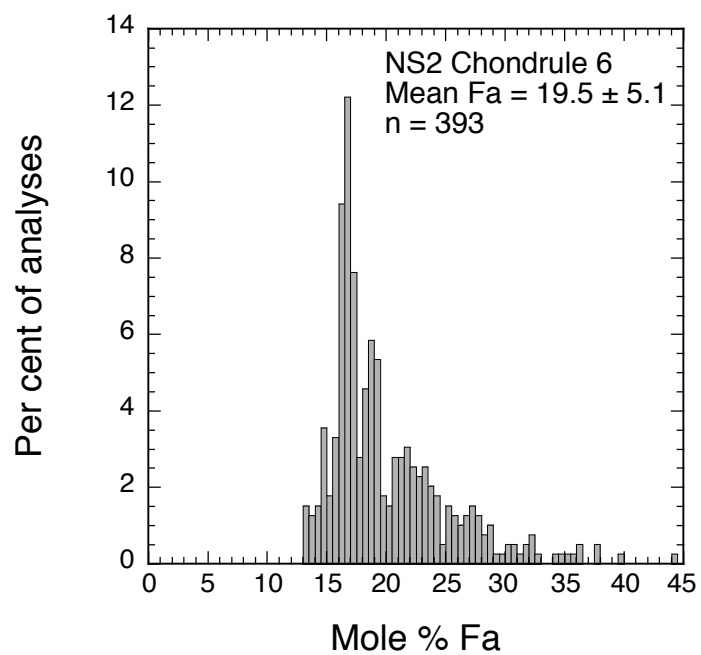
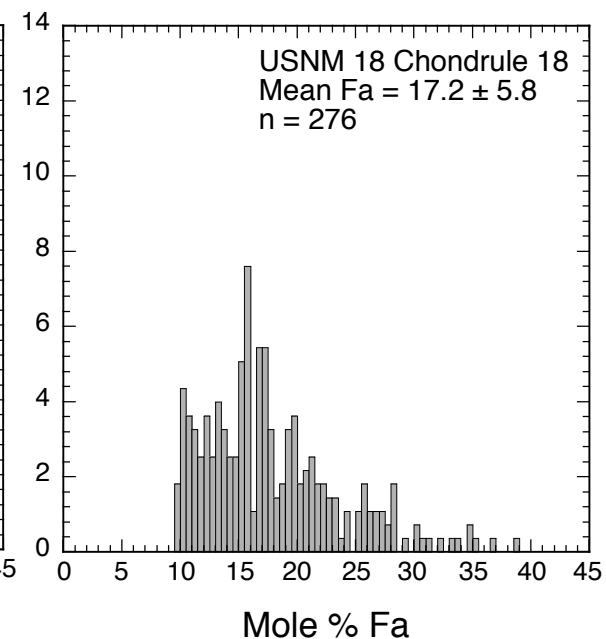
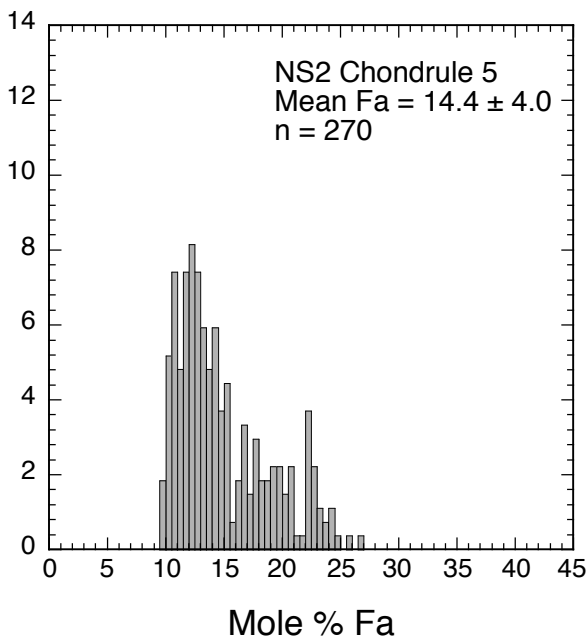
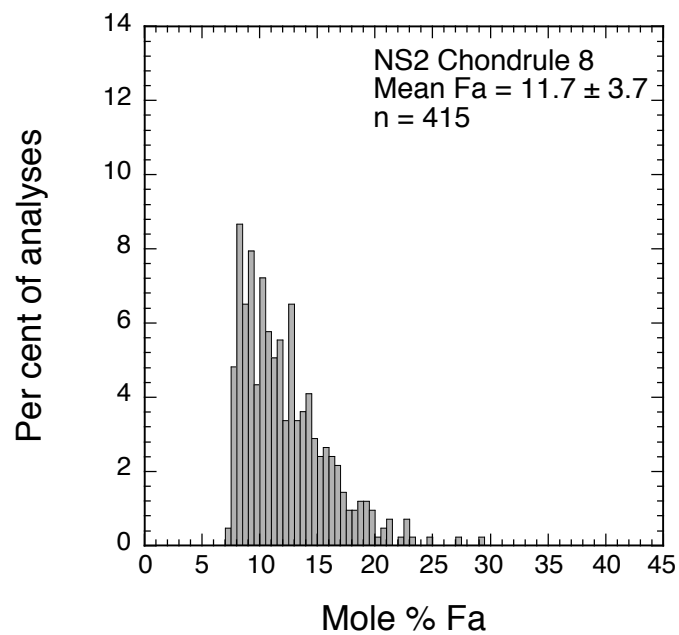
Figure 17. The change in $\delta^{56}\text{Fe}$ for the droplet in the standard case during the time interval around the time of shock arrival. Droplet temperatures corresponding to various times are indicated at the top of the graph. The time history for the complete model run is shown in the inset. Fractional crystallization of olivine occurs during cooling from 1620 to 1530K, while $\delta^{56}\text{Fe}$ of the silicate liquid, part of the equilibrating fraction of the droplet, is still elevated. Due to partial recondensation of iron onto metal that is external to the droplet, $\delta^{56}\text{Fe}$ of the bulk droplet is 0.29‰ at the end of the model run (973K). Ext. metal: external metal; other abbreviations as in Fig. 14.

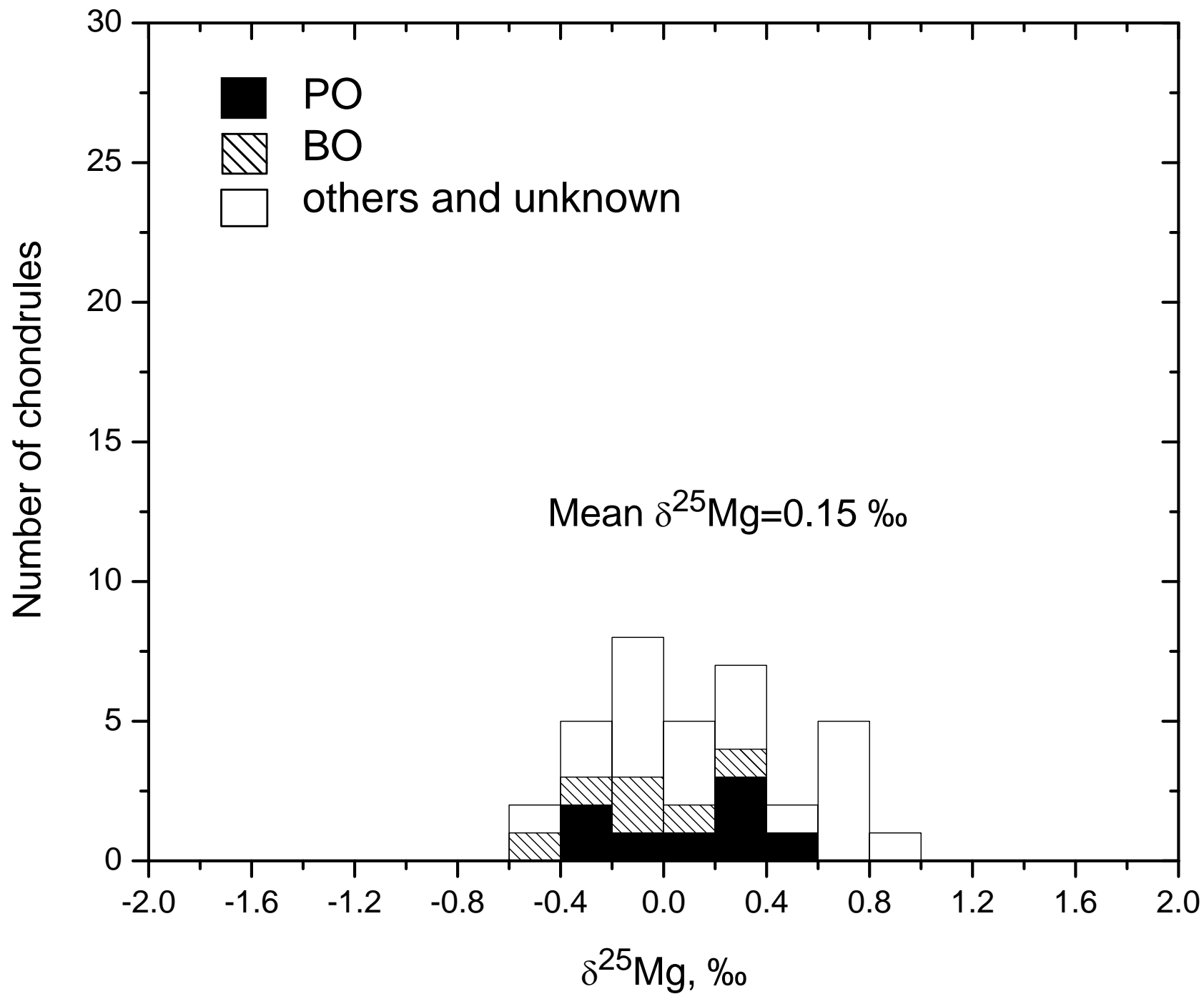
Figure 18. Proportion of the total olivine in the model droplet, plotted as a function of its $\delta^{56}\text{Fe}$ for the standard case. The bulk droplet has $\delta^{56}\text{Fe}$ of 0.29‰.

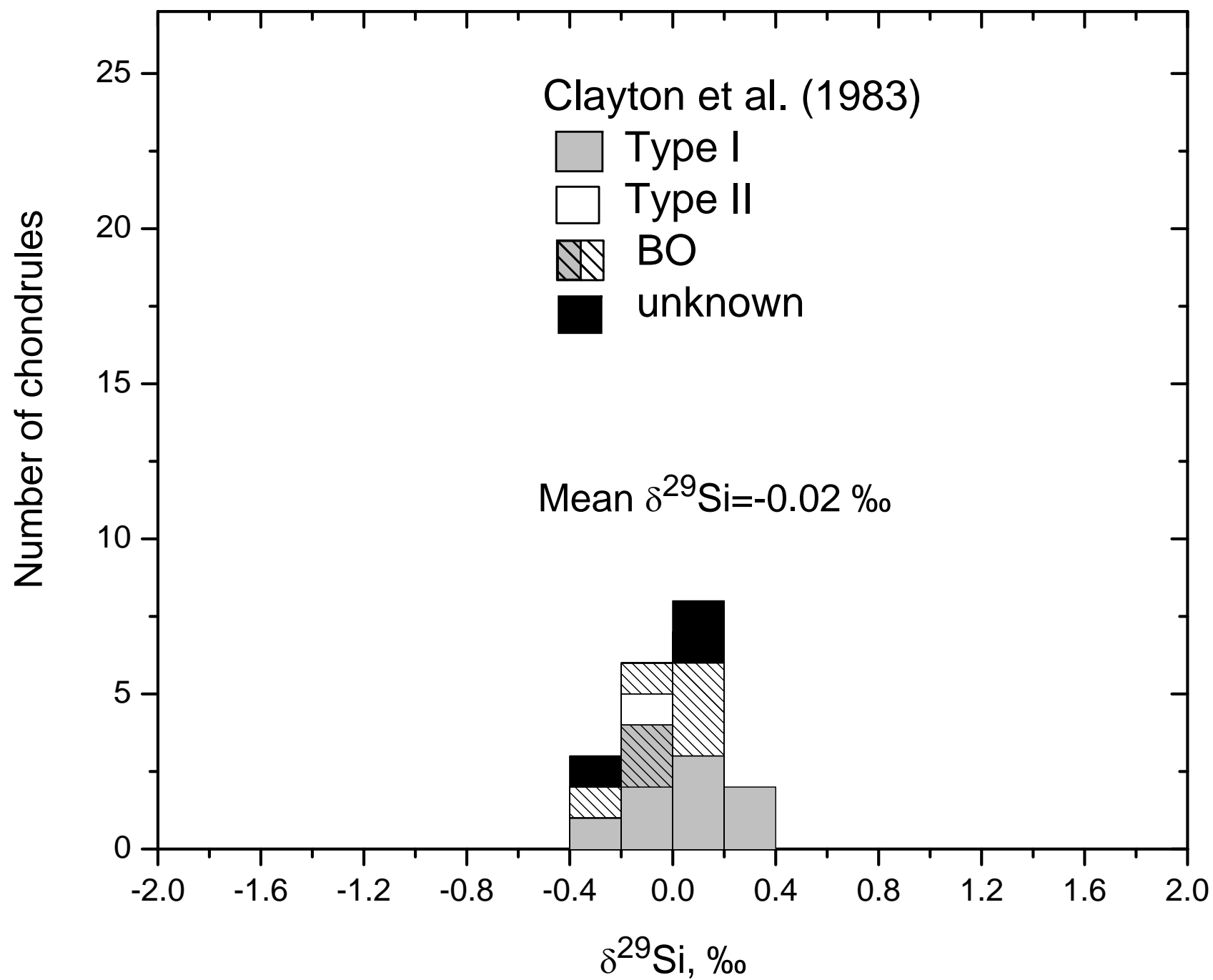
Figure 19. Olivine composition histograms calculated when each of the indicated parameters is adjusted to the value shown instead of its value in the standard case. Most calculated histograms are like that of the standard case in Fig. 13. Two, (g) and (h), are more gaussian. In two, (b) and (l), except for relict grains, the minimum X_{Fa} is very close

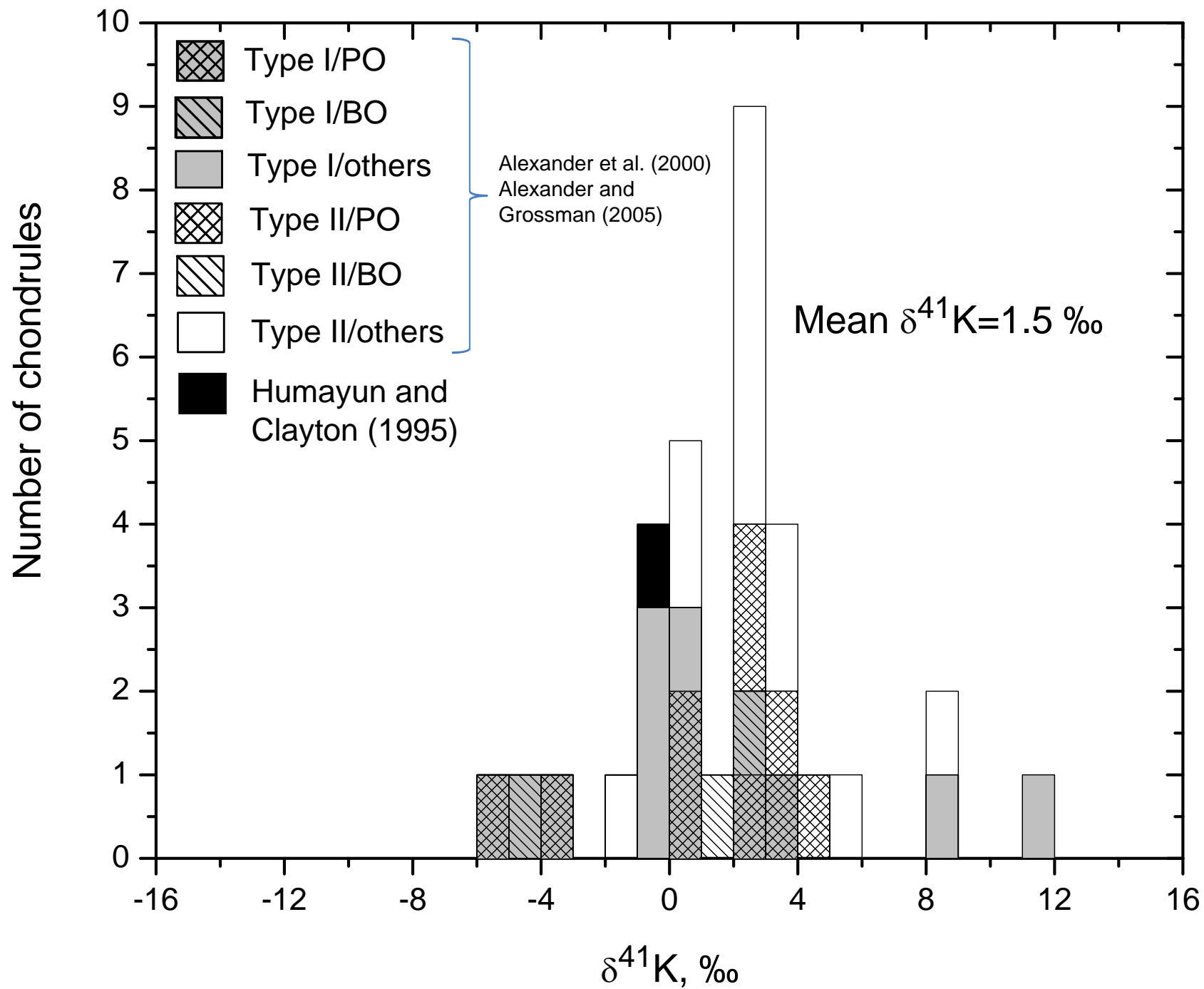
to that of the mode. All three types of histograms have counterparts in those of Type II PO chondrules in Fig. 1. Bins are 0.005 wide.

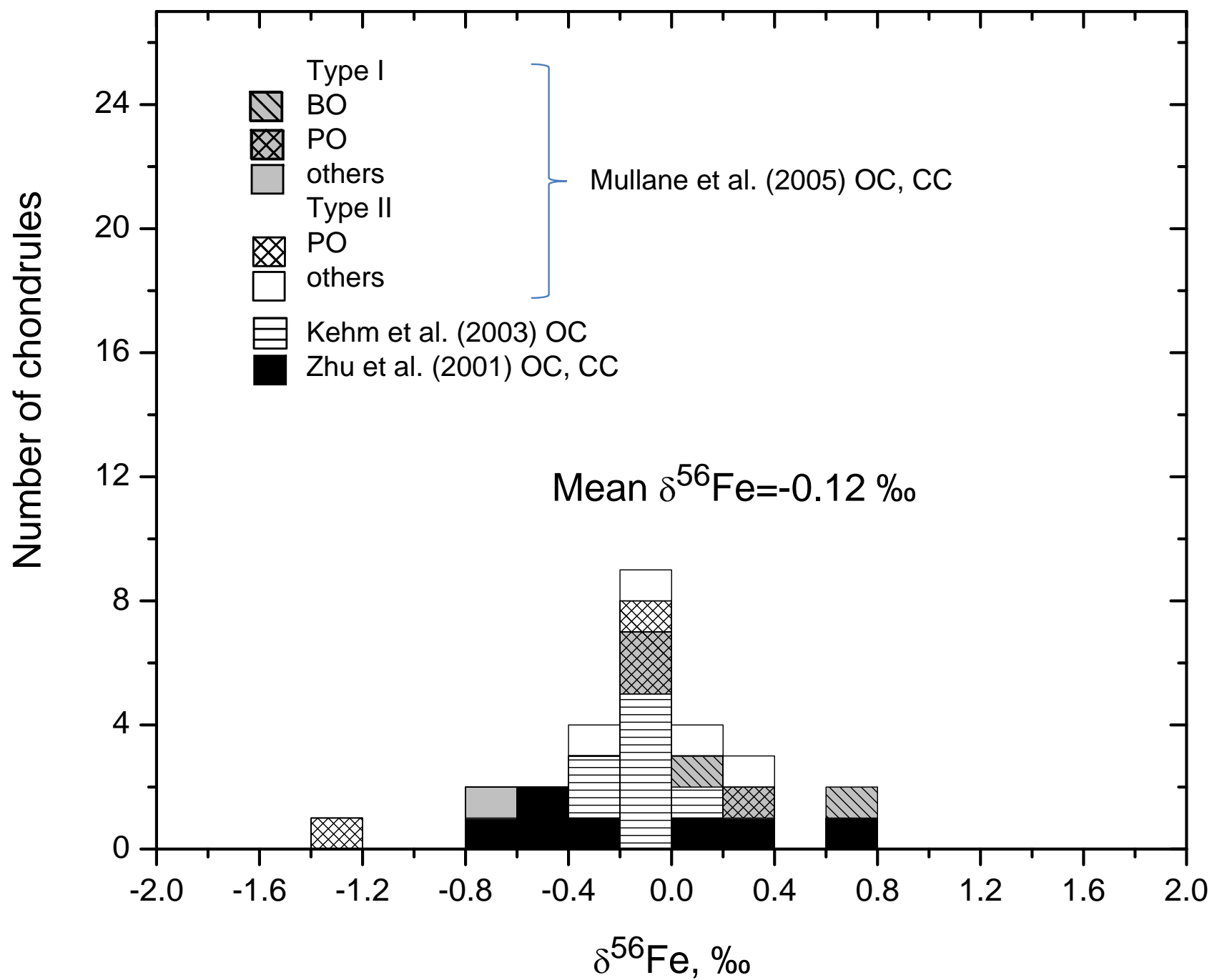
Figure 20. The degree of evaporation of K plotted against the FeO content of the liquid in the final steps of each of the model runs shown in Fig. 19. As K recondenses into silicate liquid, the FeO content of the latter varies due to fractional crystallization of olivine and oxidation-reduction reactions. The range of FeO contents in mesostases of Type II PO chondrules is shown as the shaded region. For Type II chondrules, gas-chondrule interaction must continue until K recondensation is complete. This probably requires persistence of metastable liquid, allowing its FeO content to evolve as shown.

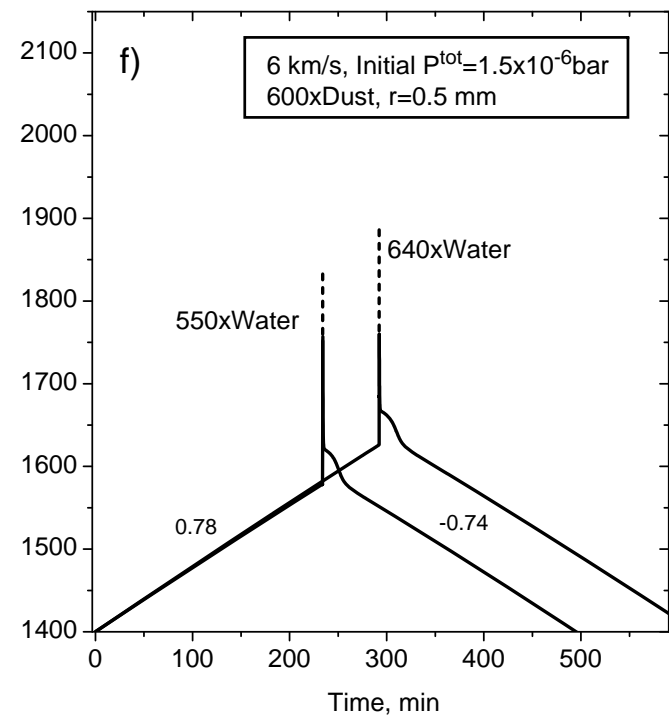
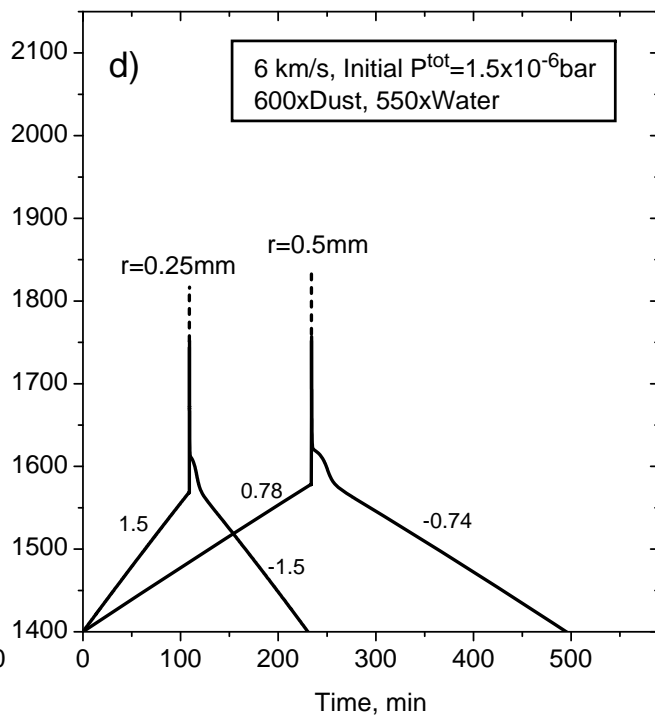
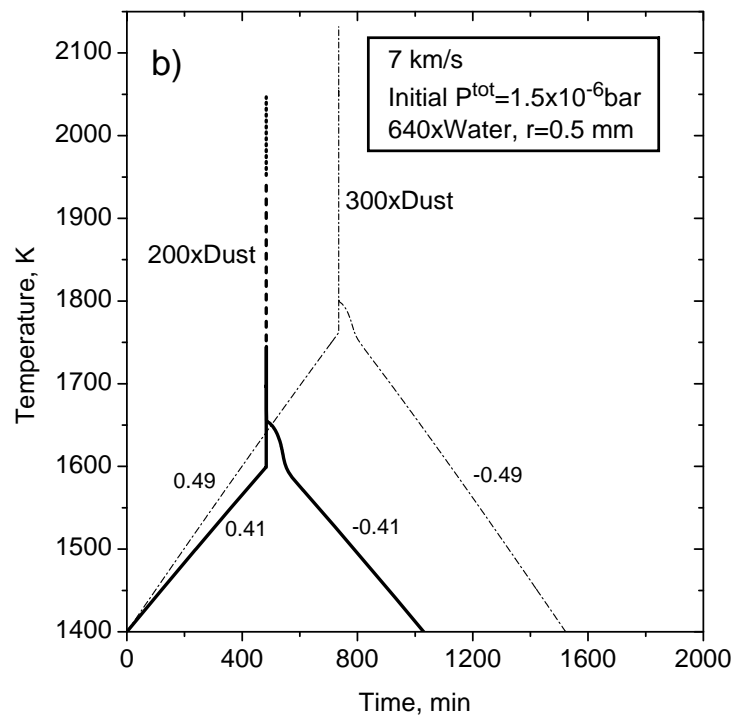
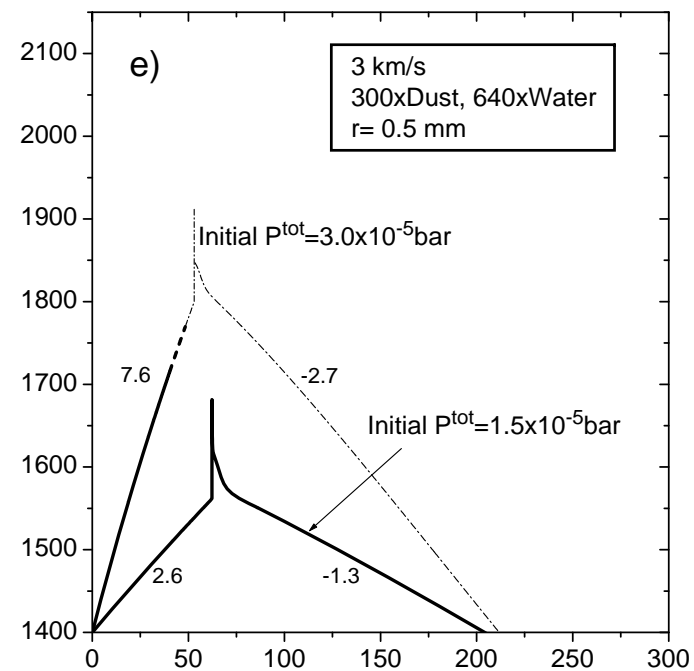
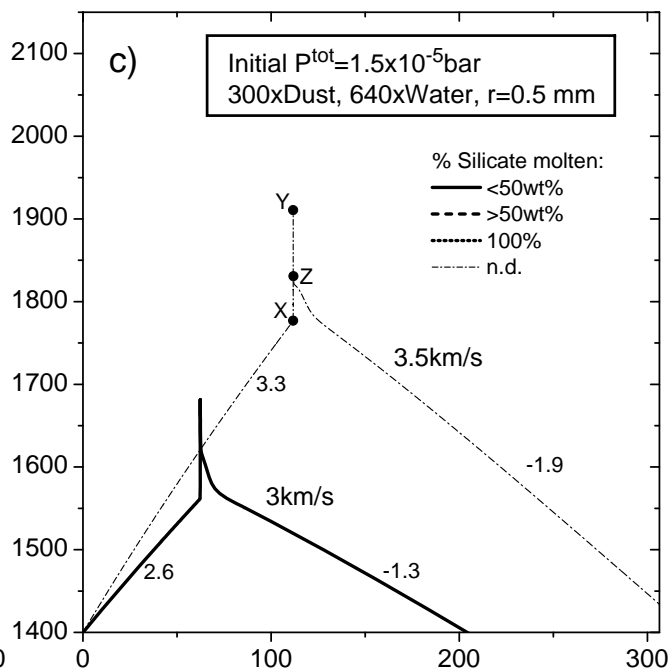
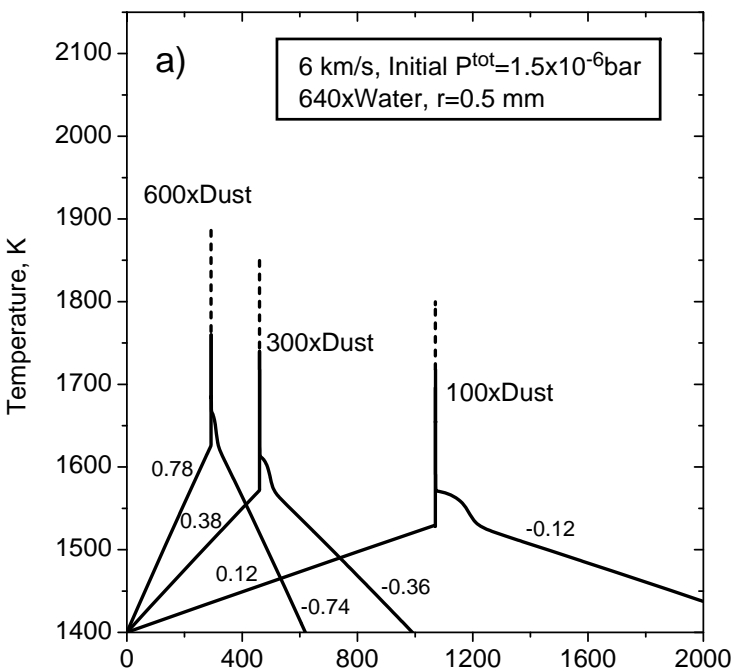


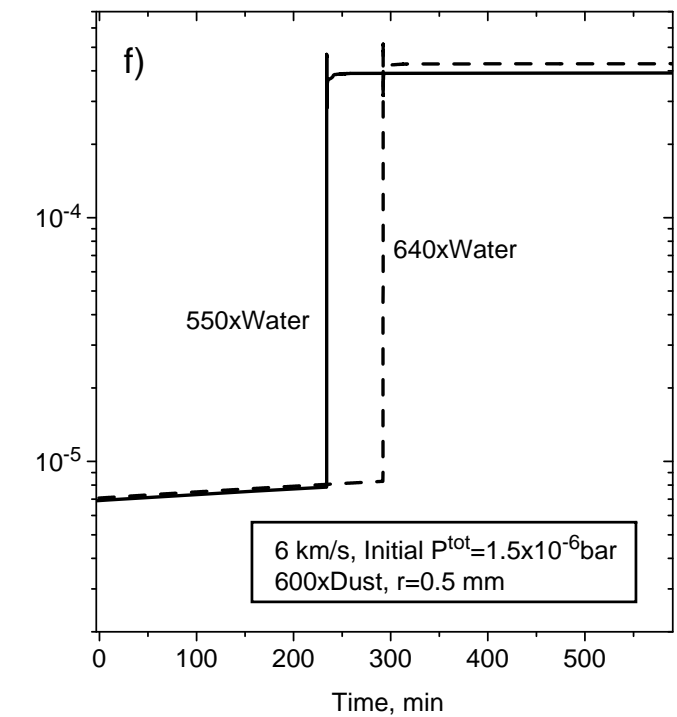
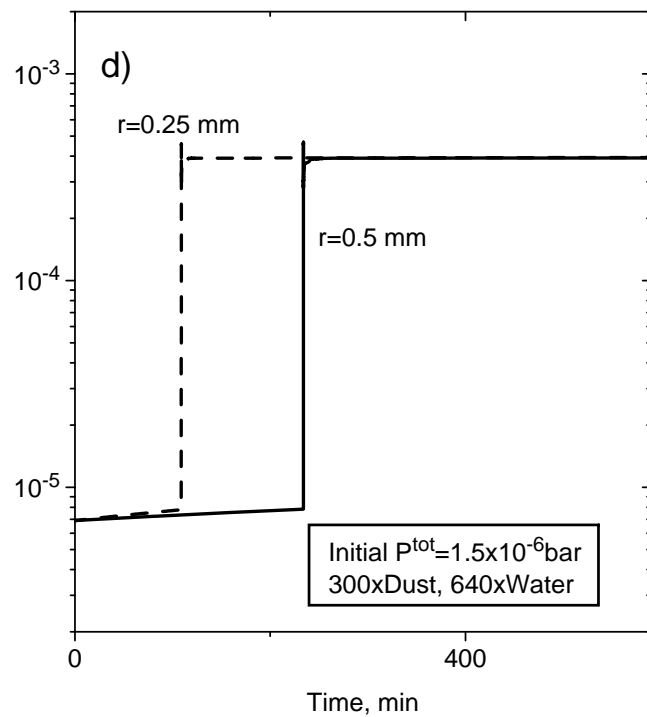
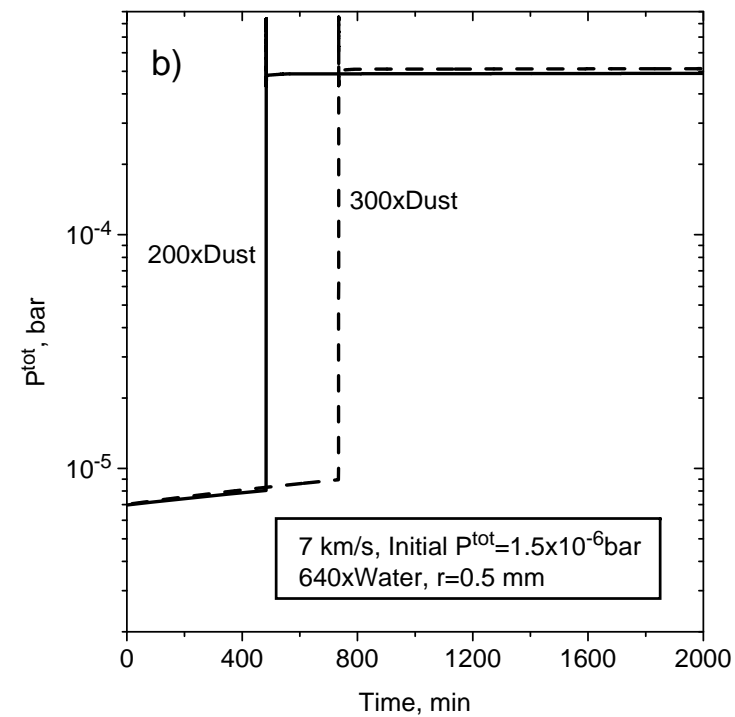
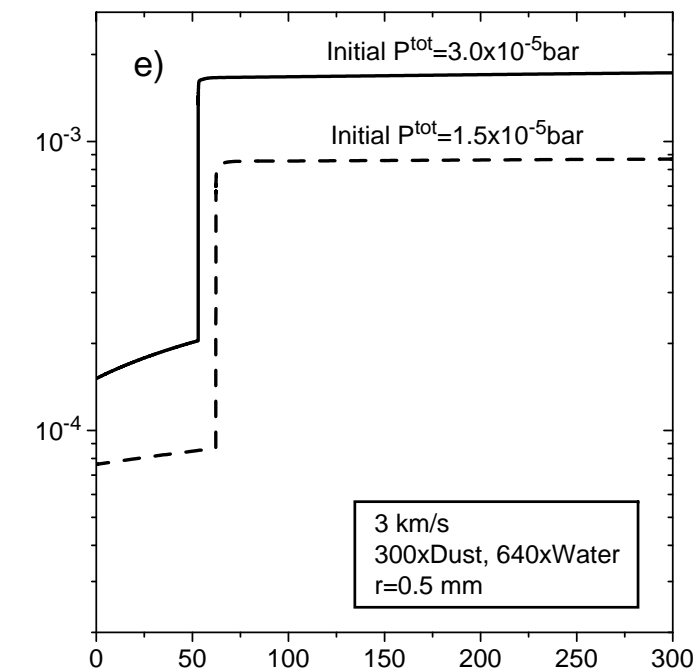
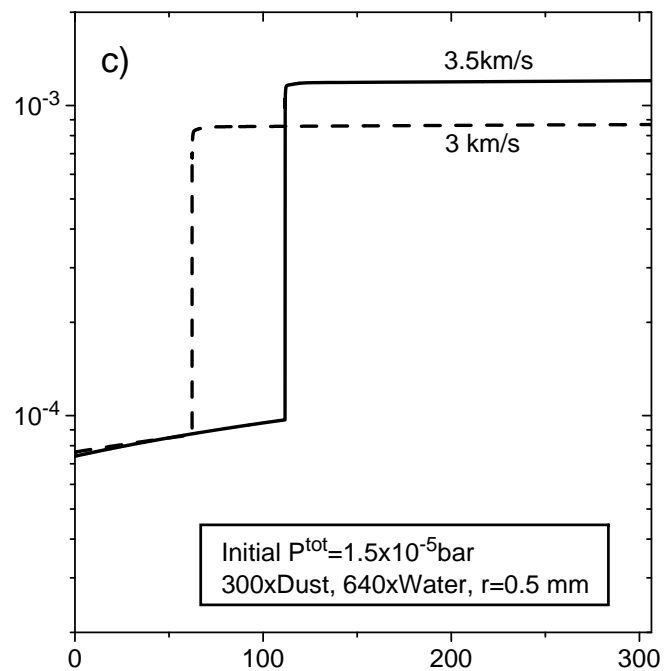
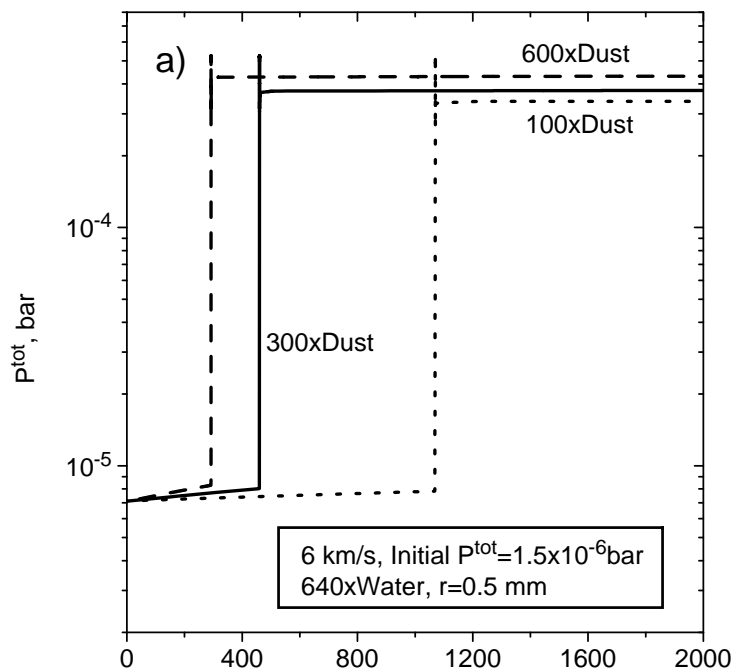


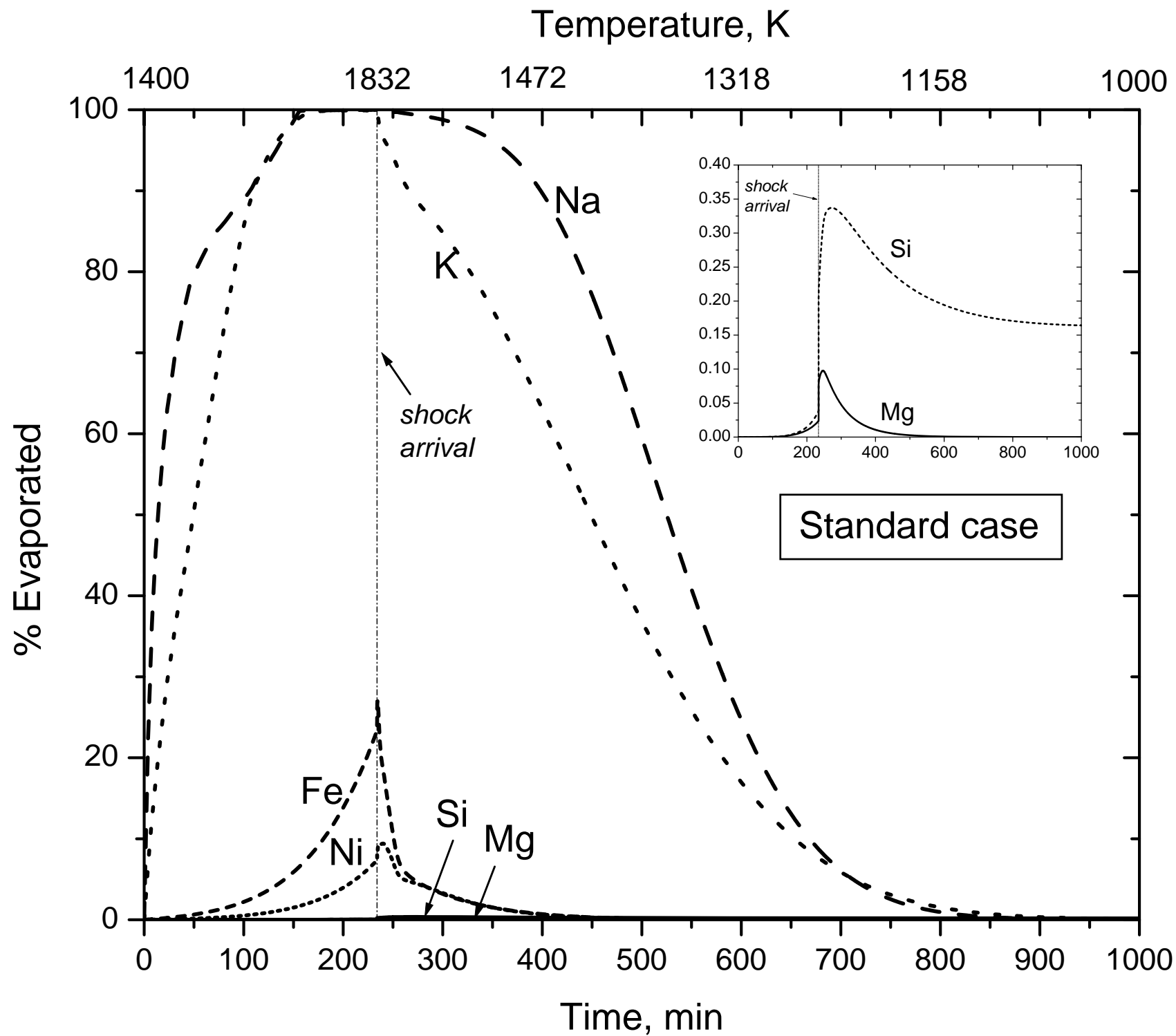


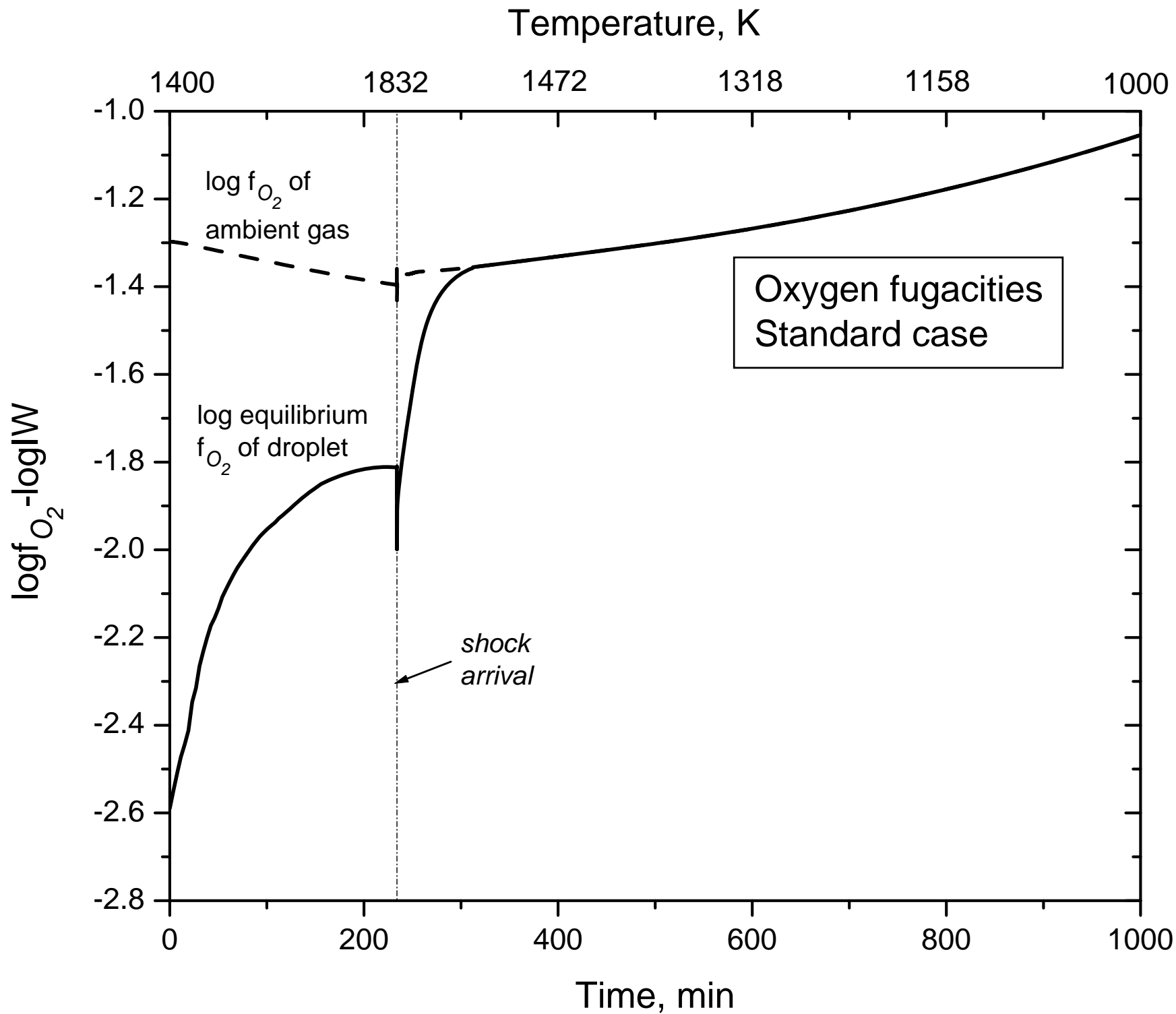


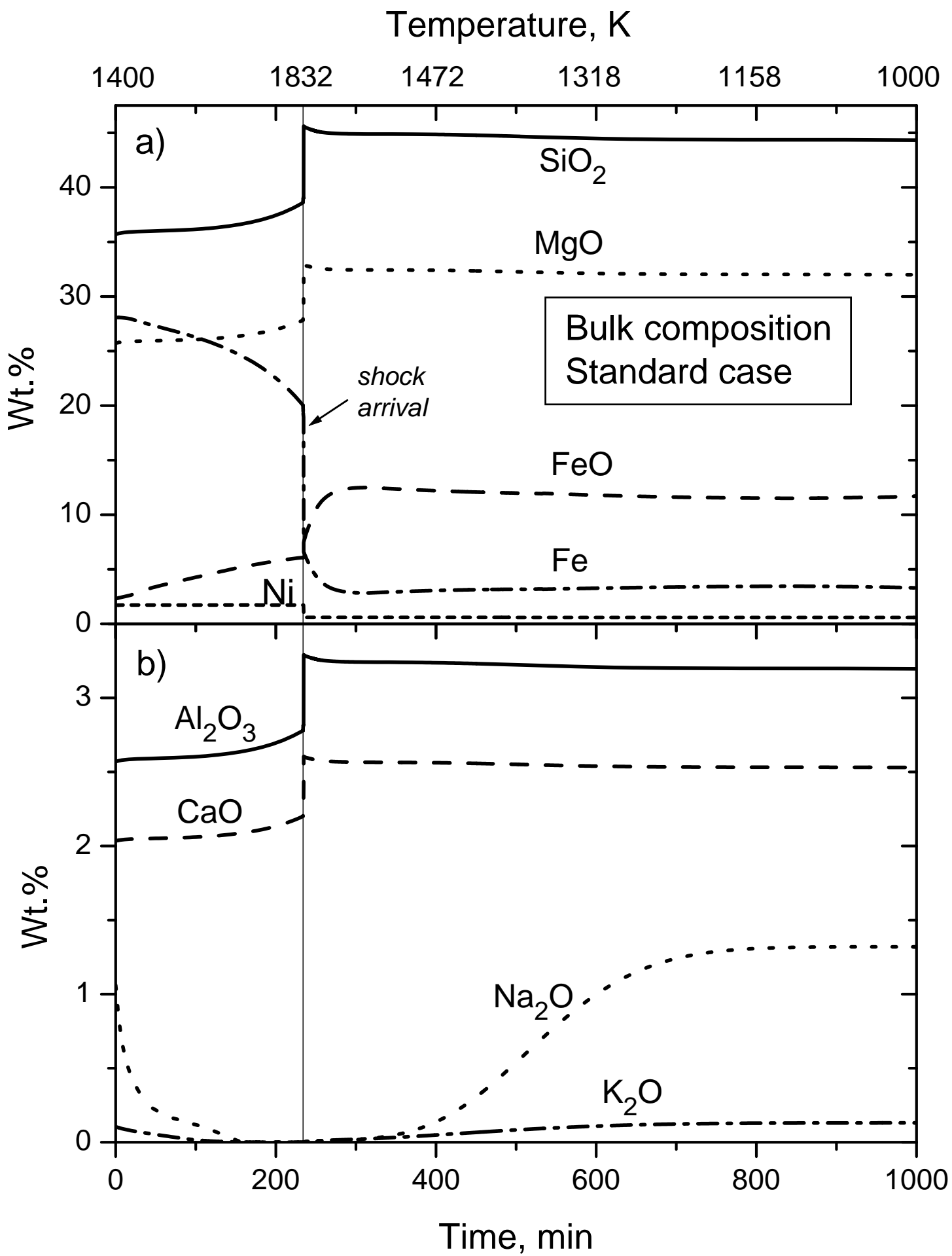


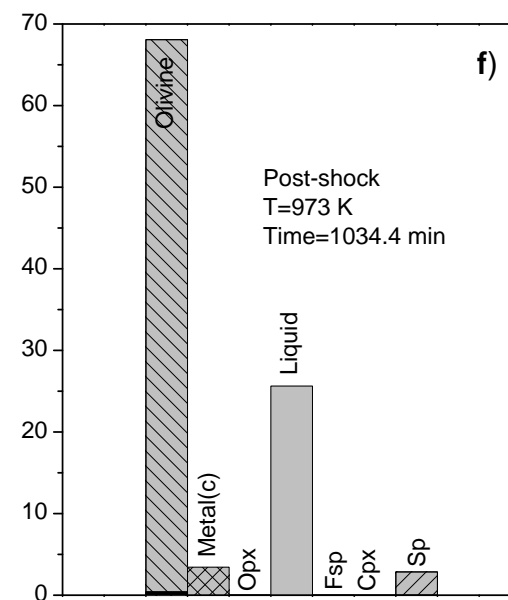
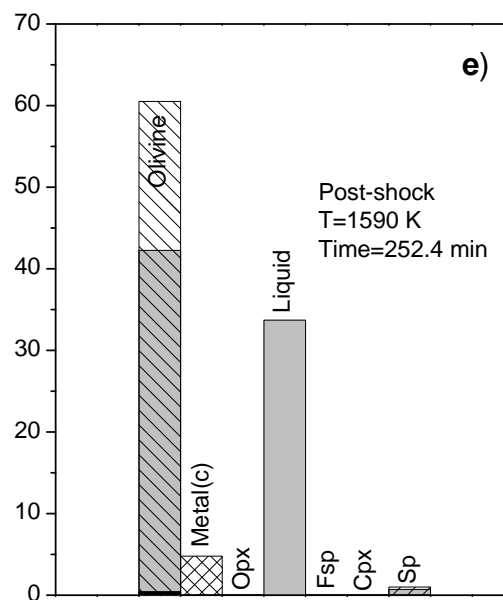
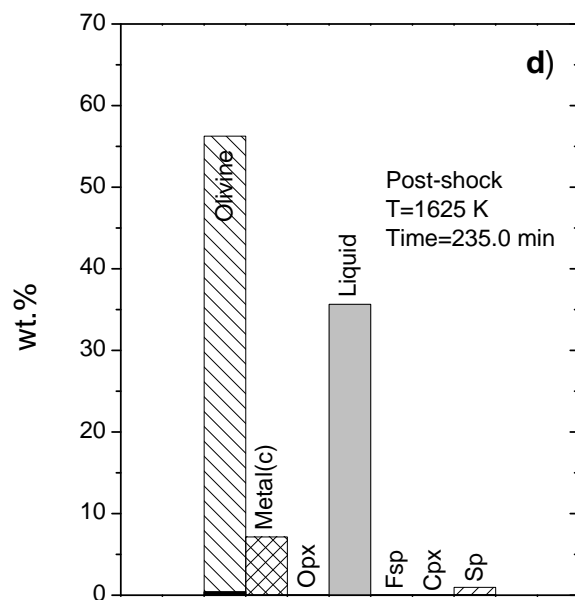
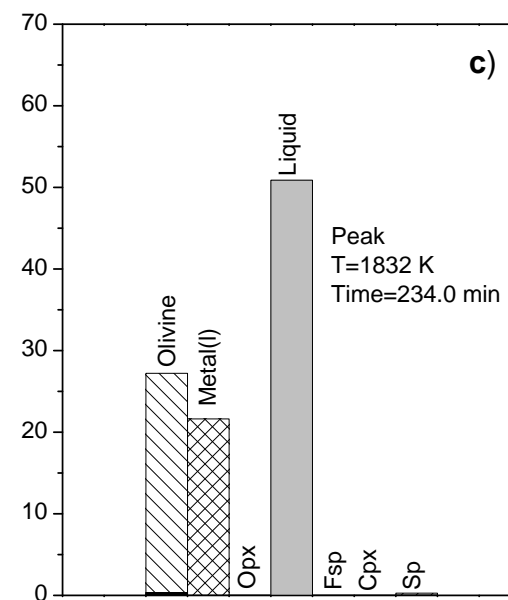
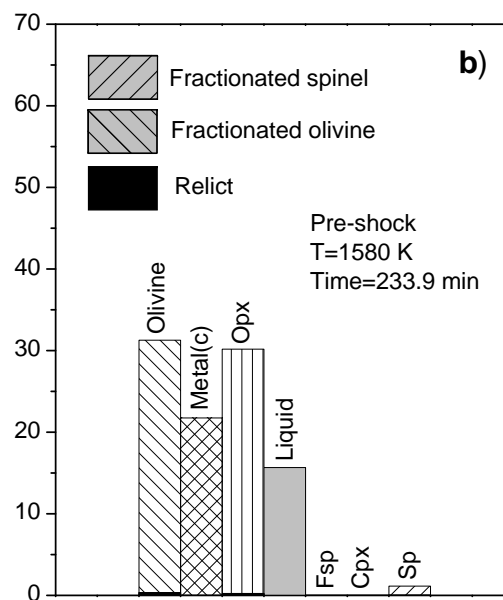
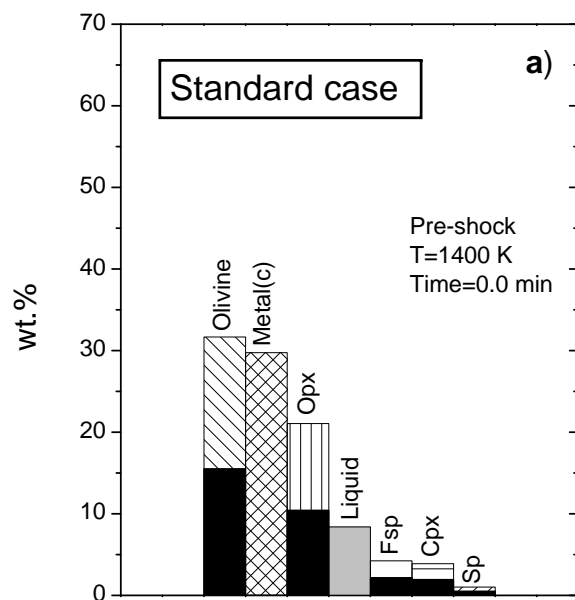




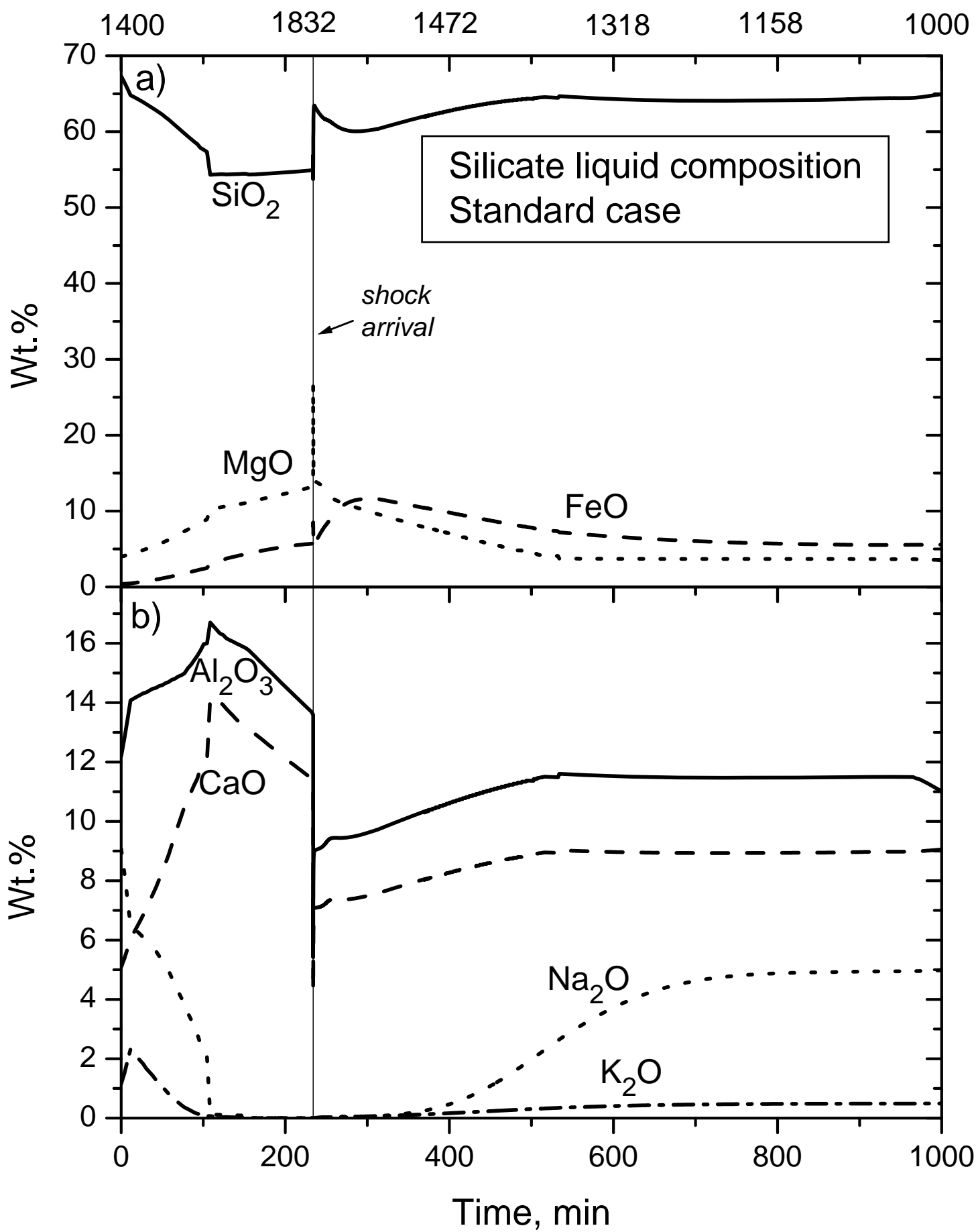


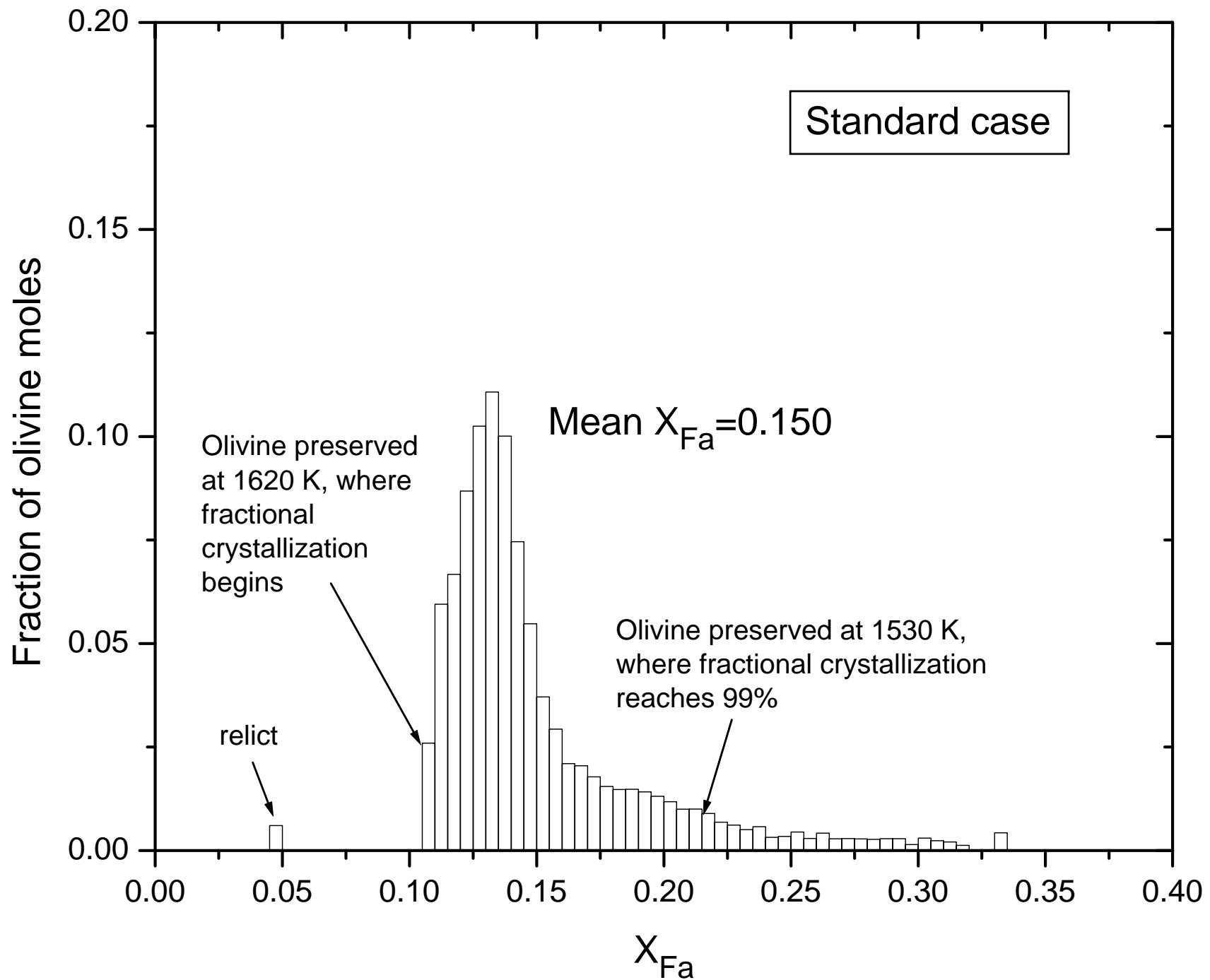






Temperature, K





Temperature, K

1400

1832

1472

1318

1158

1000

$\delta^{25}\text{Mg, ‰}$

0.00

-0.02

-0.04

-0.06

fractional xlzn
begins

recondensation
begins

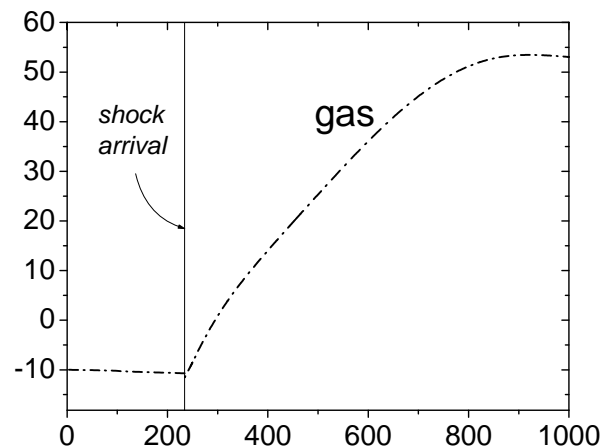
sequ. fr.

bulk

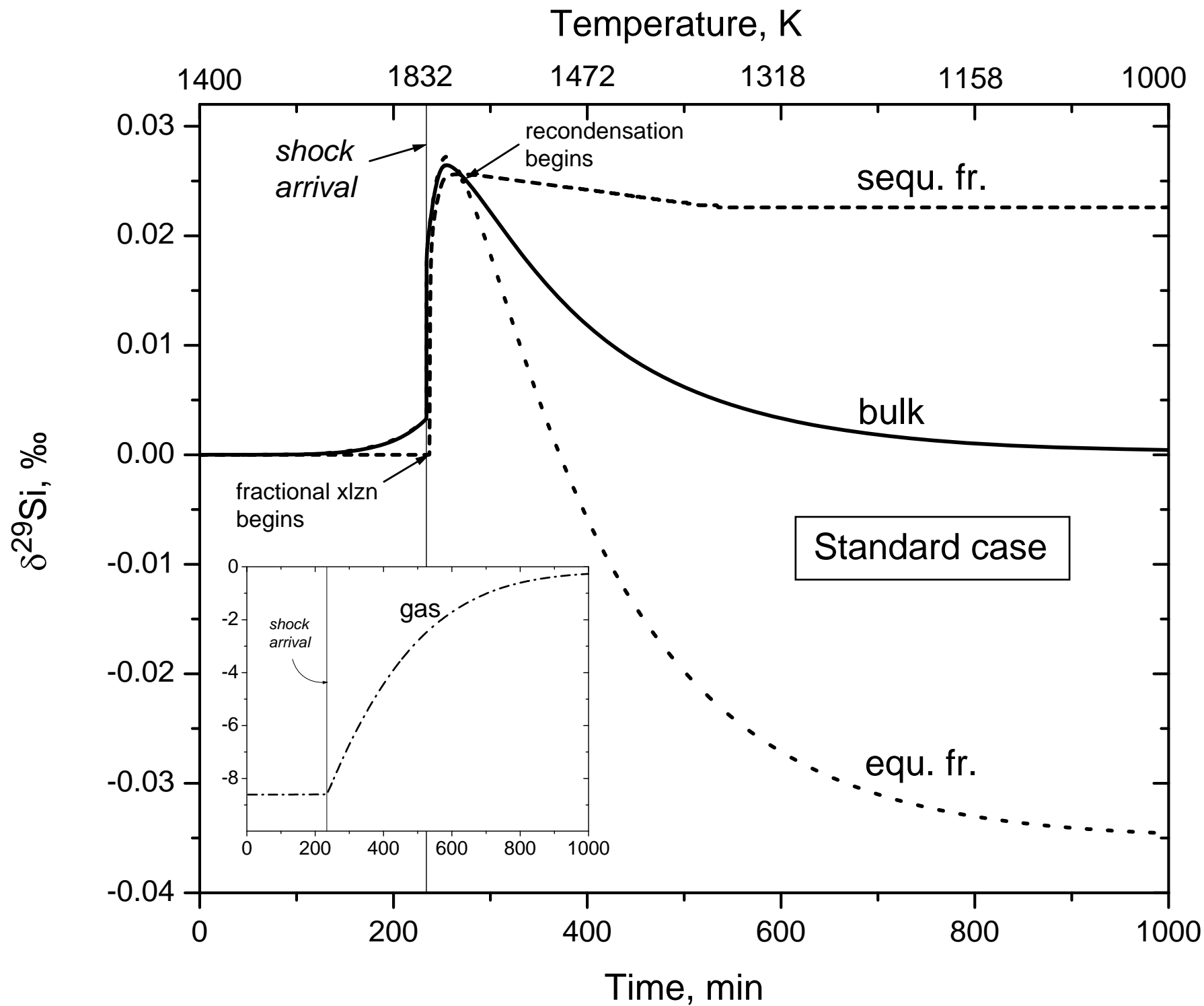
Standard case

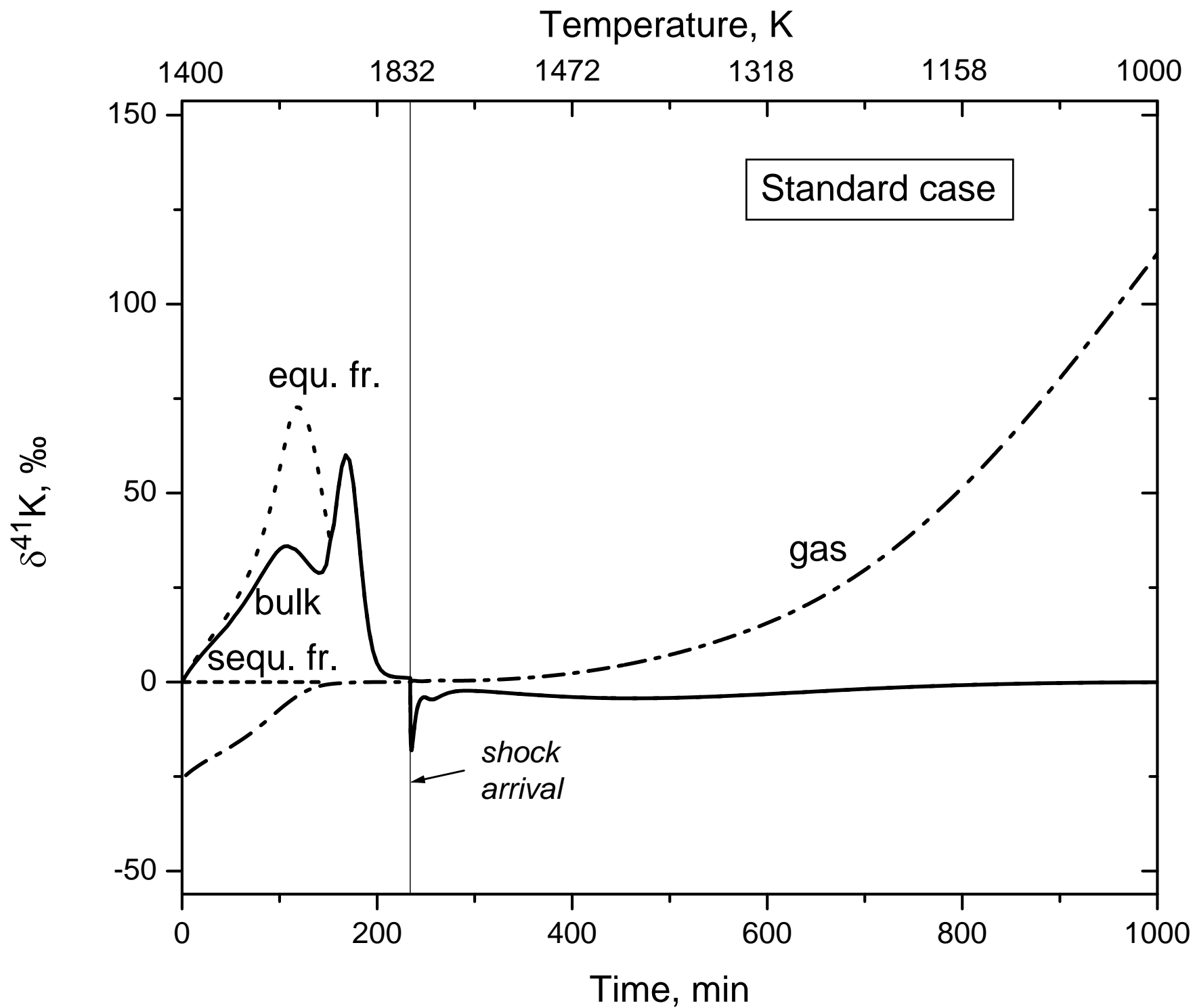
equ. fr.

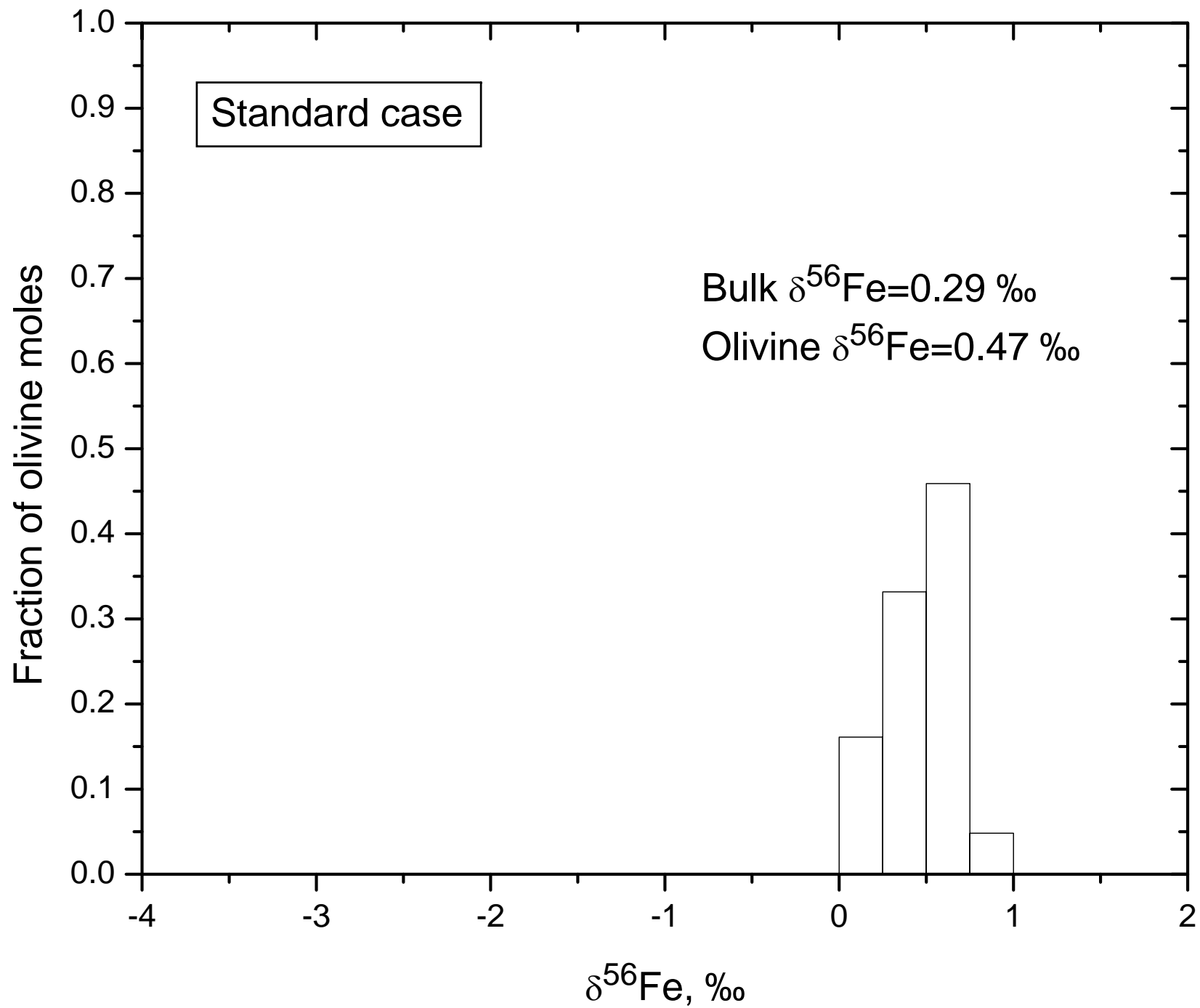
*shock
arrival*

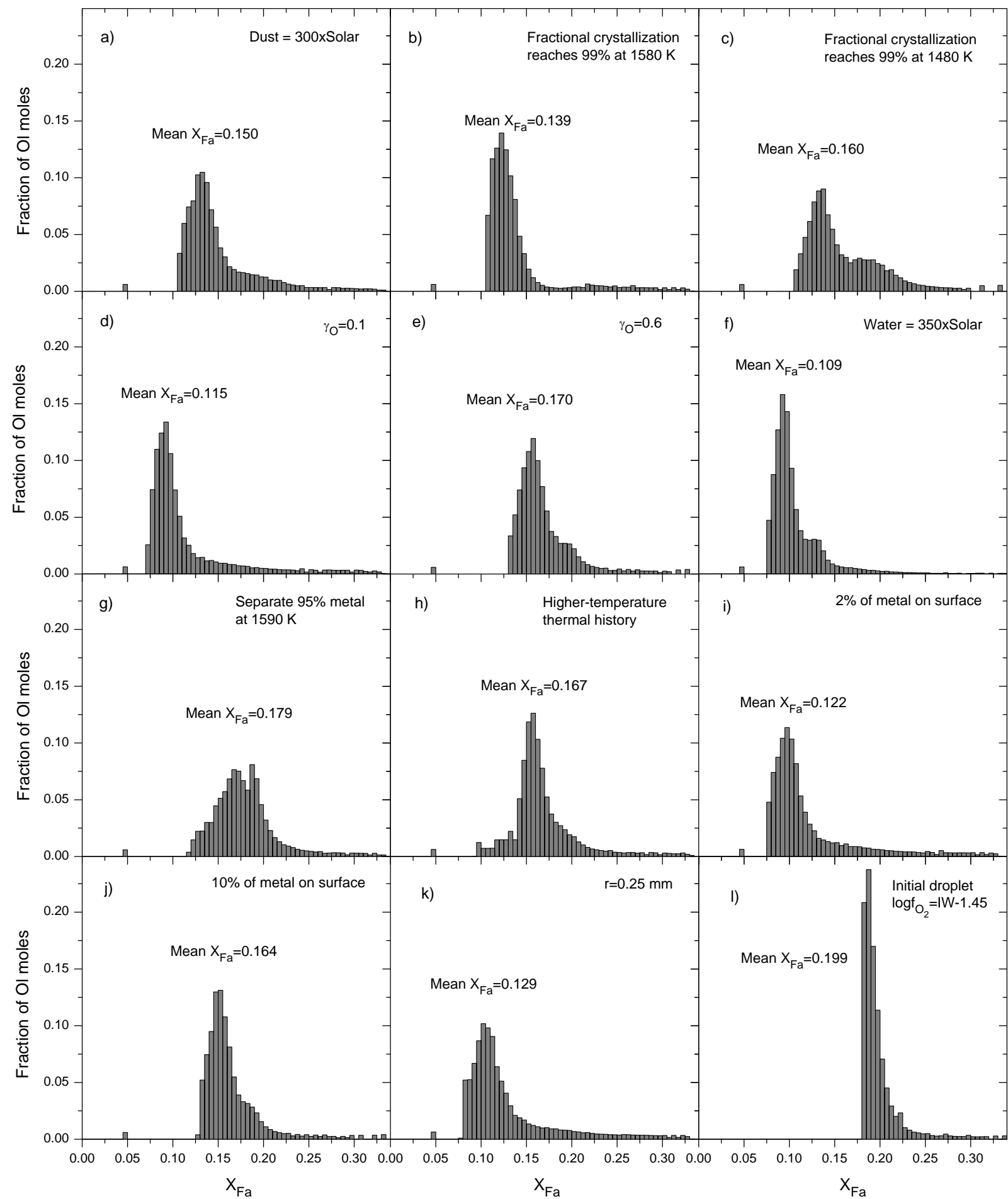


Time, min









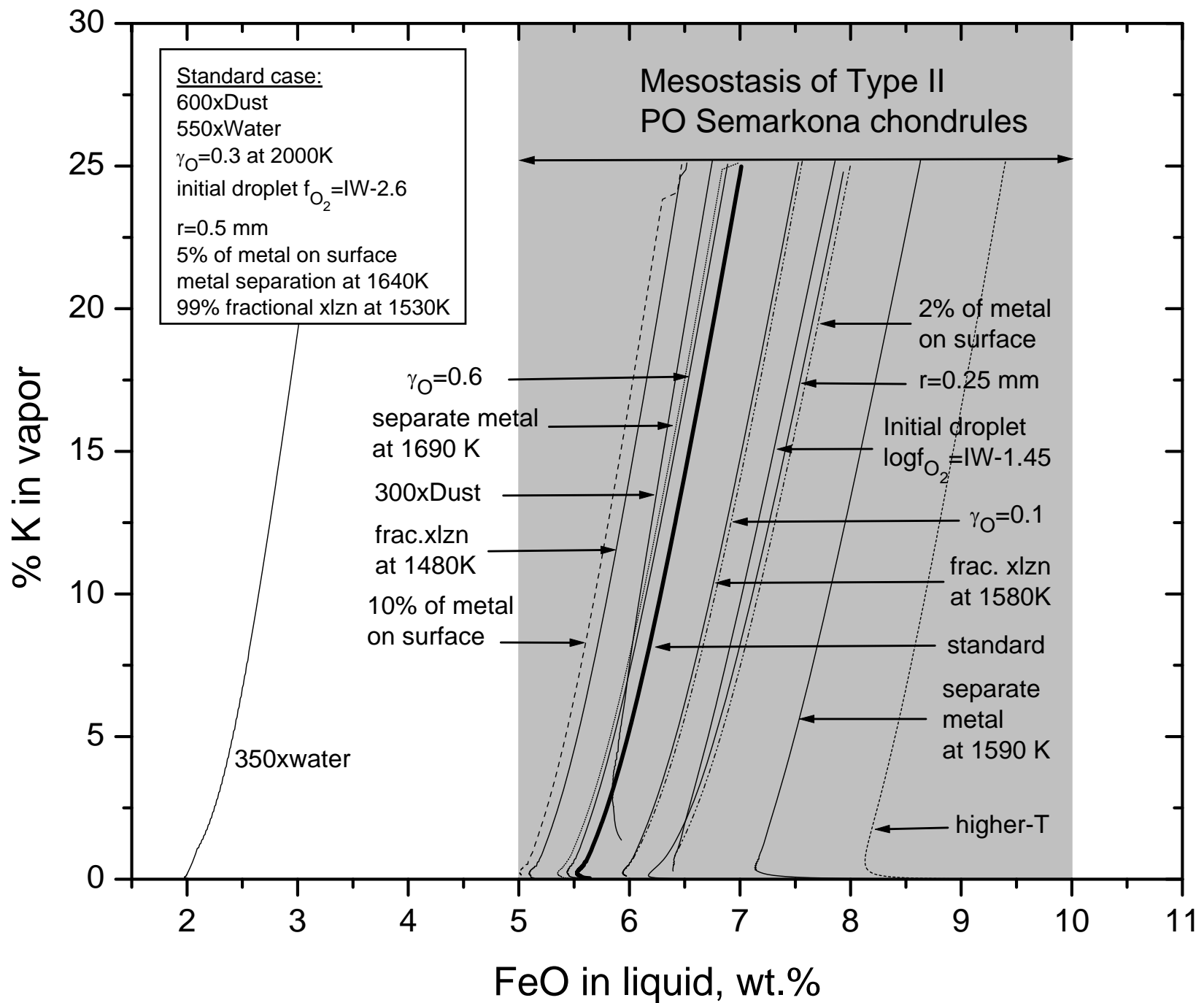


Table 1. Gas species included in the calculation.

Si	AlOH	CaS	C ₂ O	H ₂ N ₂	NS
Si ₂	AlS	Na	C ₃ O ₂	H ₂ O	O
Si ₃	Cr	Na ₂	CH	H ₂ O ₂	O ₂
SiC	CrN	NaCN	CH ₂	HO ₂	O ₃
SiC ₂	CrO	(NaCN) ₂	CH ₃	H ₂ P	OH
Si ₂ C	CrO ₂	NaH	CH ₄	HS	P
SiH	CrO ₃	NaO	C ₂ H	H ₂ S	P ₂
SiH ₄	Fe	NaOH	C ₂ H ₂	H ₂ SO ₄	P ₄
SiN	FeO	(NaOH) ₂	C ₂ H ₄	He	PH
Si ₂ N	Fe(OH) ₂	Na ₂ SO ₄	C ₂ H ₄ O	N	PH ₃
SiO	FeS	K	CHNO	N ₂	PO
SiO ₂	Mg	K ₂	CHO	N ₃	PO ₂
SiS	Mg ₂	KCN	CHP	NH	PS
Ti	MgH	(KCN) ₂	CN	NH ₃	P ₄ S ₃
TiO	MgN	(KOH) ₂	CN ₂	N ₂ H ₄	S
TiO ₂	MgO	KH	CNO	NO	S ₂
Al	MgOH	KO	CO	NO ₂	S ₃
Al ₂	Mg(OH) ₂	KOH	CO ₂	NO ₃	S ₄
AlC	MgS	K ₂ SO ₄	COS	N ₂ O	S ₅
AlH	Ni	C	CP	N ₂ O ₃	S ₆
AlN	NiS	C ₂	CS	N ₂ O ₄	S ₇
AlO	Ca	C ₃	CS ₂	N ₂ O ₅	S ₈
AlO ₂	Ca ₂	C ₄	H	NOH	SO
Al ₂ O	CaO	C ₅	H ₂	NO ₂ H	SO ₂
Al ₂ O ₂	CaOH	C ₂ N ₂	HCN	NO ₃ H	SO ₃
AlO ₂ H	Ca(OH) ₂	C ₂ N	H ₂ N	NP	S ₂ O

Table 2. Chemical and mineralogical composition of the assumed chondrule precursor at 1400 K and $\log f_{O_2} = \text{IW} - 2.6$.

Bulk	wt. %	Phases	wt. %	
SiO ₂	35.7			
TiO ₂	0.11	Alloy	30	X _{Ni} =0.06
Al ₂ O ₃	2.57	Olivine	32	X _{Fa} =0.05
Cr ₂ O ₃	0.61	Orthopyroxene	21	X _{Fs} =0.09
FeO	2.31	Clinopyroxene	4	X _{Di} =0.72, X _{En} =0.17
MgO	25.7	Spinel	1	X _{Chr} =0.72
NiO	0	Feldspar	4	X _{Ab} =0.62
CaO	2.03	Silicate Liquid	8	SiO ₂ 67.3, TiO ₂ 0.77, Al ₂ O ₃ 12.2,
Na ₂ O	1.06			Cr ₂ O ₃ 0.044, FeO 0.37, MgO 4.0,
K ₂ O	0.1			NiO 0.0, CaO 5.1, Na ₂ O 9.1,
Fe	28.1			K ₂ O 1.2 wt. %
Ni	1.72			

Table 3. Relative atomic abundances of systems employed in this work, compared to solar abundances that are normalized to 10^6 Si.

	Solar	300xDust 550xH ₂ O	600xDust 350xH ₂ O	600xDust 550xH ₂ O
H	2.790E+10	3.431E+10	3.197E+10	3.431E+10
He	2.720E+09	2.720E+09	2.720E+09	2.720E+09
C	6.849E+06	6.849E+06	6.849E+06	6.849E+06
N	3.130E+06	3.130E+06	3.130E+06	3.130E+06
O	1.367E+07	4.218E+09	4.056E+09	5.223E+09
Na	5.740E+04	1.722E+07	3.444E+07	3.444E+07
Mg	1.074E+06	3.222E+08	6.444E+08	6.444E+08
Al	8.490E+04	2.547E+07	5.094E+07	5.094E+07
Si	1.000E+06	3.000E+08	6.000E+08	6.000E+08
P	1.040E+04	1.040E+04	1.040E+04	1.040E+04
S	4.458E+05	1.337E+08	2.675E+08	2.675E+08
K	3.770E+03	1.131E+06	2.262E+06	2.262E+06
Ca	6.110E+04	1.833E+07	3.666E+07	3.666E+07
Ti	2.400E+03	7.200E+05	1.440E+06	1.440E+06
Cr	1.350E+04	4.050E+06	8.100E+06	8.100E+06
Fe	9.000E+05	2.700E+08	5.400E+08	5.400E+08
Ni	4.930E+04	1.479E+07	2.958E+07	2.958E+07

Table 4. Final silicate liquid composition for the standard case, compared to the mean mesostasis composition of 9 Type II PO chondrules (wt%).

	Model liquid	Mesostasis (Jones, 1990)
SiO ₂	65.5	63.3±1.9
TiO ₂	0.096	0.457±0.037
Al ₂ O ₃	10.5	11.1±1.3
Cr ₂ O ₃	0.001	0.320±0.139
FeO	5.83*	8.10±1.14
MgO	3.46	4.53±1.75
CaO	9.13	7.53±1.71
Na ₂ O	5.03	4.02±1.51
K ₂ O	0.498	0.581±0.144

*Including the equivalent of 0.27 wt.% Fe₂O₃